

OPACITY BUILDUP IN IMPULSIVE RELATIVISTIC SOURCES

JONATHAN GRANOT,^{1,2,3} JOHANN COHEN-TANUGI,^{1,3} AND EDUARDO DO COUTO E SILVA¹

Received 2007 August 30; accepted 2007 November 4

ABSTRACT

Opacity effects in relativistic sources of high-energy gamma-rays, such as gamma-ray bursts (GRBs) or blazars, can probe the Lorentz factor of the outflow as well as the distance of the emission site from the source and, thus, help constrain the composition of the outflow (protons, pairs, magnetic field) and the emission mechanism. Most previous works consider the opacity in steady state. Here we study time-dependent effects of the opacity to pair production ($\gamma\gamma \rightarrow e^+e^-$) in impulsive relativistic sources. We present a simple, yet rich, semianalytic model for the time and energy dependence of the optical depth, $\tau_{\gamma\gamma}$, in which a thin spherical shell expands ultrarelativistically and emits isotropically in its own rest frame over a finite range of radii, $R_0 \leq R \leq R_0 + \Delta R$. This is particularly relevant for GRB internal shocks. We find that for impulsive sources ($\Delta R \lesssim R_0$), while the instantaneous spectrum has an exponential cutoff above the photon energy $\varepsilon_1(T)$ where $\tau_{\gamma\gamma}(\varepsilon_1) = 1$, the time-integrated spectrum has a power-law high-energy tail above the photon energy $\varepsilon_{1*} \sim \varepsilon_1(\Delta T)$ where ΔT is the duration of the emission episode. Furthermore, photons with $\varepsilon > \varepsilon_{1*}$ should arrive mainly near the onset of the spike or flare corresponding to the short emission episode, since in impulsive sources it takes time to build up the (target) photon field, and thus, $\tau_{\gamma\gamma}(\varepsilon)$ initially increases with time and $\varepsilon_1(T)$ correspondingly decreases with time, so that photons of energy $\varepsilon > \varepsilon_{1*}$ are able to escape the source mainly very early on while $\varepsilon_1(T) > \varepsilon$. As the source approaches a quasi-steady state ($\Delta R \gg R_0$), the time-integrated spectrum develops an exponential cutoff, while the power-law tail becomes increasingly suppressed.

Subject headings: galaxies: jets — gamma rays: bursts — gamma rays: theory — methods: analytical — relativity

Online material: color figures

1. INTRODUCTION AND MOTIVATION

Astrophysical sources of gamma rays that are both compact and very luminous may be optically thick to pair production ($\gamma\gamma \rightarrow e^+e^-$) within the source. The corresponding optical depth, $\tau_{\gamma\gamma}$, is usually an increasing function of the photon energy, and therefore, a large optical depth would prevent the escape of high-energy photons from the source, causing a high-energy cutoff in the observed spectrum. For sufficiently high optical depths, enough e^+e^- pairs may be produced, so that the optical depth of all photons (even low-energy photons that are optically thin to pair production) to scattering on these electrons/positrons would be much larger than unity, in which case the photon energy spectrum would be thermalized. The size of the gamma-ray-emitting region is usually hard to constrain directly from observations, since the angular resolution of gamma-ray telescopes is much poorer than their counterparts in lower energy photons (e.g., X-rays, optical, or radio). Nevertheless, the physical properties of the emitting region can be constrained using compactness arguments and the observed properties of the source. In particular, rapid flux variability of the source is often used in order to set upper limits on the size of the emitting region, making highly variable sources with significant nonthermal high-energy emission a prime target for such analysis. One of the best examples for such sources are gamma-ray bursts (GRBs), and we shall focus on them below, although most of our analysis has a much broader range of applicability (similar opacity considerations have also been used to constrain the properties of other sources, such as blazars, e.g., Sikora et al. 1994).

It has been realized early on that, in GRBs, pair production within the source is expected to cause a high-energy cutoff in the observed photon energy spectrum (see Piran 2005 and references therein). Naively, if the source shows significant flux variability on an observed timescale of ΔT , its size is inferred to be $R \lesssim c\Delta T/(1+z)$, where z is its cosmological redshift, and the optical depth to pair production at a dimensionless photon energy $\varepsilon \equiv E_{\text{ph}}/m_e c^2$ is $\tau_{\gamma\gamma}(\varepsilon) \sim \sigma_T L_{1/\varepsilon(1+z)} / 4\pi m_e c^3 R \gtrsim \sigma_T L_{1/\varepsilon(1+z)} (1+z) / 4\pi m_e c^4 \Delta T \sim 10^{14} (1+z) [L_{1/\varepsilon(1+z)} / (10^{51} \text{ erg s}^{-1})] [\Delta T / (1 \text{ ms})]^{-1}$, where $L_\varepsilon = F_{\varepsilon/(1+z)} 4\pi d_L^2 (1+z)^{-1}$ and F_ε are the source isotropic equivalent luminosity and observed flux per unit dimensionless photon energy, respectively, and d_L is the luminosity distance to the source. For GRBs the (observed part of the) $\varepsilon F_\varepsilon$ spectrum typically peaks around $\varepsilon \sim 1$, and being at cosmological distances, their isotropic equivalent luminosity is typically in the range of $10^{50} - 10^{53} \text{ erg s}^{-1}$. Furthermore, they often show significant variability down to millisecond timescales. This implies huge values of $\tau_{\gamma\gamma}$, as high as $\sim 10^{15}$, under the above naive assumptions. Such huge optical depths are clearly inconsistent with the non-thermal GRB spectrum, which has a significant power-law high-energy tail. This is known as the compactness problem (Ruderman 1975).

If the source is moving relativistically toward us with a Lorentz factor $\Gamma \gg 1$, then in its own rest frame the photons have smaller energies, $\varepsilon' \sim \varepsilon(1+z)/\Gamma$, while in the lab frame (i.e., the rest frame of the central source) most of the photons propagate at angles $\lesssim 1/\Gamma$ relative to its direction of motion. The latter implies that in the lab frame the typical angle between the directions of the interacting photons is $\theta_{12} \sim 1/\Gamma$, which has two effects. First, it increases the threshold for pair production, $(1+z)^2 \varepsilon_1 \varepsilon_2 > 2/(1 - \cos \theta_{12})$, to $(1+z)^2 \varepsilon_1 \varepsilon_2 \gtrsim \Gamma^2$ (compared to $\varepsilon'_1 \varepsilon'_2 \gtrsim 1$ for the roughly isotropic distribution of angles between the directions of the interacting

¹ Kavli Institute for Particle Astrophysics and Cosmology, Stanford Linear Accelerator Center, Stanford University, P.O. Box 20450, MS 29, Stanford, CA 94309.

² Centre for Astrophysics Research, University of Hertfordshire, College Lane, Hatfield, Herts, AL10 9AB, UK.

³ The first two authors contributed equally to this work. Send reprint requests to granot@slac.stanford.edu, cohen@slac.stanford.edu.

photons in the rest frame of the source, where $\theta'_{12} \sim 1$). This reduces $\tau_{\gamma\gamma}(\varepsilon)$ by a factor of $\Gamma^{2(1-\alpha)}$ where $L_\varepsilon \approx L_0\varepsilon^{1-\alpha}$ at high photon energies (corresponding to $dN_{\text{ph}}/d\varepsilon \propto \varepsilon^{-\alpha}$, i.e., α is the high-energy photon index), since $L_{1/\varepsilon(1+z)}$ needs to be replaced by $L_{\Gamma^2/\varepsilon(1+z)} = \Gamma^{2(1-\alpha)}L_{1/\varepsilon(1+z)}$. Second, the expression for the optical depth includes a factor of $1 - \cos \theta_{12}$ (that represents the rate at which photons pass each other and have an opportunity to interact) which for a stationary source is ~ 1 , but for a relativistic source moving toward us is $\sim \Gamma^{-2}$. Finally, the size of the emitting region can be as large as $R \sim \Gamma^2 c\Delta T/(1+z)$, which reduces $\tau_{\gamma\gamma}$ by an additional factor of Γ^{-2} . Altogether, $\tau_{\gamma\gamma}(\varepsilon)$ is reduced by a factor of $\sim \Gamma^{2(\alpha+1)}$, and since typically $\alpha \sim 2-3$, this usually implies $\Gamma \gtrsim 10^2$ in order to have $\tau_{\gamma\gamma} < 1$ and overcome the compactness problem. Using similar arguments, the lack of such a high-energy cutoff due to pair production in the observed spectrum of the prompt gamma-ray emission in GRBs has been used to place lower limits on the Lorentz factor of the outflow (Krolik & Pier 1991; Fenimore et al. 1993; Woods & Loeb 1995; Baring & Harding 1997; Lithwick & Sari 2001).

We note, however, that $\tau_{\gamma\gamma}$ generally depends both on the radius of emission, R , and on the bulk Lorentz factor, Γ , $\tau_{\gamma\gamma}(\varepsilon) \propto \Gamma^{-2\alpha}R^{-1}L_0\varepsilon^{\alpha-1}$. Therefore, one needs to assume a relation between R and Γ in order to obtain a lower limit on the latter. Most works assume $R \sim \Gamma^2 c\Delta T/(1+z)$ (e.g., Lithwick & Sari 2001), which gives $\tau_{\gamma\gamma}(\varepsilon) \propto \Gamma^{-2(\alpha+1)}(\Delta T)^{-1}L_0\varepsilon^{\alpha-1}$, while the lack of a high-energy cutoff up to some photon energy ε implies $\tau_{\gamma\gamma}(\varepsilon) < 1$. This, in turn, provides a lower limit on Γ , since one can directly measure the variability time ΔT , the photon index α , and $L_0 \approx 4\pi d_L^2(1+z)^{\alpha-2}\varepsilon^{\alpha-1}F_\varepsilon$. However, the relation $R \sim \Gamma^2 c\Delta T/(1+z)$ does not hold for all models of the prompt GRB emission. For example, this relation does not hold if the prompt GRB emission is generated by relativistic magnetic reconnection events, with angular scales $\ll 1/\Gamma$, that create local relativistic motion with Lorentz factor $\gamma_{\text{rel}} \sim 5-10$ relative to the average bulk value Γ of the emitting shell (Lyutikov & Blandford 2002, 2003). In this case $\Delta T/(1+z) \ll R/c\Gamma^2$ and the inferred value of the Lorentz factor from standard opacity arguments would be $\sim \gamma_{\text{rel}}\Gamma$ rather than the bulk Lorentz factor of the shell, Γ . This allows the radius of the prompt emission to be as large as $R \sim 10^{16}-10^{17}$ cm, close to the deceleration radius where most of the energy of the outflow is transferred to the swept-up external medium, and is much larger than the prompt emission radius that is expected in the internal shocks model, $R \sim 10^{13}-10^{14}$ cm. Therefore, we adopt a more model-independent approach and do not automatically make this assumption. Instead, we derive most of our formulae without this assumption, as well as derive expressions for Γ under this assumption, which could serve in order to test its validity.

The *Gamma-Ray Large Area Space Telescope (GLAST)* mission (Ritz 2007), to be launched in early 2008, is expected to shed light on the high-energy emission from GRBs and other impulsive relativistic sources. In particular, opacity effects due to the local photon field within the source⁴ are expected to be most relevant in the *GLAST* Large Area Telescope (LAT) energy range (20 MeV to more than 300 GeV; see Reimer 2007). Thus, it represents a powerful tool for probing the physics of these sources. *GLAST* is likely to detect the high-energy cutoff due to pair production opacity which would actually determine $\Gamma^{2\alpha}R$, rather than just provide a lower limit for it. Furthermore, in GRBs the outflow Lorentz factor Γ may be constrained by the time of the afterglow onset (Panaitescu & Kumar 2002; Lee et al. 2005; Molinari et al. 2007), provided that the reverse shock is not highly relativistic, so that if *GLAST* detects the high-energy pair production opacity cutoff, the radius of emission R could be directly constrained, thus helping to test the different GRB models. In particular, this could directly test whether the relation $R \sim \Gamma^2 c\Delta T/(1+z)$ that is expected in many models indeed holds, since both R and Γ could be determined separately. This, however, requires a reliable way of identifying the observed signatures of opacity to pair production. This is one of the main motivations for this work.

The leading model for the prompt emission in GRBs features internal shocks (Rees & Mészáros 1994) due to collisions between shells that are ejected from the source at ultrarelativistic speeds ($\Gamma \gtrsim 100$). The shells are typically quasi-spherical, i.e., their properties do not vary a lot over angles \lesssim a few Γ^{-1} around our line of sight. Under the typical physical conditions that are expected in the shocked shells, all electrons cool on a timescale much shorter than the dynamical time (i.e., the time it takes the shock to cross the shell), and most of the radiation is emitted within a very thin cooling layer just behind the shock front. Thus, our model which features an emitting spherical thin shell that expands outward ultrarelativistically is appropriate for the internal shocks model.

As this emitting “shell” expands outward to larger radii, it builds up a photon field that can pair produce with high-energy photons from the same emission component. This effect has been studied in the past (see especially Baring 2006 and references therein), but the temporal and spatial dependences of the photon field have been averaged out, corresponding either explicitly or implicitly to a quasi-steady state. However, in impulsive relativistic sources the timescale for significant variations in the properties of the radiation field within the source is comparable to the total duration of the emission episode, and therefore, the dependence of the opacity to pair production on space and time cannot be ignored and may produce important effects that are suppressed in the steady state limit. Therefore, in the present work we consider the full temporal and spatial dependence of the opacity, in order to capture all the resulting effects.

We develop a simple, yet rich, model to investigate quantitatively the intuitive consideration that in impulsive sources it takes time to build up the (target) photon field, and thus, the optical depth initially increases with time, so that high-energy photons might be able to escape the source mainly at the very early part of the spike in the light curve. This results in a power-law tail for the time-integrated spectrum at high energies, while the instantaneous spectrum (which is hard to measure due to poor photon statistics) has an exponential cutoff. This arises since the photon energy of the exponential cutoff in the instantaneous spectrum decreases with time, as the opacity increases with time at all energies. Therefore, at sufficiently high photon energies, most of the photons escape during the short initial time before the optical depth increases above unity, i.e., before the cutoff energy sweeps past their energy.

We perform detailed semianalytic calculations of the optical depth to pair production, which improve on previous works by first calculating the photon field at each point in space and time and then integrating along the trajectory of each photon. The structure of the paper is as follows. In § 2 we introduce our model and derive a general expression for the flux that reaches an observer at infinity. This expression includes the optical depth along the trajectory of each photon that may reach the observer, which is derived in § 3. The

⁴ In the present work, we do not consider opacity effects due to the interaction of high-energy photons with the extragalactic background light. Such an attenuation, interesting in its own right, can be added to the “in source” opacity in a straightforward way. Furthermore, it is expected to become significant (i.e., produce $\tau_{\gamma\gamma} > 1$) only at cosmological redshifts ($z \gtrsim 1$) and for very high photon energies ($\gtrsim 56-100$ GeV at $z = 1$ and $\gtrsim 18-63$ GeV at $z = 3$; Kneiske et al. 2004) and is therefore likely to significantly affect only the high end of the *GLAST* energy range, where the photon statistic might be too poor to reliably measure this effect. This source of opacity will be independent of time (and depends only on the redshift of the source and on the photon energy), which would help in disentangling it from the time-dependent opacity intrinsic to the source that we calculate in this work.

calculation of the optical depth requires the knowledge of the photon field at each point along the trajectory of each (test) photon. This local photon field is first expressed in terms of the source emissivity (§ 3.1). Next (§ 3.2) it is conveniently rewritten as the product of the typical optical depth (that is approached on a dynamical time and is similar to that derived in previous works) and dimensionless order unity expression (containing a few integrals) which captures the new time-dependent effects that are the focus of this work. In § 4 explicit expressions are derived for the integrands of these dimensionless order unity integrals. In § 5 we derive the relevant analytic scalings for the resulting optical depths and observed flux, and in § 6 we present numerical results (i.e., numerically evaluate the semianalytic expressions) for the opacity, light curves, and spectra (both the instantaneous and time-integrated spectra are addressed in §§ 5 and 6). Our conclusions are discussed in § 7. Readers that are interested mainly in the final results and not in the technical details of the calculations can skip §§ 2.2–4. While § 5 is still a little technical, it is easier to follow and helps one to understand the results shown in § 6, so it should not be skipped, if possible.

2. CALCULATING THE OBSERVED FLUX

2.1. Model Assumptions

We consider an ultrarelativistic (with Lorentz factor $\Gamma \gg 1$), thin (of width $\ll R/\Gamma^2$ in the lab frame) spherical expanding shell that emits over a finite range of radii, $R_0 \leq R \leq R_0 + \Delta R$ (i.e., the emission turns on at R_0 and turns off at $R_0 + \Delta R$). This model can be associated with a single pulse or flare in the light curve. In the context of internal shocks within the outflow, $\Delta R \sim R_0$ is typically expected (Rees & Mészáros 1994; Piran 2005 and references therein).

The emission is assumed to be isotropic in the comoving frame of the emitting shell (i.e., the shell rest frame) and uniform over the spherical shell. In this work primed quantities are always measured in the comoving frame, while unprimed quantities are evaluated either in the lab frame, that is, the rest frame of the central source, in which the shell is spherical (e.g., the Lorentz factor Γ), or in the observer frame (e.g., the observed time and photon energy which suffer cosmological time dilation and redshift, respectively, relative to the lab frame which is at the cosmological redshift of the source). The observer is assumed to be located at a distance from the source that is much larger than the source size (so that the angle subtended by the source, as seen by the observer, is very small, and the observer can be considered as being at “infinity”).

For convenience, we use dimensionless photon energies, ε , in which the observed photon energy, E_{ph} , is normalized by the electron rest energy, $\varepsilon \equiv E_{\text{ph}}/m_e c^2$. While general expressions are provided when possible, we also provide detailed semianalytical solutions to the model by assuming that the luminosity in the shell rest frame has a power-law dependence on rest-frame photon energy ε' and radius R , $L'_{\varepsilon'} \propto (\varepsilon')^{1-\alpha} R^b$, and that the Lorentz factor scales as a power law with radius, $\Gamma^2 \propto R^{-m}$. The approximation that Γ and $L'_{\varepsilon'}$ scale as power laws with radius is usually expected to hold reasonably well. For internal shocks, the colliding shells are expected to be in the coasting stage near the collision radius (R_0), which corresponds to $m = 0$ (see Piran 2005; Mészáros 2006 and references therein). In the GRB afterglow, both before and after the deceleration radius, where most of the energy is transferred from the ejecta to the shocked external medium, Γ (Blandford & McKee 1976) and $L'_{\varepsilon'}$ (e.g., Sari 1998; Granot 2005) are expected to scale as power laws with radius. For GRB internal shocks, the scaling of $L'_{\varepsilon'}$ with radius R generally depends on the details of the colliding shells.

For uniform colliding shells, where the strength of the shocks going into the shells is constant with radius, above the peak of the νF_ν spectrum, $\varepsilon'_{\text{peak}}$, one expects $-0.5 \lesssim b \lesssim 0$. This may be understood as follows. In this case, the Lorentz factor in the shocked regions of the colliding shells is constant with radius, while the magnetic field scales as $B' \propto R^{-1}$. Therefore, since the number of emitting electrons scales linearly with radius, $N_e \propto R$, then $L'_{\varepsilon', \text{max}} \propto B' N_e \propto R^0$. The typical synchrotron photon energy scales as $\varepsilon'_m \propto B' \gamma_m^2 \propto R^{-1}$, since the typical Lorentz factor of the electrons, γ_m , is constant for a constant shock strength. The energy of a photon that cools on the dynamical time (the time since the start of the collision) scales as $\varepsilon'_c \propto R$. Therefore, above the peak of the νF_ν spectrum, at $\varepsilon' > \varepsilon'_{\text{peak}} = \max(\varepsilon'_c, \varepsilon'_m)$, we have $L'_{\varepsilon'} = L'_{\varepsilon', \text{max}} (\varepsilon'_m/\varepsilon'_c)^{-1/2} (\varepsilon'/\varepsilon'_m)^{-p/2} \propto R^{(2-p)/2}$, where p is the power-law index of the electron distribution, $dN_e/d\gamma_e \propto \gamma_e^{-p}$ for $\gamma_e > \gamma_m$. Since $p \sim 2-3$ is typically inferred for the GRB prompt emission, this corresponds to $-0.5 \lesssim b \lesssim 0$. For fast cooling ($\varepsilon'_c < \varepsilon'_m$) below $\varepsilon'_{\text{peak}} = \varepsilon'_m$, $L'_{\varepsilon'} = L'_{\varepsilon', \text{max}} (\varepsilon'/\varepsilon'_c)^{-1/2} \propto R^{1/2}$. For slow cooling ($\varepsilon'_c > \varepsilon'_m$), however, below $\varepsilon'_{\text{peak}} = \varepsilon'_c$, $L'_{\varepsilon', \text{max}} (\varepsilon'/\varepsilon'_m)^{(1-p)/2} \propto R^{(1-p)/2}$.

The simplifying assumption of a power-law emission spectrum [$L'_{\varepsilon'} \propto (\varepsilon')^{1-\alpha}$], however, is not always valid (see, e.g., Baring 2006). For example, in GRB internal shocks it breaks down for photons of energy $\varepsilon \gtrsim \Gamma^2/(1+z)^2 \varepsilon_{\text{peak}}$, i.e., $\varepsilon m_e c^2 \gtrsim 25(1+z)^{-2} (\Gamma/100)^2 (\varepsilon_{\text{peak}} m_e c^2/100 \text{ keV})^{-1} \text{ GeV}$. Indeed, photons of such energy interact with photons below the spectral break energy $\varepsilon_{\text{break}}$, which is the peak of the νF_ν spectrum. A detailed treatment of the case of a more realistic spectrum for GRB internal shocks will be provided elsewhere. The exact shape of the spectrum at high energies is not well constrained. Thus, we use a fiducial value of $\alpha = 2$, which corresponds to a flat νF_ν (i.e., equal energy per decade in photon energy), in our detailed illustrative solutions and also explore the effects of varying the value of α .

2.2. The Equal Arrival Time Surface of Photons to the Observer (EATS-I)

The observed normalized flux density, $F_\varepsilon = (m_e c^2/h) F_\nu$, is calculated as a function of time and photon energy, closely following the derivation of Granot (2005). For this purpose, the contributions to the observed flux at any given observed time T are integrated over the “equal arrival time surface” (EATS-I)—the locus of points from which photons that are emitted at the shell reach the observer simultaneously, at the observed time T . In the present work, the effects of opacity to pair production are added at the end of this calculation, as detailed below.

We consider a photon initially emitted by the shell at a lab frame time t_0 , when the radius of the shell is $R_{t,0} \equiv R_{\text{sh}}(t_0)$ and its Lorentz factor is $\Gamma_{t,0}$, at an angle of $\theta_{t,0}$ from our line of sight to the origin $R = 0$ (see Fig. 1). Because of the spherical symmetry of our model, there is no dependence on the azimuthal angle. The arrival time T of the photon to a distant observer is given by the “equal arrival time” formula

$$\frac{T}{(1+z)} = t_0 - \frac{R_{t,0}}{c} \cos \theta_{t,0}, \quad (1)$$

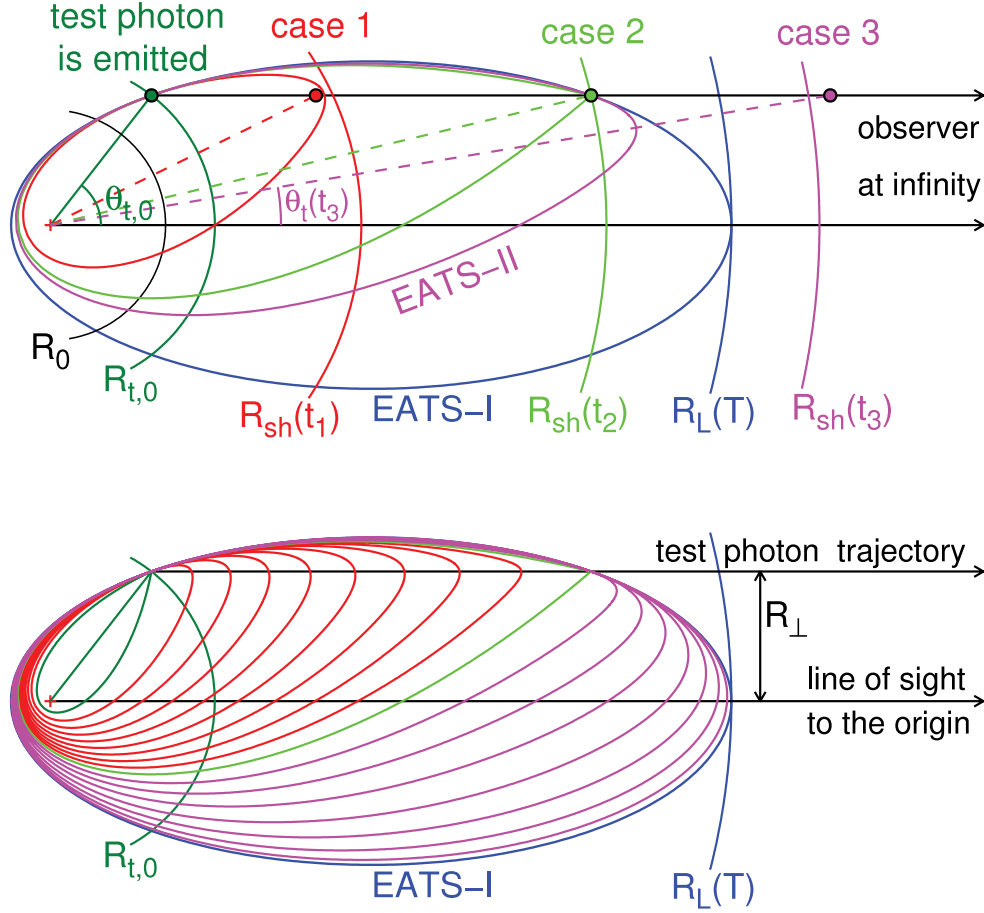


FIG. 1.—Illustration of the two different equal arrival time surfaces (EATS) of photons: (1) to the observer at infinity (EATS-I, blue) and (2) to the instantaneous location of a test photon (EATS-II, different colors). The overall geometry as well as relevant radii and angles are shown in the top panel, along with an illustration of the three different cases that are discussed in the text, in which the test photon either lags behind the shell (case 1), coincides with the shell (case 2), or is in front of the shell (case 3). The bottom panel shows the sequence of EATS-II, whose size increases with time, nested within the EATS-II which correspond to a larger time, and in particular within EATS-I which corresponds to an infinite time (i.e., an infinite radius for the test photon, when it reaches the observer at infinity).

where the lab frame time t is related to the shell radius at that time, $R_{sh}(t)$, by

$$t = \int_0^{R_{sh}(t)} \frac{dR}{\beta c} = \frac{R_{sh}(t)}{c} + \frac{1}{2c} \int_0^{R_{sh}(t)} \frac{dR}{\Gamma^2(R)} + O(\Gamma^{-4}). \quad (2)$$

In equation (1), $T = 0$ is chosen to correspond to a photon that is emitted at the origin at $t_0 = 0$. Equation (2) relates t and $R_{sh}(t)$, so that the locus of points $(R_{t,0}, \theta_{t,0})$ that keep T constant defines the EATS-I at time T . For a coasting shell ($m = 0$), it is a well-known result that the EATS-I is an ellipse⁵ of semimajor to semiminor axis ratio Γ (Rees 1966). The flux density at the rescaled energy ε is obtained by integrating over the luminosity in the shell rest frame, $L'_{\varepsilon'}$, along the EATS-I (Granot 2005),

$$F_{\varepsilon}(T) = \frac{(1+z)}{4\pi d_L^2} \int \delta^3 dL'_{\varepsilon'} = \frac{(1+z)}{8\pi d_L^2} \int_{y_{\min}}^{y_{\max}} dy \frac{d\mu_{t,0}}{dy} \delta^3(y) L'_{\varepsilon'}(y), \quad (3)$$

where $\delta \equiv (1+z)\varepsilon/\varepsilon'$ is the Doppler factor of the emitted photon (between the comoving and lab frames), $\mu_{t,0} \equiv \cos \theta_{t,0}$ is the cosine of its angle of emission, and we defined the normalized radius $y \equiv R_{t,0}/R_L$, where $R_L = R_L(T)$ is the largest radius on the EATS-I at time T . The integration is performed along the EATS-I, and the boundaries for y are

$$y_{\min}(T) = \min \left[1, \frac{R_0}{R_L(T)} \right], \quad y_{\max} = \min \left[1, \frac{R_0 + \Delta R}{R_L(T)} \right], \quad (4)$$

since the emission turns on at R_0 and turns off at $R_0 + \Delta R$. For the times T relevant to the problem, corresponding to the arrival of photons to the observer, $R_0/R_L(T)$ is always smaller than 1.

⁵ It actually represents an ellipsoid, keeping in mind the symmetry around the line of sight to the center of the emitting spherical shell and the lack of dependence on the azimuthal angle.

In order to evaluate the integral above, we now derive expressions for the integrand. Defining $\Gamma_L \equiv \Gamma(R_L)$, $\Gamma^2 \propto R^{-m}$ can be rewritten as $\Gamma^2(R)R^m = \Gamma_L^2 R_L^m = \text{const}$, and thus, $\Gamma^2 = \Gamma_L^2 y^{-m}$. Equation (2) now becomes

$$t_0 = \frac{R_{t,0}}{c} + \frac{R_L y^{m+1}}{2(m+1)\Gamma_L^2 c} + O(\Gamma^{-4}). \quad (5)$$

In the limit of small angles ($\theta_{t,0} \ll 1$, which is relevant for $\Gamma \gg 1$), equation (1) implies $t_0 - R_{t,0}/c = T/(1+z) - R_{t,0}\theta_{t,0}^2/2c$, which together with equation (5) yields

$$\frac{T}{(1+z)} = \frac{R_L y^{m+1}}{2(m+1)\Gamma_L^2 c} + \frac{R_{t,0}\theta_{t,0}^2}{2c}. \quad (6)$$

As can be seen in Figure 1, a photon that is emitted at $R_{t,0} = R_L$ [corresponding to $y = R_{t,0}/R_L(T) = 1$] remains along the line of sight ($\theta_t = \theta_{t,0} = 0$), so that equation (6) yields

$$R_L(T) = 2(m+1)\Gamma_L^2(T) \frac{cT}{(1+z)} = R_0 \left(\frac{T}{T_0} \right)^{1/(m+1)}, \quad T_0 = \frac{(1+z)R_0}{2(m+1)c\Gamma_0^2}, \quad (7)$$

where $\Gamma_0 \equiv \Gamma(R_0)$, and can be rewritten as

$$\theta_{t,0}^2 = \frac{y^{-1} - y^m}{(m+1)\Gamma_L^2}. \quad (8)$$

We have introduced the time T_0 at which the first photons reach the observer (corresponding to a photon emitted at R_0 along the line of sight, $\theta = 0$), $R_L(T_0) \equiv R_0$. Since $\mu_{t,0} \approx 1 - \theta_{t,0}^2/2$, equation (8) implies

$$\frac{d\mu_{t,0}}{dy} = \frac{y^{-2} + my^{m-1}}{2(m+1)\Gamma_L^2}. \quad (9)$$

Finally, the Doppler factor of the emitted electron is given by

$$\delta \equiv \frac{1}{\Gamma(1 - \beta \cos \theta_{t,0})} \approx \frac{2\Gamma}{1 + (\Gamma\theta_{t,0})^2} = \frac{2(m+1)\Gamma_L y^{-m/2}}{m + y^{-m-1}}, \quad (10)$$

and its value at R_L (which corresponds to $y = 1$) is $\delta(R_L) = 2\Gamma_L$. Since

$$L'_{\varepsilon'} = L'_{(1+z)\varepsilon/\delta(R_L)}(R_L) \left[\frac{\varepsilon'}{\varepsilon'(R_L)} \right]^{1-\alpha} \left(\frac{R_{t,0}}{R_L} \right)^b, \quad (11)$$

where $\varepsilon' = (1+z)\varepsilon/\delta$, we obtain

$$L'_{\varepsilon'} = L'_{(1+z)\varepsilon/2\Gamma_L}(R_L) \left(\frac{\delta}{2\Gamma_L} \right)^{\alpha-1} y^b = L'_{(1+z)\varepsilon/2\Gamma_0}(R_0) \left(\frac{\delta}{2\Gamma_L} \right)^{\alpha-1} y^b \left(\frac{R_L}{R_0} \right)^{b-m(\alpha-1)/2}. \quad (12)$$

The effect of pair production opacity is treated in this work in a somewhat simplified manner, by assuming that photons which pair produce do not reach the observer and ignoring the additional opacity that is produced by the secondary pairs and the photons emitted by these pairs. Under these simplifications, the effects of opacity to pair production can be included by adding a term $\exp(-\tau_{\gamma\gamma})$ into the integrand in equation (3). Thus, by combining equations (9)–(12) with equation (3), we obtain

$$\begin{aligned} F_{\varepsilon}(T) &= 2\Gamma_L L'_{(1+z)\varepsilon/2\Gamma_L}(R_L) \frac{(1+z)}{4\pi d_L^2} \int_{y_{\min}}^{y_{\max}} dy \left(\frac{m+1}{m+y^{-m-1}} \right)^{1+\alpha} y^{b-1-m\alpha/2} e^{-\tau_{\gamma\gamma}} \\ &= 2\Gamma_0 L'_{(1+z)\varepsilon/2\Gamma_0}(R_0) \frac{(1+z)}{4\pi d_L^2} \left(\frac{T}{T_0} \right)^{(2b-m\alpha)/[2(m+1)]} \int_{y_{\min}}^{y_{\max}} dy \left(\frac{m+1}{m+y^{-m-1}} \right)^{1+\alpha} y^{b-1-m\alpha/2} e^{-\tau_{\gamma\gamma}}, \end{aligned} \quad (13)$$

where equation (7) is used to derive the scaling $R_L(T)/R_0 = (T/T_0)^{1/(m+1)}$,

$$\tau_{\gamma\gamma} = \tau_{\gamma\gamma} \left(y, \varepsilon, \frac{\Delta R}{R_0}, \frac{T}{T_0}, \frac{L_0}{\Gamma_0^{2\alpha} R_0} \right), \quad (14)$$

TABLE 1
NOTATION AND DEFINITION OF SOME QUANTITIES USED THROUGHOUT THIS WORK

Notation	Definition	Eq./Sect.
$\varepsilon \equiv E_{\text{ph}}/m_e c^2$	Observed photon energy normalized by the electron rest energy	§ 2.1
t, R, θ	Spherical coordinates (time, radius from the source, polar angle)	...
$R_0, \Delta R$	Onset radius and range of the emission episode	§ 2.1
$R_{\text{sh}}(t), \Gamma, \Gamma_0 \equiv \Gamma(R_0)$	Radius and bulk Lorentz factor of the emitting shell	eq. (2)
$m \equiv 2 d \log \Gamma/d \log R$	Power-law index of Γ^2 with radius R	§ 2.1
$L_0 \equiv \Gamma_0^\alpha L'_0$	Roughly: observed isotropic equivalent luminosity at R_0 and $\varepsilon = 1$	eq. (14)
$\alpha \equiv -d \log N_{\text{ph}}/d \log E_{\text{ph}}$	Photon index at large photon energies	§ 2.1
$b \equiv d \log L'_e/d \log R$	Power-law index of comoving spectral luminosity with radius	§ 2.1
$t_t, R_t, \theta_t, \Gamma_t \equiv \Gamma(R_t)$	Test photon spherical coordinates and shell Lorentz factor at R_t	§ 3
$t_0, R_{t,0}, \theta_{t,0}, \Gamma_{t,0}$	Initial test photon spherical coordinates and Lorentz factor	eqs. (1) and (8)
R_e, θ_e	Emission radius and polar angle of interacting photon	§ 3
T_0, T	Arrival times of first and subsequent photons at the observer	eqs. (7) and (1)
$R_L(T), R_{e,\text{max}}$	Maximal radius of emission along the EATS-I and EATS-II	eq. (7)
ε_1	Dimensionless photon energy at which $\tau_{\gamma\gamma}(\varepsilon_1) = 1$	§ 5
s	Path length along the test photon trajectory	eq. (17)
R_\perp	Distance of test photon from the line of sight to the origin	eq. (A1)
θ_{ii}	Angle between directions of test photon and interacting photon	eq. (19)
$\varepsilon_t, \varepsilon_i$	Dimensionless test/interacting photon energies in the lab frame	eq. (17)
$\mu \equiv \cos \theta$	Cosine of angle θ	...
$\chi \equiv [\varepsilon_t \varepsilon_i (1 - \mu_{ii})/2]^{1/2}$	Dimensionless photon energy in the center of momentum frame	eq. (18)
$\zeta \equiv (1 - \mu_{ii})/2$	Convenient integration variable	Appendix A.2
r	Interacting photon emission to test photon intersection distance	§ 3
θ_r	Angle of an interacting photon relative to the radial direction	§ 3
$\delta \equiv (1+z)\varepsilon/\varepsilon'$	Doppler factor between the comoving and lab frames	eq. (10)
f_m	Useful quantity	eq. (64)
τ_*	Typical optical depth at $\varepsilon = 1$ on a dynamical time ($\bar{T}_f > \bar{T} \sim 1$)	eq. (37)
$\tau_0, \mathcal{F}(\mathcal{X})$	Explicit analytic and integral parts of the optical depth	eq. (40)
$x \equiv (\Gamma_{t,0} \theta_{t,0})^2$	Rescaled emission angle squared	eq. (16)
$y \equiv R_{t,0}/R_L(T)$	Emission radius rescaled to the maximum radius on an EATS-I	eq. (3)
$\hat{R} \equiv R/R_{t,0}$	Radius rescaled to a given test photon emission radius	§ 3.2
$\tilde{R} \equiv R/R_t$	Radius rescaled to the instantaneous test photon radius	§ 3.2
$\bar{T} \equiv T/T_0 - 1$	Arrival time of photons rescaled to the earliest arrival time	§ 5
$\bar{\delta} \equiv \delta/\Gamma_t, \bar{\mu}_e \equiv \Gamma_t^2 \mu_e$	Rescaled Lorentz factor and cosine of the emission angle	eq. (35)
$\tilde{\zeta}_- \equiv \Gamma_t^2 \zeta$	Rescaled integration variable	eq. (38)
$Y \equiv (y - y_{\text{min}})/(y_{\text{max}} - y_{\text{min}}), Y_*$	Rescaled variable y and value at which \mathcal{F} changes its behavior	eq. (114)

as is shown below, and $L_\varepsilon \approx L_0 \varepsilon^{1-\alpha}$ is the observed isotropic equivalent luminosity. Unless specified otherwise, the derivations throughout this work are valid for a general value of m . For a coasting shell ($m = 0$), which is a case of special interest (as it is expected, e.g., for internal shocks), equation (13) simplifies to

$$F_\varepsilon(T) = 2\Gamma_0 L'_{(1+z)\varepsilon/2\Gamma_0}(R_0) \frac{(1+z)}{4\pi d_L^2} \left(\frac{T}{T_0}\right)^b \int_{y_{\text{min}}}^{y_{\text{max}}} dy y^{\alpha+b} e^{-\tau_{\gamma\gamma}}. \quad (15)$$

We have expressed the observed flux density for our model as a function of the observed time T , and we now need to derive the expression of the optical depth $\tau_{\gamma\gamma}$. We gather here the dependence on y of two quantities that will be needed below,

$$\hat{R}_0 \equiv \frac{R_0}{R_{t,0}} = \frac{y_{\text{min}}}{y} = \frac{R_0}{\Delta R} \frac{\Delta R}{R_{t,0}} = \frac{1}{y} \left(\frac{T}{T_0}\right)^{-1/(m+1)}, \quad x \equiv (\Gamma_{t,0} \theta_{t,0})^2 = \frac{y^{-(m+1)} - 1}{(m+1)}. \quad (16)$$

In order to facilitate reading, we include in Table 1 the most common quantities used throughout this work.

3. COMPUTATION OF THE OPTICAL DEPTH

As in § 2 we consider a “test” photon emitted by the shell at radius $R_{t,0}$ and angle $\theta_{t,0}$ with respect to the line of sight (see Fig. 1). All the quantities with a subscript t will always refer to such a test photon. We wish to calculate its optical depth to pair production with all the other photons which are emitted by the same source and denoted by a subscript i (for potentially “interacting”). The differential of the optical depth to pair production is given by (Weaver 1976)

$$d\tau_{\gamma\gamma} = \sigma^*(\chi(\varepsilon_t, \varepsilon_i, \mu_{ii}))(1 - \mu_{ii}) \frac{dn_i}{d\Omega_i d\varepsilon_i} d\Omega_i d\varepsilon_i ds. \quad (17)$$

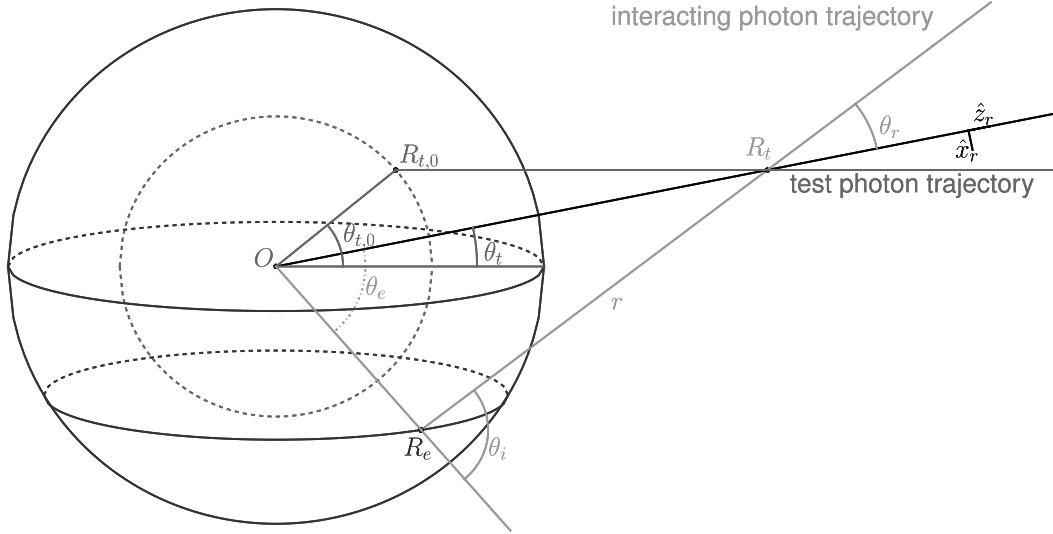


FIG. 2.— Geometry of the interaction between two photons, for a spherically symmetric shell. A test photon emitted at $R_{t,0}$ reaches $R_t > R_{t,0}$ at $t_t > t_0$ and can interact with a photon emitted at R_e that reaches the location R_t at the exact same time t_t as the test photon. Note that O , $R_{t,0}$, and R_t are coplanar (and in the plane of the figure), whereas R_e is not in the same plane nor is the interacting photon trajectory that goes from R_e to R_t . The observer is to the right, at infinity. The other symbols are defined in the text. [See the electronic edition of the *Journal* for a color version of this figure.]

In this equation, ds is the differential of the path length along the trajectory of the test photon; n_i , Ω_i , and $E_i \equiv \varepsilon_i m_e c^2$ are, respectively, the number density, solid angle, and photon energy of the photon field along the path of the test photon with which it might interact.⁶ For convenience, ε_t and ε_i denote the values of the corresponding dimensionless photon energies in the lab frame, rather than in the observer frame (as is the case for ε), i.e., without the cosmological redshift, so that $\varepsilon_i = (1+z)\varepsilon$ should eventually be used in order to evaluate the optical depth at an observed value of ε . The Lorentz invariant cross section for pair production $\sigma^*(\chi)$ is

$$\sigma^*(\chi) = \frac{\pi r_e^2}{\chi^6} \left[(2\chi^4 + 2\chi - 1) \ln(\chi + \sqrt{\chi^2 - 1}) - \chi(1 + \chi^2) \sqrt{\chi^2 - 1} \right], \quad (18)$$

$$\chi = \sqrt{\frac{\varepsilon_t \varepsilon_i (1 - \mu_{ti})}{2}}, \quad (19)$$

where χ is the center of momentum energy (in units of $m_e c^2$, of each particle—each of the two interacting photons and the produced electron and positron), and $\mu_{ti} = \hat{\mathbf{n}}_t \cdot \hat{\mathbf{n}}_i$ is the cosine of the angle between the directions of motion of the test photon ($\hat{\mathbf{n}}_t$) and a potentially interacting photon ($\hat{\mathbf{n}}_i$). In order to evaluate μ_{ti} , we need to specify the geometry for our model: a spherical emitting shell, whose emission depends only on its radius R_{sh} (i.e., at any given radius its local emission does not depend on the location within the shell) and is isotropic in its own rest frame. Under these assumptions, the radiation field will depend only on the radius R and the (lab frame) time t , and at any given place and time, it will be symmetric around the radial direction (see Fig. 2). Therefore, at any point along the trajectory of the test photon, we can use a local coordinate system, S_r , whose z -axis is aligned with the radial direction (from the center of the shell to that point), $\hat{\mathbf{z}}_r$, and such that the direction of motion of the test photon is in the x - z plane. In this frame the polar angles are denoted by (θ_r, ϕ_r) , and

$$\hat{\mathbf{n}}_t = \hat{\mathbf{x}}_r \sin \theta_t + \hat{\mathbf{z}}_r \cos \theta_t, \quad (20)$$

$$\hat{\mathbf{n}}_i = \hat{\mathbf{x}}_r \sin \theta_r \cos \phi_r + \hat{\mathbf{y}}_r \sin \theta_r \sin \phi_r + \hat{\mathbf{z}}_r \cos \theta_r, \quad (21)$$

$$\mu_{ti} = \hat{\mathbf{n}}_i \cdot \hat{\mathbf{n}}_t = \sin \theta_t \sin \theta_r \cos \phi_r + \cos \theta_t \cos \theta_r. \quad (22)$$

Note that θ_t varies only with s . The integration over the solid angle in the lab frame in equation (17) can conveniently use the frame S_r , which is at rest in the lab frame, i.e., $d\Omega_i = d\Omega_r = d\phi_r d\mu_r$. The optical depth of the test photon is then given by

$$\tau_{\gamma\gamma}(\varepsilon_t, \theta_{t,0}, R_{t,0}) = \int ds \int d\varepsilon_i \int d\Omega_r \sigma^*(\chi(\varepsilon_t, \varepsilon_i, \mu_{ti})) (1 - \mu_{ti}) \frac{dn_i}{d\Omega_r d\varepsilon_i}. \quad (23)$$

Next, we express the derivative in the integrand of equation (23), which represents the photon field along the trajectory of the test photon, in terms of the source emissivity. In addition, we make a series of changes of variable in order to simplify the expression for the optical depth.

⁶ We do not add a factor of 1/2 due to double counting (as was done by, e.g., Baring & Harding 1997; Dermer & Schlickeiser 1994), as it should not appear in the expression for the optical depth. We discuss this point in more details in Appendix E.

3.1. Expressing the Photon Field in Terms of the Source Emissivity

In § 2.2 we expressed the observed flux as an integral over the EATS-I of photons to the observer at an observed time T . These photons travel along straight line trajectories that pass through the photon field. As a result, we integrate the contribution to the optical depth at each point along the path of each photon, treating it as a test photon. This is the integration over ds in equation (23) which, as we show below, can be replaced by an integration over dR_t . In the other two inner integrations, R_t is kept fixed, and the photon field, $dn_i/d\Omega_r d\varepsilon_i$, needs to be evaluated as a function of ε_i , μ_r , and R_t . For a given test photon that is emitted at $(R_{t,0}, \mu_{t,0})$, the value of R_t also determines the value of the lab frame time t_t . We remind the reader that R_t and t_t are always computed in the lab frame and that R_t is in general different than $R_{sh}(t_t)$, i.e., at a general time the position of the test photon does not coincide with that of the shell. We proceed first to relate the photon field at (t_t, R_t) to the emissivity in the local frame of the emitting shell, which is easier to specify, and simpler. The Doppler factor of the emitted photon is given by

$$\delta \equiv \frac{\varepsilon_i}{\varepsilon'_i} = \frac{1}{\Gamma(1 - \beta\mu'_i)} = \Gamma(1 + \beta\mu'_i), \quad (24)$$

where $\mu_i \equiv \cos \theta_i = \boldsymbol{\beta} \cdot \hat{\mathbf{n}}_i$ and $\mu'_i \equiv \cos \theta'_i = \boldsymbol{\beta} \cdot \hat{\mathbf{n}}'_i$ are the cosines of the angle between the bulk velocity of the emitting fluid ($\boldsymbol{\beta}$) and the direction of the interacting photon in the lab frame ($\hat{\mathbf{n}}_i$) and in the comoving frame of the emitting fluid ($\hat{\mathbf{n}}'_i$), respectively. Furthermore,

$$\mu'_i = \frac{\mu_i - \beta}{1 - \beta\mu_i} \implies \frac{d\Omega'_i}{d\Omega_r} = \frac{d\Omega'_i}{d\Omega_i} = \frac{d\mu'}{d\mu} = \delta^2, \quad (25)$$

since $d\Omega_i = d\phi_i d\mu_i$ and $\phi'_i = \phi_i$. We are interested in the differential density of photons of energy ε_i and direction of motion in the solid angle $d\Omega_r$, around the direction $\hat{\mathbf{n}}_i$, which is at an angle θ_r from the radial direction, at a radius R_t and time t_t . This density is related to the specific intensity of the photon field by

$$I_{\varepsilon_i}(\hat{\mathbf{n}}_i) \equiv \frac{dE}{dS dt d\varepsilon_i d\Omega_i} = \varepsilon_i m_e c^3 \frac{dn_i}{d\varepsilon_i d\Omega_r}(\hat{\mathbf{n}}_i), \quad (26)$$

where the (*normalized*) specific intensity I_{ε_i} is the energy (dE) per unit normal area (dS where $dS/dS = \hat{\mathbf{n}}$), per unit time (dt), per unit (*normalized*) photon energy ($d\varepsilon_i$), per solid angle ($d\Omega_i = d\Omega_r$) around some direction $\hat{\mathbf{n}}_i$ of the (potentially interacting) photons.

The differential (*normalized*) specific luminosity (in our case, from a small part of the emitting shell) is defined as $dL_{\varepsilon_i} = dE/d\varepsilon_i dt$, while the isotropic equivalent (*normalized*) specific luminosity is defined by

$$dL_{\varepsilon_i, \text{iso}} \equiv 4\pi \frac{dL_{\varepsilon_i}}{d\Omega_r}. \quad (27)$$

The contribution of an emitting element with $dL_{\varepsilon_i, \text{iso}}$ to the (*normalized*) flux density $dF_{\varepsilon_i} \equiv dE/dS dt d\varepsilon_i$ and to the (*normalized*) specific intensity I_{ε_i} at a point located at a distance r from it is

$$dF_{\varepsilon_i} = \frac{dL_{\varepsilon_i, \text{iso}}}{4\pi r^2} = I_{\varepsilon_i}(\hat{\mathbf{n}}) d\Omega_r \quad (28)$$

and is along the direction $\hat{\mathbf{n}}$ from the emitting element to that point (i.e., here dS is the differential of the area normal to $\hat{\mathbf{n}}$, $dS = \hat{\mathbf{n}} \cdot d\mathbf{S}$). Finally, we can conveniently express $dL_{\varepsilon_i, \text{iso}}$ in the comoving frame (i.e., the local rest frame of the emitting shell),

$$dL_{\varepsilon_i, \text{iso}} = 4\pi \frac{dL_{\varepsilon_i}}{d\Omega_r} = 4\pi \frac{dE}{d\varepsilon_i dt d\Omega_i} = \delta^3 4\pi \frac{dE'}{d\varepsilon' dt' d\Omega'_i} = \delta^3 dL'_{\varepsilon'_i}, \quad (29)$$

where the last equality follows from the assumption that the emission is isotropic in the comoving frame. Because the emission is assumed to be uniform throughout the shell, $dL'_{\varepsilon'_i}$ depends only on the radius of emission of the potentially interacting photon, R_e , and not on the location within the shell. Apart from the emission radius, R_e , the position of an emitting point on the shell is also specified by the polar angle, θ_e , which for convenience is measured with respect to the direction from the center of the sphere to the location of the test photon (at a radius R_t) where the flux (or some other property of the photon field) is calculated (see Fig. 2). As a result, we can write $dL'_{\varepsilon'_i} = L'_{\varepsilon'_i}(R_e) d\mu_e/2$, where $\mu_e = \cos \theta_e$ and $L'_{\varepsilon'_i}(R_e)$ has been defined and discussed in § 2. We finally combine equations (26), (28), and (29) to obtain the expressions for the normalized specific intensity,

$$I_{\varepsilon_i} = \frac{L'_{\varepsilon'_i}(R_e)}{4\pi} \frac{\delta^3}{4\pi r^2} \left| \frac{d\mu_e}{d\mu_r} \right|, \quad (30)$$

and the expression for the photon field which appears in the integrand in equation (23),

$$\frac{dn_i}{d\varepsilon_i d\Omega_r} = \frac{L'_{\varepsilon'_i}(R_e)}{(4\pi)^2 \varepsilon_i m_e c^3 r^2} \left| \frac{d\mu_e}{d\mu_r} \right|. \quad (31)$$

The derivative in the last term to the right of these equations must be computed along the equal arrival time surface (EATS-II) of photons to R_t at t_t , where I_{ε_i} or $dn_i/d\varepsilon_i d\Omega_r$ are to be calculated. We can now rewrite equation (23) as

$$\tau_{\gamma\gamma}(\varepsilon_t, \theta_{t,0}, R_{t,0}) = \frac{\sigma_T}{(4\pi)^2 m_e c^3} \int ds \int d\varepsilon_i \int d\Omega_r \frac{\sigma^*(\chi(\varepsilon_t, \varepsilon_i, \mu_{ti}))}{\sigma_T} (1 - \mu_{ti}) \frac{L'_{\varepsilon_i}(R_e) \delta^3}{\varepsilon_i r^2} \left| \frac{d\mu_e}{d\mu_r} \right|. \quad (32)$$

We have thus replaced the photon field by the specific emissivity in the expression for the optical depth. The boundaries of integration will be specified explicitly later on. We now want to simplify this triple integration in order to make it easier to evaluate.

3.2. Analytical Reduction

In the remainder of this work, we will make use of various dimensionless radii, which are gathered in Table 1 and greatly simplify the analysis. Furthermore, it is much more convenient to work with such quantities of order unity inside the integrand. We thus rescale R_e and R_t by introducing $\tilde{R}_e \equiv R_e/R_t$ and $\hat{R}_t \equiv R_t/R_{t,0}$. Furthermore, the notations $\tilde{R} \equiv R/R_t$ and $\hat{R} \equiv R/R_{t,0}$ will be used for other rescaled dimensionless radii as well. While clearly $1 \leq \hat{R}_t < \infty$, the range of \tilde{R}_e is much more complex and will be extensively discussed in § 4. For now, we want to simplify equation (32) by changing integration variables. We give here the main results and leave the details of the derivations for Appendix A.

As has been mentioned above, the integration over ds can be replaced by an integration over \hat{R}_t . Under the approximation of large Lorentz factors ($\Gamma \gg 1$), and thus small emission angles ($\theta_{t,0} \ll 1$), one obtains $ds = R_{t,0} d\hat{R}_t$ (see the discussion following eq. [A2] for more details). Besides, since we integrate over $d\Omega_r = d\phi_r d\mu_r$, and the integrand contains $|d\mu_e/d\mu_r|$ we can conveniently change the integration over μ_r to an integration over \tilde{R}_e . We show in the Appendix A that

$$\left| \frac{d\mu_e}{d\mu_r} \right| d\mu_r = \frac{d\mu_e}{d\tilde{R}_e} d\tilde{R}_e, \quad (33)$$

since $d\mu_e/d\tilde{R}_e > 0$, where the limit of integration over \tilde{R}_e should be in increasing order (i.e., the integration should be from small to large values of \tilde{R}_e). The optical depth now reads

$$\tau_{\gamma\gamma}(\varepsilon_t, \theta_{t,0}, R_{t,0}) \approx \frac{\sigma_T}{(4\pi)^2 m_e c^3 R_{t,0}} \int_1^\infty \frac{d\hat{R}_t}{\hat{R}_t^2} \int_{2/\varepsilon_i}^\infty d\varepsilon_i \int_0^{2\pi} d\phi_r \int_{R_0/R_t} d\tilde{R}_e \frac{\sigma^*[\chi(\varepsilon_t, \varepsilon_i, \mu_{ti})]}{\sigma_T} (1 - \mu_{ti}) \frac{L'_{\varepsilon_i}(R_e) \delta^3}{\varepsilon_i \tilde{r}^2} \frac{d\mu_e}{d\tilde{R}_e}. \quad (34)$$

Next, we can follow the hindsight of Stepney & Guilbert (1983) and Baring (1994) in order to cast the integrations over $(d\phi_r, d\varepsilon_i)$ into a much more practical form. In order to perform this change of variables, it is necessary to specialize the specific luminosity to the dependence discussed in § 2, $L'_{\varepsilon_i}(R_e) = L'_0 h(R_e/R_0) (\varepsilon'_i)^{1-\alpha} \equiv \Gamma_0^{-\alpha} L_0 (\varepsilon'_i)^{1-\alpha} h(\tilde{R}_e \hat{R}_t / \hat{R}_0)$, where h is a general function of R_e/R_0 that satisfies $h(1) = 1$ (for details see Appendix A.3) and $L'_0 \equiv L'_{\varepsilon'_i=1}(R_0)$. Note that $L_0 \equiv \Gamma_0^\alpha L'_0$ is approximately the observed isotropic equivalent luminosity at a photon energy of $m_e c^2 \approx 511$ keV, near the peak of the spike in the light curve which corresponds to the emission episode that we model for $\Delta R \sim R_0$.

For convenience, we rescale all the quantities in the integrand of equation (34) which are not of order unity by the relevant power of the Lorentz factor at radius R_t , $\Gamma_t = \Gamma(R_t)$, so that the rescaled quantities (which are denoted by a bar) will be of order unity. We rescale $\bar{\delta} \equiv \delta/\Gamma_t$ and $d\bar{\mu}_e \equiv \Gamma_t^2 d\mu_e$, but do not rescale \tilde{r} which is already of order unity. Thus,

$$\frac{\delta^{2+\alpha}}{\tilde{r}^2} \frac{d\mu_e}{d\tilde{R}_e} = \Gamma_0^\alpha \left(\frac{\hat{R}_t}{\hat{R}_0} \right)^{-m\alpha/2} \frac{\bar{\delta}^{2+\alpha}}{\tilde{r}^2} \frac{d\bar{\mu}_e}{d\tilde{R}_e}, \quad (35)$$

and the expression for the optical depth becomes

$$\tau_{\gamma\gamma}(\varepsilon_t, \theta_{t,0}, R_{t,0}) = \tau_* \varepsilon_t^{\alpha-1} \hat{R}_0^{1-m\alpha/2} \int_1^\infty \frac{d\hat{R}_t}{\hat{R}_t^{2-m\alpha/2}} \int d\tilde{R}_e \frac{\bar{\delta}^{2+\alpha}}{\tilde{r}^2} \frac{d\bar{\mu}_e}{d\tilde{R}_e} h\left(\tilde{R}_e \frac{\hat{R}_t}{\hat{R}_0}\right) \bar{\zeta}_-^\alpha H_\alpha(\zeta), \quad (36)$$

where

$$\tau_* (\Gamma_0^{2\alpha} R_0, \alpha, L_0) = \frac{7\sigma_T}{48\pi^3 m_e c^3} \frac{\Gamma_0^{-2\alpha} L_0}{\alpha^{5/3} R_0} = 0.402 \left(\frac{\alpha}{2} \right)^{-5/3} 10^{4(2-\alpha)} \frac{L_{0,52}}{(\Gamma_{0,2})^{2\alpha} R_{0,13}}, \quad (37)$$

$L_{0,52} = L_0/(10^{52} \text{ erg s}^{-1})$, $R_{0,13} = R_0/(10^{13} \text{ cm})$, $\Gamma_{0,2} = \Gamma_0/100$, $\zeta = (\zeta_+ - \zeta_-)/\zeta_-$, $\zeta_+ = [1 - \cos(\theta_r + \theta_t)]/2$, $\zeta_- = [1 - \cos(\theta_r - \theta_t)]/2$, and $H_\alpha(\zeta)$ is a function discussed in Appendix A.3. In equation (37), τ_* , the only quantity requiring astrophysical input, is a constant of the order of the optical depth to pair production at a photon energy of $m_e c^2$ at R_0 in quasi-steady state (near the peak of the spike in the light curve for $\Delta R \sim R_0$). Note that since both the photon index α and L_0 (roughly the isotropic equivalent luminosity) are observable quantities (the latter requiring knowledge of the source redshift), the observation of a high-energy spectral cutoff due to pair

production opacity can enable the determination of $\Gamma_0^{2\alpha} R_0$. In the limit of small angles that is appropriate for large Lorentz factors, ζ_- is of order Γ^{-2} , so we define $\tilde{\zeta}_- \equiv \Gamma_t^2 \zeta_-$, where $\Gamma_t = \Gamma(R_t) = \Gamma_0 \hat{R}_t^{-m/2}$. Thus,

$$\zeta_-^\alpha = \Gamma_0^{-2\alpha} \left(\frac{\hat{R}_t}{\hat{R}_0} \right)^{m\alpha} (\tilde{\zeta}_-)^\alpha. \quad (38)$$

Under the assumption that h is also a power law of index b , $h(R_e) = (R_e/R_0)^b = (\tilde{R}_e \hat{R}_t / \hat{R}_0)^b$, the expression for the optical depth in our model simplifies to

$$\tau_{\gamma\gamma}(\varepsilon_t, \theta_{t,0}, R_{t,0}) = \tau_0(\varepsilon_t, R_{t,0}) \mathcal{F}(x), \quad (39)$$

$$\tau_0(\varepsilon_t, R_{t,0}) = \tau_* \varepsilon_t^{\alpha-1} \hat{R}_0^{1-b-m\alpha/2}, \quad (40)$$

$$\mathcal{F}(x) = \int_1^\infty d\hat{R}_t \hat{R}_t^{b-2+m\alpha/2} \int d\tilde{R}_e \frac{\delta^{2+\alpha}}{\tilde{r}^2} \frac{d\tilde{\mu}_e}{d\tilde{R}_e} \tilde{R}_e^b \tilde{\zeta}_-^\alpha H_\alpha(\zeta). \quad (41)$$

In order to proceed further, we need to obtain an explicit expression for the innermost integrand of \mathcal{F} by a detailed examination of the geometry of the photon field. Section 4 is devoted to this analysis, which constitutes the main novelty of this work. We evaluate the optical depth (eq. [39]), taking into account that the photon field is not homogeneous along the test photon trajectory, but the contribution to the photon field is actually built up in time.

4. CALCULATING THE PHOTON FIELD

4.1. Equal Arrival Time Surface of Photons to the Test Photon (EATS-II)

In this section we calculate the photon field at a general radius R_t and time t_t , along the trajectory of a test photon. For this purpose we need to consider the contribution from all photons that arrive at the instantaneous location of the test photon, (R_t, t_t) , simultaneously. The locus of points where all such photons are emitted, taking into account that the emission occurs only in the shell, forms a two-dimensional surface referred to as the equal arrival time surface (EATS-II) of photons to the instantaneous location of the test photon. The local photon field at (R_t, t_t) is calculated by integrating the contributions over this surface. We stress that this surface (EATS-II) is different from the equal arrival time surface of photons to the observer at infinity (EATS-I).

Figure 1 shows the basic configuration for our calculations and illustrates the relation between the two different equal arrival time surfaces (EATS) of photons: (1) to the observer at infinity (EATS-I) and (2) to the instantaneous location of a test photon (EATS-II). It can be seen that the EATS-II grows with the lab frame time t and, therefore, also with the radius of the test photon R_t . Furthermore, each EATS-II encompasses all other EATS-II corresponding to smaller times and is encompassed within all the EATS-II which correspond to larger times. In particular, all EATS-II are within the EATS-I, which corresponds to the limit of the EATS-II for an infinite time (when the test photon reaches the observer at infinity). All of the EATS-II and EATS-I pass through the emission point of the test photon and, for cases 2 and 3, also through the place where the photon crosses the shell (i.e., its location in case 2). These are general properties of the EATS-II.

We now proceed to calculate the EATS-II and the expressions for relevant quantities along this surface, which are needed in order to calculate the local radiation field. From the geometry of our problem (see Fig. 2), we can immediately derive the two following equations,

$$\tilde{r}^2 = 1 + \tilde{R}_e^2 - 2\tilde{R}_e\mu_e = (1 - \tilde{R}_e)^2 + 2\tilde{R}_e(1 - \mu_e), \quad (42)$$

$$\tilde{R}_e^2 = 1 + \tilde{r}^2 - 2\tilde{r}\mu_r, \quad (43)$$

where $\tilde{R}_e \equiv R_e/R_t$ and $\tilde{r} \equiv r/R_t$. The EATS-II of photons to (R_t, t_t) is determined by the condition that $r = c(t_t - t_e) = c[t_t - t_{\text{sh}}(R_e)]$, where the photons are emitted at a previous time t_e when the shell is at a radius $R_e = R_{\text{sh}}(t_e)$. The EATS-II equation is thus given by

$$\tilde{r} = \frac{c}{R_t} [t_t - t_{\text{sh}}(R_e)] = \sqrt{(1 - \tilde{R}_e)^2 + 2\tilde{R}_e(1 - \mu_e)}, \quad (44)$$

which relates the radius (R_e) and angle ($\theta_e = \arccos \mu_e$) of emission along this surface.

The expression for $t_{\text{sh}}(R_e)$ depends on our assumption about the expansion of the shell. If the latter occurs at constant speed, then $t_{\text{sh}}(R_e) = R_e/\beta c$ and in the limit of $R_t \rightarrow \infty$ equation (44) reduces to $\beta(ct_t - R_t) = R_e(1 - \beta\mu_e)$, which is the usual polar equation of an ellipse (setting $cT = ct_t - R_t$). In this simple case, using the short notation $\tilde{R}_{\text{sh}} = \tilde{R}_{\text{sh}}(t_t)$ we have $\tilde{r} = (\tilde{R}_{\text{sh}} - \tilde{R}_e)/\beta$, and the EATS-II is given by

$$\mu_e = 1 - \frac{1}{2\beta^2\tilde{R}_e} \left[(\tilde{R}_{\text{sh}} - \tilde{R}_e)^2 - \beta^2(1 - \tilde{R}_e)^2 \right], \quad (45)$$

while the lower and upper limits for the range of \tilde{R}_e values along the EATS-II, which correspond to $\mu_e = -1$ and $\mu_e = 1$, respectively, are given by

$$\tilde{R}_{e,\text{min}} = \frac{\tilde{R}_{\text{sh}} - \beta}{1 + \beta}, \quad \tilde{R}_{e,\text{max}} = \begin{cases} (\tilde{R}_{\text{sh}} + \beta)/(1 + \beta), & \tilde{R}_{\text{sh}} \geq 1, \\ (\tilde{R}_{\text{sh}} - \beta)/(1 - \beta), & \tilde{R}_{\text{sh}} \leq 1. \end{cases} \quad (46)$$

Note that we have not assumed $\Gamma = (1 - \beta^2)^{-1/2} \gg 1$, so these results are valid for an arbitrary velocity, as long as it is constant with radius.

Combining equations (42) and (43) we also obtain

$$\mu_r = \frac{1 - \tilde{R}_e \mu_e}{\sqrt{(1 - \tilde{R}_e)^2 + 2\tilde{R}_e(1 - \mu_e)}} = \frac{R_t}{c} \left[\frac{1 - \tilde{R}_e \mu_e}{t_t - t_{sh}(R_e)} \right], \tag{47}$$

where in the last equality we have also used equation (44), so that it is valid only along the EATS-II (while the first equality is valid more generally, as it is derived directly from the geometrical setup).

4.2. Radial Dependence of Relevant Angles, $\mu_e(\tilde{R}_e)$ and $\mu_r(\tilde{R}_e)$, along EATS-II

Specifying for $1 \ll \Gamma^2 = \Gamma_t^2 \tilde{R}^{-m}$, we can rewrite equation (5) as

$$t_{sh}(R) = \frac{R_t}{c} \left[\tilde{R} + \frac{\tilde{R}^{m+1}}{2(m+1)\Gamma_t^2} \right] + O(\Gamma_t^{-4}). \tag{48}$$

Thus, equation (44) implies

$$\tilde{r} = \tilde{R}_{sh} - \tilde{R}_e + \frac{(\tilde{R}_{sh}^{m+1} - \tilde{R}_e^{m+1})}{2(m+1)\Gamma_t^2} + O(\Gamma_t^{-4}), \tag{49}$$

$$\tilde{r}^2 = (\tilde{R}_{sh} - \tilde{R}_e)^2 + \frac{(\tilde{R}_{sh} - \tilde{R}_e)(\tilde{R}_{sh}^{m+1} - \tilde{R}_e^{m+1})}{(m+1)\Gamma_t^2} + O(\Gamma_t^{-4}). \tag{50}$$

Note that $\tilde{R}_e \leq \tilde{R}_{sh}$, because $t_e \leq t_t$ (due to causality) and $R_{sh}(t)$ is an increasing function of t . The equality only holds when $R_t = R_{sh}(t_t)$, i.e., when $\tilde{R}_{sh} = 1$ (case 2 below). Thus, equations (42) and (50) give (to the order of Γ_t^{-2})

$$2\Gamma_t^2(1 - \mu_e) = (\Gamma_t \theta_e)^2 = \frac{1}{\tilde{R}_e} \left\{ \Gamma_t^2 [(\tilde{R}_{sh} - \tilde{R}_e)^2 - (1 - \tilde{R}_e)^2] + \frac{(\tilde{R}_{sh} - \tilde{R}_e)(\tilde{R}_{sh}^{m+1} - \tilde{R}_e^{m+1})}{(m+1)} \right\}. \tag{51}$$

The two terms on the right-hand side of the equation are typically of the same order, since $|\tilde{R}_{sh} - 1| \lesssim \text{a few } \Gamma_t^{-2}$, i.e., $\tilde{R}_{sh} \cong 1 \Leftrightarrow R_{sh}(t_t) \cong R_t$. This immediately implies

$$\frac{d\mu_e}{d\tilde{R}_e} = \frac{1}{2\Gamma_t^2 \tilde{R}_e^2} \left[\Gamma_t^2 (\tilde{R}_{sh}^2 - 1) + \frac{\tilde{R}_{sh}}{m+1} (\tilde{R}_{sh}^{m+1} + m\tilde{R}_e^{m+1}) - \tilde{R}_e^{m+2} \right]. \tag{52}$$

Now we turn to μ_r . From equations (43) and (50) we obtain

$$\mu_r = \frac{(\tilde{R}_{sh} - \tilde{R}_e)^2 + (1 - \tilde{R}_e^2)}{2(\tilde{R}_{sh} - \tilde{R}_e)} + \frac{(\tilde{R}_{sh}^{m+1} - \tilde{R}_e^{m+1})}{4(m+1)\Gamma_t^2} \left[1 - \frac{1 - \tilde{R}_e^2}{(\tilde{R}_{sh} - \tilde{R}_e)^2} \right] + O(\Gamma_t^{-4}), \tag{53}$$

$$\frac{d\mu_r}{d\tilde{R}_e} = -\frac{d\tilde{r}}{d\tilde{R}_e} \left[\frac{1 - \tilde{R}_e^2 - \tilde{r}^2}{2\tilde{r}^2} \right] - \frac{\tilde{R}_e}{\tilde{r}} = \frac{1 - \tilde{R}_{sh}^2}{2(\tilde{R}_{sh} - \tilde{R}_e)^2} + \frac{\tilde{R}_e^m}{4\Gamma_t^2} \left[\frac{1 - \tilde{R}_e^2}{(\tilde{R}_{sh} - \tilde{R}_e)^2} - 1 \right] + \frac{(\tilde{R}_{sh}^{m+1} - \tilde{R}_e^{m+1})(\tilde{R}_{sh}\tilde{R}_e - 1)}{2(m+1)\Gamma_t^2(\tilde{R}_{sh} - \tilde{R}_e)^3} + O(\Gamma_t^{-4}), \tag{54}$$

where

$$-\frac{d\tilde{r}}{d\tilde{R}_e} = 1 + \frac{\tilde{R}_e^m}{2\Gamma_t^2} = 1 + \frac{1}{2\Gamma^2(\tilde{R}_e)} = \frac{1}{\beta(\tilde{R}_e)}. \tag{55}$$

This can easily be understood since $r = c(t_t - t_e)$ along the EATS, so that $dr = -c dt_e$ and $d\tilde{r}/d\tilde{R}_e = dr/dR_e = -c dt_e/dR_e = -c/(dR_e/dt_e) = -1/\beta(\tilde{R}_e)$.

The maximal radius of emission, $R_{e, \max}$, from which a photon reaches a point at radius R_t at the time t_t is determined by the photon that is emitted at $\theta_e = 0$ (i.e., $\mu_e = 1$), along the line connecting that point to the center of the sphere. Thus,

$$\tilde{r}_{\min} = |1 - \tilde{R}_{e, \max}| = \frac{c}{R_t} [t_t - t_{sh}(\tilde{R}_{e, \max})] \tag{56}$$

$$= \tilde{R}_{sh} - \tilde{R}_{e, \max} + \frac{(\tilde{R}_{sh}^{m+1} - \tilde{R}_{e, \max}^{m+1})}{2(m+1)\Gamma_t^2} + O(\Gamma_t^{-4}), \tag{57}$$

and the problem naturally divides into three cases.

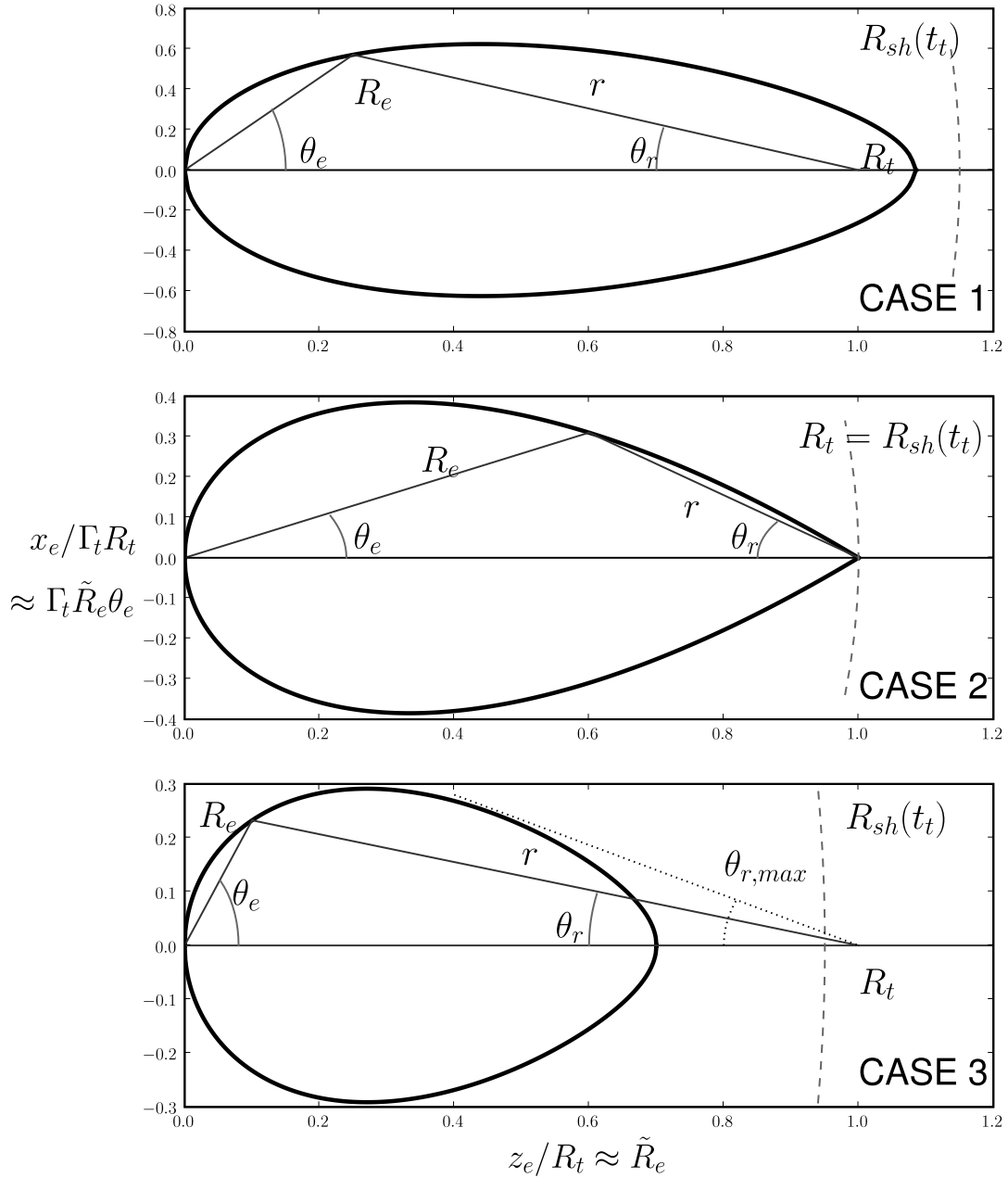


FIG. 3.—Equal arrival time surface (EATS-II) of photons to (R_t, t_t) , which represents a general point along the trajectory of a test photon, is shown by the thick blue line. It naturally divides into three cases (1) the test photon is behind the shell [$R_t < R_{sh}(t_t)$, *top*], (2) the test photon coincides with the shell [$R_t = R_{sh}(t_t)$, *middle*], and (3) the test photon is ahead of the shell [$R_t > R_{sh}(t_t)$, *bottom*]. There are qualitative difference in the properties of the EATS-II between these different cases that are discussed in the text. [See the electronic edition of the *Journal* for a color version of this figure.]

4.3. Properties of EATS-II According to Relative Location of Test Photon and Shell

The properties of the EATS-II qualitatively change according to the location of the test photon relative to the shell at the same lab frame time, t_t . Thus, the problem naturally divides into three cases, as illustrated in Figures 1 and 3. If the photon is emitted at an angle⁷ $\theta_{t,0} > 1/\Gamma_{t,0}$, i.e., $x \equiv (\Gamma_{t,0}\theta_{t,0})^2 > 1$, it initially lags behind the shell (case 1), since due to the aberration of light (also referred to as relativistic beaming) this corresponds to an angle greater than 90° from the radial direction in the comoving frame of the shell. The photon eventually catches up with the shell and crosses it (case 2), since the latter is moving at a velocity slightly smaller than the speed of light. After it crosses the shell, it remains ahead of the shell (case 3). A photon that is emitted at $\theta_{t,0} \leq 1/\Gamma_{t,0}$, corresponding to $x \leq 1$, immediately gets ahead of the shell (case 3). All photons are always emitted at the shell, so the point of emission is considered case 2. Like the later shell crossing for photons with $x > 1$, case 2 corresponds to a single point along that trajectory of the test photon, unlike case 1 which corresponds to a finite path along the trajectory, and case 3 corresponds to a (practically) semi-infinite interval (as far as the observer is considered to be at “infinity”); the contribution to the opacity at large distances from the source, however, becomes

⁷ More generally, the condition is $\cos \theta_{t,0} < \beta$, but for $\Gamma_{t,0} \gg 1$ and $\theta_{t,0} \ll 1$ this reduces to $\theta_{t,0} > 1/\Gamma_{t,0}$.

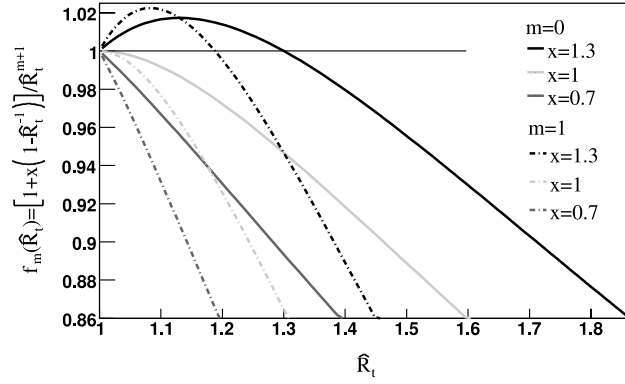


FIG. 4.—Plots of $f_m(\hat{R}_t)$, defined in eq. (64), as a function of \hat{R}_t , for $m = 0$ and 1 . The test photon is necessarily on the shell at the time of its emission, so that all the curves meet at $f_m(1) = 1$. [See the electronic edition of the Journal for a color version of this figure.]

negligible). The three different cases are discussed in detail below, and the relevant expressions for each case are derived. We start by defining some useful quantities for this purpose, which will be very helpful later on.

In the limit of small angles, equation (A1) yields

$$(\Gamma_t \theta_t)^2 \approx x \hat{R}_t^{-m-2}, \quad (58)$$

where $x \equiv (\Gamma_{t,0} \theta_{t,0})^2$ is the square of the normalized emission angle of the test photon. Evaluating equation (48) at $\tilde{R}_{\text{sh}} = \tilde{R}_{\text{sh}}(t_t)$ gives

$$\frac{ct_t}{R_t} = \tilde{R}_{\text{sh}} + \frac{\tilde{R}_{\text{sh}}^{m+1}}{2(m+1)\Gamma_t^2} + O(\Gamma_t^{-4}), \quad (59)$$

which can be rewritten in terms of the quantity

$$f_m \equiv 2(m+1)\Gamma_t^2 \left(\frac{ct_t}{R_t} - 1 \right) = 2(m+1)\Gamma_t^2 (\tilde{R}_{\text{sh}} - 1) + \tilde{R}_{\text{sh}}^{m+1} + O(\Gamma_t^{-2}), \quad (60)$$

which plays a major role in the following derivations.

For an emission episode starting at $R_0 = 0$, the inequality $ct_t > R_t$ is required in order to have a nonvanishing radiation field at the point (R_t, t_t) . If the emission turns on at a nonzero radius R_0 , this condition generalizes to

$$\frac{ct_t}{R_t} - 1 \geq \frac{\tilde{R}_0}{2(m+1)\Gamma^2(R_0)} = \frac{\tilde{R}_0^{m+1}}{2(m+1)\Gamma_t^2}. \quad (61)$$

This implies that $f_m > 0$ (for $m > -1$, which is assumed in this work, and is typically the case for the astrophysical sources of interest).

We note that $f_m < 1$ for $\tilde{R}_{\text{sh}} < 1$ (when the test photon is traveling in front of the shell), $f_m > 1$ for $\tilde{R}_{\text{sh}} > 1$ (when the test photon is traveling behind the shell), and $f_m = 1$ for $\tilde{R}_{\text{sh}} = 1$ (when the test photon is at the shell). It is convenient to express f_m as a function of our primary variables. Using

$$R_t^2 = R_\perp^2 + z^2 = R_{t,0}^2 \sin^2 \theta_{t,0} + [R_{t,0} \cos \theta_{t,0} + c(t_t - t_0)]^2, \quad (62)$$

where R_\perp is the distance between the line of sight to the origin and the trajectory of the test photon (see Fig. 1 and eq. [A1]), and solving this second-order equation, one obtains

$$\frac{c(t_t - t_0)}{R_{t,0}} = (\hat{R}_t - 1) \left(1 + \frac{\theta_{t,0}^2}{2\hat{R}_t} \right) + O(\theta_{t,0}^4). \quad (63)$$

Recalling that $ct_0/R_{t,0} = 1 + 1/2(m+1)\Gamma_{t,0}^2 + O(\Gamma_{t,0}^{-4})$, we finally obtain

$$f_m(\hat{R}_t) \equiv 2(m+1)\Gamma_t^2 \left(\frac{ct_t}{R_t} - 1 \right) = \frac{1 + x(m+1)(1 - \hat{R}_t^{-1})}{\hat{R}_t^{m+1}} + O(\Gamma^{-4}). \quad (64)$$

Figure 4 shows the dependence of $f_m(\hat{R}_t)$ on the parameter $x \equiv (\Gamma_{t,0} \theta_{t,0})^2$. For $\hat{R}_t = 1$ we always have $f_m = 1$, since the test photon is emitted at the shell. For $x > 1$ the photon initially lags behind the shell (case 1), and the equation $f_m = 1$ that can be expressed as $\hat{R}_t^{m+2} - [1 + (m+1)x]\hat{R}_t + (m+1)x = 0$ has an additional nontrivial solution, \hat{R}_2 , which corresponds to the point where the photon crosses the shell. For $m = 0$ and 1 , it is given by $\hat{R}_2 = x$ and $[(1 + 8x)^{1/2} - 1]/2$, respectively.

4.3.1. Case 1: Test Photon behind the Shell, $R_t < R_{\text{sh}}(t_i)$

In this case,

$$R_t < R_{e,\text{max}} < R_{\text{sh}}(t_i) \lesssim R_t \left(1 + \frac{\text{a few}}{\Gamma_t^2} \right) \Leftrightarrow 1 < \tilde{R}_{e,\text{max}} < \tilde{R}_{\text{sh}}(t_i) \lesssim 1 + \frac{\text{a few}}{\Gamma_t^2}, \quad (65)$$

where the last approximate inequality holds for emission angles $(\Gamma_t \theta_e)^2 \lesssim \text{a few}$, from which most of the contribution to the observed flux arises, and are therefore the ones of relevance. An expression for $\tilde{R}_{\text{sh}}(t_i)$ may readily be obtained through (see eq. [48])

$$\tilde{R}_{\text{sh}}(t_i) = \frac{ct_i}{R_t} \left\{ 1 - \frac{[\tilde{R}_{\text{sh}}(t_i)]^m}{2(m+1)\Gamma_t^2} \right\} + O(\Gamma_t^{-4}) = \frac{ct_i}{R_t} - \frac{1}{2(m+1)\Gamma_t^2} + O(\Gamma_t^{-4}), \quad (66)$$

while $\tilde{R}_{e,\text{max}}$ is obtained by equating the two expressions for \tilde{r} , from equations (49) and (42) for $\mu_e = 1$,

$$\tilde{r}_{\text{min}} = \tilde{R}_{e,\text{max}} - 1 = \tilde{R}_{\text{sh}} - \tilde{R}_{e,\text{max}} + \frac{(\tilde{R}_{\text{sh}}^{m+1} - \tilde{R}_{e,\text{max}}^{m+1})}{2(m+1)\Gamma_t^2} + O(\Gamma_t^{-4}) = \tilde{R}_{\text{sh}} - \tilde{R}_{e,\text{max}} + O(\Gamma_t^{-4}), \quad (67)$$

which implies

$$2(\tilde{R}_{e,\text{max}} - 1) \approx (\tilde{R}_{\text{sh}} - 1) \approx \left(\frac{ct_i}{R_t} - 1 \right) - \frac{1}{2(m+1)\Gamma_t^2} \quad (68)$$

$$\Rightarrow \tilde{R}_{e,\text{max}} = \frac{1}{2} \left(\frac{ct_i}{R_t} + 1 \right) - \frac{1}{4(m+1)\Gamma_t^2} + O(\Gamma_t^{-4}) \approx \frac{\tilde{R}_{\text{sh}} + 1}{2}. \quad (69)$$

While θ_e is always small, $(\Gamma_t \theta_e)^2 \lesssim \text{a few}$, in the case studied in this subsection θ_r can range from zero to π and it is not obvious a priori whether it can be taken to be either large, $(\Gamma_t \theta_r)^2 \gg 1$, or small, $(\Gamma_t \theta_r)^2 \lesssim \text{a few}$. We argue that when θ_r is large, the photons must be emitted at a large angle relative to the direction of motion of the emitting shell ($\theta_i = \theta_r + \theta_e$) and are therefore significantly suppressed by relativistic beaming. This effect wins over the increase in the reaction rate due to the larger angle between the test photon and the interacting photons, which is manifested by the factor of $(1 - \mu_{ii})$ in the integrand for the optical depth. Therefore, the dominant contributions to the optical depth occur from small θ_r values, and we can therefore make the approximations that are appropriate for $(\Gamma_t \theta_r)^2 \lesssim \text{a few}$. We express these considerations more quantitatively in Appendix B. Thus, we obtain

$$\begin{aligned} (\Gamma_t \theta_e)^2 &= 2\Gamma_t^2(1 - \mu_e) = \frac{(\tilde{R}_{e,\text{max}} - \tilde{R}_e)}{(m+1)\tilde{R}_e} \left[\tilde{R}_{e,\text{max}}^{m+1} - \tilde{R}_e^{m+1} + 4(m+1)\Gamma_t^2(\tilde{R}_{e,\text{max}} - 1) \right] + O(\Gamma_t^{-2}) \\ &= \frac{(1 - \tilde{R}_e)}{(m+1)\tilde{R}_e} [f_m(\hat{R}_t) - \tilde{R}_e^{m+1}] + O(\Gamma_t^{-2}), \end{aligned} \quad (70)$$

$$(\Gamma_t \theta_r)^2 = 2\Gamma_t^2(1 - \mu_r) = \frac{\tilde{R}_e [\tilde{R}_{\text{sh}}^{m+1} - \tilde{R}_e^{m+1} + 2(m+1)\Gamma_t^2(\tilde{R}_{\text{sh}} - 1)]}{(m+1)(\tilde{R}_{\text{sh}} - \tilde{R}_e)} + O(\Gamma_t^{-2}) = \frac{\tilde{R}_e [f_m(\hat{R}_t) - \tilde{R}_e^{m+1}]}{(m+1)(1 - \tilde{R}_e)} + O(\Gamma_t^{-2}), \quad (71)$$

$$\begin{aligned} \frac{d\mu_e}{d\tilde{R}_e} &= \frac{1}{2(m+1)\Gamma_t^2} \left\{ \frac{\tilde{R}_{e,\text{max}}}{\tilde{R}_e^2} \left[\tilde{R}_{e,\text{max}}^{m+1} - \tilde{R}_e^{m+1} + 4(m+1)\Gamma_t^2(\tilde{R}_{e,\text{max}} - 1) \right] + (m+1)\tilde{R}_e^{m-1}(\tilde{R}_{e,\text{max}} - \tilde{R}_e) \right\} \\ &= \frac{[f_m(\hat{R}_t) - \tilde{R}_e^{m+1} + (m+1)\tilde{R}_e^{m+1}(1 - \tilde{R}_e)]}{2(m+1)\Gamma_t^2 \tilde{R}_e^2}, \end{aligned} \quad (72)$$

$$\frac{d\mu_r}{d\tilde{R}_e} = \frac{(m+1)\tilde{R}_e^{m+1}(\tilde{R}_{\text{sh}} - \tilde{R}_e) - \tilde{R}_{\text{sh}}[\tilde{R}_{\text{sh}}^{m+1} - \tilde{R}_e^{m+1} + 2(m+1)\Gamma_t^2(\tilde{R}_{\text{sh}} - 1)]}{2(m+1)\Gamma_t^2(\tilde{R}_{\text{sh}} - \tilde{R}_e)^2} \approx \frac{[(m+1)\tilde{R}_e^{m+1}(1 - \tilde{R}_e) - f_m(\hat{R}_t) + \tilde{R}_e^{m+1}]}{2(m+1)\Gamma_t^2(1 - \tilde{R}_e)^2}. \quad (73)$$

We note that, as expected, $\mu_e(\tilde{R}_{e,\text{max}}) = 1$, since $(1 - \tilde{R}_e) = (\tilde{R}_{e,\text{max}} - \tilde{R}_e) + O(\Gamma_t^{-2})$ while $d\mu_e/d\tilde{R}_e > 0$. The Doppler factor is given by

$$\delta \approx \frac{2\Gamma}{1 + \Gamma^2(\theta_e + \theta_r)^2} = \frac{2(m+1)\Gamma_t \tilde{R}_e^{(m+2)/2} (1 - \tilde{R}_e)}{(m+1)\tilde{R}_e^{m+1} (1 - \tilde{R}_e) + f_m(\hat{R}_t) - \tilde{R}_e^{m+1}}, \quad (74)$$

where we have used equations (70) and (71) as well as $\Gamma^2 = \Gamma_t^2 \tilde{R}_e^{-m} \gg 1$ and $\theta_e + \theta_r \ll 1$. Finally, $\tilde{r} \approx 1 - \tilde{R}_e$, and thus,

$$\frac{\delta^{\alpha+2}}{\tilde{r}_e^2} \frac{d\mu_e}{d\tilde{R}_e} = \Gamma_t^\alpha \frac{\tilde{\delta}^{\alpha+2}}{\tilde{r}_e^2} \frac{d\tilde{\mu}_e}{d\tilde{R}_e} \approx \frac{2(2\Gamma_t)^\alpha (m+1)^{1+\alpha} \tilde{R}_e^{\alpha+m(\alpha+2)/2} (1 - \tilde{R}_e)^\alpha}{[(m+1)\tilde{R}_e^{m+1} (1 - \tilde{R}_e) + f_m(\hat{R}_t) - \tilde{R}_e^{m+1}]^{1+\alpha}}. \quad (75)$$

4.3.2. Case 2: Test Photon at the Shell, $R_t = R_{\text{sh}}(t_t)$

This is a limiting case between case 1 and case 3, when the test photon is located on the shell, $t_t = t_{\text{sh}}(\tilde{R}_{e,\text{max}})$, $\tilde{r}_{\text{min}} = 0$, and $\tilde{R}_{e,\text{max}} = 1$, i.e.,

$$R_{e,\text{max}} = R_{\text{sh}}(t_t) = R_t, \quad \tilde{R}_{e,\text{max}} = \tilde{R}_{\text{sh}}(t_t) = 1. \quad (76)$$

This means that the last emitted photons that still reach the point (R_t, t_t) are emitted at that same point in space and time, i.e., the EATS ends at that point. Therefore,

$$(\Gamma_t \theta_e)^2 = 2\Gamma_t^2(1 - \mu_e) = \frac{(1 - \tilde{R}_e)(1 - \tilde{R}_e^{m+1})}{(m+1)\tilde{R}_e}, \quad (77)$$

$$(\Gamma_t \theta_r)^2 = 2\Gamma_t^2(1 - \mu_r) = \frac{\tilde{R}_e(1 - \tilde{R}_e^{m+1})}{(m+1)(1 - \tilde{R}_e)}, \quad (78)$$

$$\frac{d\mu_e}{d\tilde{R}_e} = \frac{m\tilde{R}_e^{m+1}(1 - \tilde{R}_e) + (1 - \tilde{R}_e^{m+2})}{2(m+1)\Gamma_t^2\tilde{R}_e^2}, \quad (79)$$

$$\frac{d\mu_r}{d\tilde{R}_e} = -\frac{(1 - \tilde{R}_e^{m+2}) - (m+2)\tilde{R}_e^{m+1}(1 - \tilde{R}_e)}{2(m+1)\Gamma_t^2(1 - \tilde{R}_e)^2}. \quad (80)$$

In the limit where $\tilde{R}_e \approx 1$ (i.e., $1 - \tilde{R}_e \ll 1$) we have

$$(\Gamma_t \theta_e)^2 \approx (1 - \tilde{R}_e)^2, \quad (\Gamma_t \theta_r)^2 \approx 1 - \frac{m+2}{2}(1 - \tilde{R}_e), \quad (81)$$

$$\frac{d\mu_e}{d\tilde{R}_e} \approx \frac{1 - \tilde{R}_e}{\Gamma_t^2} \approx \frac{\theta_e}{\Gamma_t}, \quad \frac{d\mu_r}{d\tilde{R}_e} \approx -\frac{(m+2)}{4\Gamma_t^2}, \quad \frac{d\mu_e}{d\mu_r} \approx -\frac{4}{(m+2)}(1 - \tilde{R}_e). \quad (82)$$

In this limit $\tilde{r} \approx 1 - \tilde{R}_e$, which implies (see eq. [31]) that $I_\varepsilon \propto |d\mu_e/d\mu_r|/\tilde{r}^2 \propto (1 - \tilde{R}_e)^{-1}$, i.e., the specific intensity diverges at the angle $\theta_r = \theta_{r,\text{max}} = 1/\Gamma_t$ and vanishes above this angle. This can be understood as follows. In this limit $\tilde{r} \ll 1$, i.e., $r \ll R_t = R_{\text{sh}}(t_t)$ and the curvature of the shock front becomes unimportant, so that in order for a photon to reach the point (R_t, t_t) together with the shock front it must propagate along the shock front, which corresponds locally to an angle of $1/\Gamma$ (or more generally $\cos \theta = \beta$) from the normal to the shock front, i.e., the radial direction in our case.

4.3.3. Case 3: Test Photon Ahead of the Shell, $R_t > R_{\text{sh}}(t_t)$

With the causality condition $R_{e,\text{max}} < R_{\text{sh}}(t_t)$ and equation (61), we now have

$$R_0 \leq R_{e,\text{max}} < R_{\text{sh}}(t_t) < R_t < ct_t - \frac{R_t \tilde{R}_0^{m+1}}{2(m+1)\Gamma_t^2}, \quad (83)$$

$$\iff \tilde{R}_0 \leq \tilde{R}_{e,\text{max}} < \tilde{R}_{\text{sh}} < 1 \leq \frac{ct_t}{R_t} - \frac{\tilde{R}_0^{m+1}}{2(m+1)\Gamma_t^2}. \quad (84)$$

As a result, equation (57) yields

$$1 - \tilde{R}_{e,\text{max}} = \tilde{R}_{\text{sh}} - \tilde{R}_{e,\text{max}} + \frac{(\tilde{R}_{\text{sh}}^{m+1} - \tilde{R}_{e,\text{max}}^{m+1})}{2(m+1)\Gamma_t^2} + O(\Gamma^{-4}), \quad (85)$$

$$\iff 1 - \tilde{R}_{\text{sh}} = \frac{\tilde{R}_{\text{sh}}^{m+1} - \tilde{R}_{e,\text{max}}^{m+1}}{2(m+1)\Gamma_t^2} \leq \frac{\tilde{R}_{\text{sh}}^{m+1} - \tilde{R}_0^{m+1}}{2(m+1)\Gamma_t^2} < \frac{\tilde{R}_{\text{sh}}^{m+1}}{2(m+1)\Gamma_t^2} < \frac{1}{2(m+1)\Gamma_t^2}, \quad (86)$$

$$\tilde{R}_{e,\text{max}} = \tilde{R}_{\text{sh}} \left[1 - \frac{2(m+1)\Gamma_t^2}{\tilde{R}_{\text{sh}}^{m+1}} (1 - \tilde{R}_{\text{sh}}) \right]^{1/(m+1)} = \left[2(m+1)\Gamma_t^2 \left(\frac{ct_t}{R_t} - 1 \right) \right]^{1/(m+1)} = [f_m(\hat{R}_t)]^{1/(m+1)}. \quad (87)$$

Taking these results into account, we now derive the relevant expressions from equations (51)–(54). The leading terms for $1 - \mu_e$, $1 - \mu_r$, and their derivatives with respect to \tilde{R}_e are all of the order of $O(\Gamma_t^{-2})$. Thus, we obtain

$$(\Gamma_t \theta_e)^2 = 2\Gamma_t^2(1 - \mu_e) = \frac{(1 - \tilde{R}_e)(\tilde{R}_{e,\text{max}}^{m+1} - \tilde{R}_e^{m+1})}{(m+1)\tilde{R}_e} + O(\Gamma_t^{-2}) = \frac{(1 - \tilde{R}_e)[f_m(\hat{R}_t) - \tilde{R}_e^{m+1}]}{(m+1)\tilde{R}_e} + O(\Gamma_t^{-2}), \quad (88)$$

$$(\Gamma_t \theta_r)^2 = 2\Gamma_t^2(1 - \mu_r) = \frac{\tilde{R}_e(\tilde{R}_{e,\text{max}}^{m+1} - \tilde{R}_e^{m+1})}{(m+1)(1 - \tilde{R}_e)} + O(\Gamma_t^{-2}) = \frac{\tilde{R}_e[f_m(\hat{R}_t) - \tilde{R}_e^{m+1}]}{(m+1)(1 - \tilde{R}_e)} + O(\Gamma_t^{-2}), \quad (89)$$

and for the derivatives

$$\frac{d\mu_e}{d\tilde{R}_e} = \frac{(m+1)\tilde{R}_e^{m+1}(1-\tilde{R}_e) + [f_m(\hat{R}_t) - \tilde{R}_e^{m+1}]}{2(m+1)\Gamma_t^2\tilde{R}_e^2} + O(\Gamma_t^{-4}), \quad (90)$$

$$\frac{d\mu_r}{d\tilde{R}_e} = \frac{(m+1)\tilde{R}_e^{m+1}(1-\tilde{R}_e) - [f_m(\hat{R}_t) - \tilde{R}_e^{m+1}]}{2(m+1)\Gamma_t^2(1-\tilde{R}_e)^2} + O(\Gamma_t^{-4}). \quad (91)$$

The Doppler factor is given by

$$\delta \approx \frac{2\Gamma}{1 + \Gamma^2(\theta_e + \theta_r)^2} = \frac{2(m+1)\Gamma_t\tilde{R}_e^{(m+2)/2}(1-\tilde{R}_e)}{(m+1)\tilde{R}_e^{m+1}(1-\tilde{R}_e) + [f_m(\hat{R}_t) - \tilde{R}_e^{m+1}]}, \quad (92)$$

where we have used equations (88) and (89) as well as $\Gamma^2 = \Gamma_t^2\tilde{R}_e^{-m} \gg 1$ and $\theta_e + \theta_r \ll 1$. Finally, $\tilde{r} \approx 1 - \tilde{R}_e$, and thus,

$$\begin{aligned} \frac{\delta^{\alpha+2}}{\tilde{r}_e^2} \frac{d\mu_e}{d\tilde{R}_e} &= \Gamma_t^\alpha \frac{\tilde{\delta}^{\alpha+2}}{\tilde{r}_e^2} \frac{d\tilde{\mu}_e}{d\tilde{R}_e} \approx \frac{2(2\Gamma_t)^\alpha}{(1-\tilde{R}_e)\tilde{R}_e^{1+m\alpha/2}} \left[1 + \frac{f_m(\hat{R}_t) - \tilde{R}_e^{m+1}}{(m+1)\tilde{R}_e^{m+1}(1-\tilde{R}_e)} \right]^{-(1+\alpha)} \\ &\approx \frac{2(2\Gamma_t)^\alpha (m+1)^{1+\alpha} \tilde{R}_e^{\alpha+m(2+\alpha)/2} (1-\tilde{R}_e)^\alpha}{[(m+1)\tilde{R}_e^{m+1}(1-\tilde{R}_e) + f_m(\hat{R}_t) - \tilde{R}_e^{m+1}]^{1+\alpha}}. \end{aligned} \quad (93)$$

We note that the expressions above for case 3 are identical to those for case 1 (eq. [74]). While $dn_i/d\varepsilon_i d\Omega_r$ diverges as $|\tilde{R}_e - \tilde{R}_e(\theta_{r,\max})|^{-1} \propto |\theta_r - \theta_{r,\max}|^{-1/2}$ at $\theta_{r,\max}$, $dn_i/d\varepsilon_i = \int d\Omega_r (dn_i/d\varepsilon_i d\Omega_r) \approx 2\pi \int \theta_r d\theta_r (dn_i/d\varepsilon_i d\Omega_r)$ remains finite (i.e., both the energy density and the energy flux of the radiation field remain finite). This has been noticed in the context of the diverging surface brightness of the afterglow image at its outer edge, when the emission comes from an infinitely thin shell (Sari 1998; Granot & Loeb 2001). In that context, it has also been shown (Waxman 1997; Granot et al. 1999a, 1999b; Granot & Loeb 2001) that when the emission comes from a shell of finite width, the surface brightness (i.e., the specific intensity I_ε) does not diverge.

4.4. Putting It All Together

Analytical expressions for our model have now been fully derived, and are reported for convenience here. The scaled spectral flux density, equation (13) is rewritten as

$$\frac{F_\varepsilon(T)}{F_{\varepsilon,0}} = \left(\frac{T}{T_0}\right)^{(2b-m\alpha)/[2(m+1)]} \int_{y_{\min}}^{y_{\max}} dy \left(\frac{m+1}{m+y^{-m-1}}\right)^{1+\alpha} y^{b-1-m\alpha/2} \exp\left[-\tau_{\gamma\gamma}\left(y, \varepsilon_t, \frac{\Delta R}{R_0}, \frac{T}{T_0}, \frac{L_0}{\Gamma_0^{2\alpha} R_0}\right)\right], \quad (94)$$

where $\varepsilon_t = (1+z)\varepsilon$, $y_{\min} = \min[1, R_0/R_L(T)]$, and $y_{\max} = \min[1, (R_0 + \Delta R)/R_L(T)]$, while the flux normalization is given by

$$F_{\varepsilon,0} = 2\Gamma_0 L'_{(1+z)\varepsilon/2\Gamma_0}(R_0) \frac{(1+z)}{4\pi d_L^2} = \frac{2^\alpha L_0 \varepsilon^{1-\alpha} (1+z)^{2-\alpha}}{4\pi d_L^2}, \quad (95)$$

$$\begin{aligned} F_0 &\equiv \varepsilon^{\alpha-1} F_{\varepsilon,0} = (\varepsilon F_{\varepsilon,0})|_{\varepsilon=1} = \frac{L_0}{\pi d_L^2} \left(\frac{1+z}{2}\right)^{2-\alpha} \\ &= 7.6 \times 10^{-6} \left(\frac{1+z}{2}\right)^{2-\alpha} L_{0,52} d_{L,28}^{-2} \text{ erg cm}^{-2} \text{ s}^{-1}, \end{aligned} \quad (96)$$

where $d_L = 10^{28} d_{L,28}$ cm, and may be used in order to infer the value of L_0 from the observed flux level. The optical depth in the integrand above is

$$\tau_{\gamma\gamma}(\varepsilon_t, \theta_{t,0}, R_{t,0}) = \tau_* \varepsilon_t^{\alpha-1} \hat{R}_0^{1-b-m\alpha/2} \mathcal{F}(x), \quad (97)$$

where $\hat{R}_0 = y^{-1}(T/T_0)^{-1/(m+1)}$ and $x = (y^{-(m+1)} - 1)/(m+1)$. The function \mathcal{F} is the following double integral,

$$\mathcal{F}(x) = \int_1^{\hat{R}_2} d\hat{R}_t \int_{\hat{R}_0/\hat{R}_t}^{\hat{R}_{e,2}} d\tilde{R}_e \mathcal{I}(\hat{R}_t, \tilde{R}_e) + \int_{\hat{R}_2}^\infty d\hat{R}_t \int_{\hat{R}_0/\hat{R}_t}^{\hat{R}_{e,3}} d\tilde{R}_e \mathcal{I}(\hat{R}_t, \tilde{R}_e). \quad (98)$$

The two integrals above correspond to cases 1 and 3, respectively, as discussed in § 4.3. When $x > 1$, the test photon lags behind the shell and $f_m(\hat{R}_t) > 1$, with $f_m(\hat{R}_t) \equiv [1 + x(m+1)(1 - \hat{R}_t^{-1})]/\hat{R}_t^{m+1}$; \hat{R}_2 is then defined by the implicit equation $f_m(\hat{R}_2) \equiv 1$, and $\hat{R}_{e,2} \equiv \min[(\hat{R}_0 + \Delta\hat{R})/\hat{R}_t, 1]$. For $m = 0$, $\hat{R}_2 = \max(1, x)$, while for $m = 1$, $\hat{R}_2 = \max(1, [(1+8x)^{1/2} - 1]/2)$. The test photon eventually overtakes the shell at radius R_2 and will travel ahead of the shell ever after, which corresponds to the second integral, where $\hat{R}_{e,3} \equiv \min[(\hat{R}_0 + \Delta\hat{R})/\hat{R}_t, f_m(\hat{R}_t)^{1/(m+1)}]$. When $x \leq 1$, only the second integral contributes, as the photon is emitted on the shell and

immediately travels ahead of it. Thus, $\hat{R}_2 = 1$ so that the first integral vanishes. Note that, for all practical purposes, equation (98) can be cast into a single integral,

$$\mathcal{F}(x) = \int_1^\infty d\hat{R}_t \int_{\hat{R}_0/\hat{R}_t}^{\hat{R}_{e,M}} d\tilde{R}_e \mathcal{I}(\hat{R}_t, \tilde{R}_e), \tag{99}$$

where $\tilde{R}_{e,M} = \tilde{R}_{e,2}$ when $x > 1$ and $f_m(\hat{R}_t) > 1$, and $\tilde{R}_{e,M} = \tilde{R}_{e,3}$ in all other cases, i.e., $\tilde{R}_{e,M} = \min[(\hat{R}_0 + \Delta\hat{R})/\hat{R}_t, f_m(\hat{R}_t)^{1/(m+1)}, 1]$. Finally, the integrand is equal to

$$\mathcal{I}(\hat{R}_t, \tilde{R}_e) = \frac{1}{\hat{R}_t^2} \left(\frac{\delta^3 d\bar{\mu}_e}{\tilde{r}^2 d\tilde{R}_e} \right) \int_{\zeta_-}^{\zeta_+} \frac{\zeta d\zeta}{\sqrt{(\zeta_+ - \zeta)(\zeta - \zeta_-)}} \int_1^\infty \frac{d\chi}{\chi} \frac{\sigma^*(\chi)}{\sigma_T} L'_{\chi^{2/\varepsilon_i \zeta \delta}}(\tilde{R}_e). \tag{100}$$

Specializing to $L'_{\varepsilon'_i}(R) = L' \varepsilon_i^{1-\alpha} (\tilde{R}_e \hat{R}_t / \hat{R}_0)^b$, equation (99) becomes

$$\mathcal{F}(x) = \int_1^\infty d\hat{R}_t \hat{R}_t^{b-2+m\alpha/2} \int_{\hat{R}_0/\hat{R}_t}^{\tilde{R}_{e,M}} d\tilde{R}_e \frac{\delta^{2+\alpha}}{\tilde{r}^2} \frac{d\bar{\mu}_e}{d\tilde{R}_e} \tilde{R}_e^b \bar{\zeta}_-^\alpha H_\alpha(\zeta), \tag{101}$$

where the integrands are further expressed as

$$\begin{aligned} \frac{\delta^{2+\alpha}}{\tilde{r}^2} \frac{d\bar{\mu}_e}{d\tilde{R}_e} \tilde{R}_e^b &\approx \frac{[2(m+1)]^{1+\alpha} \tilde{R}_e^{b+\alpha+m(\alpha+2)/2} (1-\tilde{R}_e)^\alpha}{[(m+1)\tilde{R}_e^{m+1}(1-\tilde{R}_e) + f_m(\hat{R}_t) - \tilde{R}_e^{m+1}]^{1+\alpha}}, \\ \bar{\zeta}_- &= \frac{(\Gamma_t \theta_r - \Gamma_t \theta_t)^2}{4}, \quad \zeta = \frac{4(\Gamma_t \theta_r)(\Gamma_t \theta_t)}{(\Gamma_t \theta_r - \Gamma_t \theta_t)^2}, \quad H_\alpha(\zeta) = {}_2F_1(-\alpha, 0.5; 1; -\zeta), \end{aligned} \tag{102}$$

$$(\Gamma_t \theta_r)^2 = \frac{\tilde{R}_e [f_m(\hat{R}_t) - \tilde{R}_e^{m+1}]}{(m+1)(1-\tilde{R}_e)}, \quad (\Gamma_t \theta_t)^2 = \frac{x}{\hat{R}_t^{m+2}}. \tag{103}$$

This concludes the set of general equations that have been obtained. For reference, the hypergeometric expressions for $\alpha = 1, 2,$ and $3,$ respectively, read

$$\bar{\zeta}_-^1 H_1(\zeta) = \bar{\zeta}_- \left(1 + \frac{\zeta}{2} \right) = \frac{1}{4} [(\Gamma_t \theta_r)^2 + (\Gamma_t \theta_t)^2], \tag{104}$$

$$\bar{\zeta}_-^2 H_2(\zeta) = \bar{\zeta}_-^2 \left(1 + \zeta + \frac{3}{8} \zeta^2 \right) = \frac{(\Gamma_t \theta_t)^4 + (\Gamma_t \theta_r)^4}{16} + \frac{(\Gamma_t \theta_t)^2 (\Gamma_t \theta_r)^2}{4}, \tag{105}$$

$$\bar{\zeta}_-^3 H_3(\zeta) = \bar{\zeta}_-^3 \left(1 + \frac{3}{2} \zeta + \frac{9}{8} \zeta^2 + \frac{5}{16} \zeta^3 \right) = \frac{1}{64} [(\Gamma_t \theta_r)^6 + 9(\Gamma_t \theta_r)^4 (\Gamma_t \theta_t)^2 + 9(\Gamma_t \theta_r)^2 (\Gamma_t \theta_t)^4 + (\Gamma_t \theta_t)^6]. \tag{106}$$

For our fiducial case, $\alpha = 2,$ we also explicitly write the relevant expressions,

$$\tau_0(\varepsilon_t, R_{t,0}) = \tau_* \varepsilon_t \hat{R}_0^{-m-b+1}, \quad \tau_* = 0.402 \left(\frac{\Gamma_0}{100} \right)^{-4} \frac{L_{0,52}}{R_{0,13}}, \tag{107}$$

$$\mathcal{F}(x) = \int_1^\infty \hat{R}_t^{b+m-2} d\hat{R}_t \int d\tilde{R}_e \frac{\delta^4}{\tilde{r}^2} \frac{d\bar{\mu}_e}{d\tilde{R}_e} \tilde{R}_e^b \bar{\zeta}_-^2 H_2(\zeta), \tag{108}$$

$$\frac{\delta^4}{\tilde{r}^2} \frac{d\bar{\mu}_e}{d\tilde{R}_e} = \frac{[2(m+1)]^3 \tilde{R}_e^{2+2m} (1-\tilde{R}_e)^2}{[(m+1)\tilde{R}_e^{m+1}(1-\tilde{R}_e) + f_m(\hat{R}_t) - \tilde{R}_e^{m+1}]^3}, \tag{109}$$

$$\bar{\zeta}_-^2 H_2(\zeta) = \frac{x^2}{16 \hat{R}_t^{2(m+2)}} + \frac{x}{4 \hat{R}_t^{m+2}} \frac{\tilde{R}_e [f_m(\hat{R}_t) - \tilde{R}_e^{m+1}]}{(m+1)(1-\tilde{R}_e)} + \frac{1}{16} \frac{\tilde{R}_e^2 [f_m(\hat{R}_t) - \tilde{R}_e^{m+1}]^2}{(m+1)^2 (1-\tilde{R}_e)^2}. \tag{110}$$

5. ANALYTIC SCALINGS OF THE FLUX AND OPTICAL DEPTH

Before showing our results for the light curves and spectra, it is useful to first analytically derive some of the relevant scaling laws (from the equations obtained in the preceding sections) and discuss the qualitative behavior of the system in different regimes. It is convenient to define a normalized time $\bar{T} \equiv (T/T_0) - 1,$ which is zero when the first photon from $R_{t,0} = R_0$ and $\theta_{t,0} = 0$ reaches the observer and is ~ 1 about a dynamical time later, when the system starts to approach a quasi-steady state. It is also useful to define the

time $T_f = T_0(1 + \Delta R/R_0)^{m+1}$, where $R_L(T_f) \equiv R_0 + \Delta R$, when the lack of emission from outside the outer edge of the emitting region ($R > R_0 + \Delta R$) starts being noticed by the observer, and the corresponding normalized time

$$\bar{T}_f = \frac{T_f}{T_0} - 1 = \left(1 + \frac{\Delta R}{R_0}\right)^{m+1} - 1 \approx \begin{cases} (m+1)\Delta R/R_0 \ll 1, & \Delta R \ll R_0, \\ (\Delta R/R_0)^{m+1} \gg 1, & \Delta R \gg R_0. \end{cases} \quad (111)$$

Note that at $T \leq T_f$ the outer boundary of the emission region does not affect either the emission, since the outer edge of the EATS-I is still fully within the emission region, or the opacity of the emitted photons, since the maximal radius of the EATS-II ($R_{e,\max}$) at all points along the trajectory of any photon is always smaller than that of the EATS-I [$R_L(T)$], $R_{e,\max}(T, y, R_t) < R_L(T)$. As shown in Figure 1, the two radii become nearly equal for $R_t \gg R_L(T)$. In fact, for $R_t \gg R_L(T)$, not only does $R_{e,\max}(T, y, R_t)$ approach $R_L(T)$, but the EATS-II approaches the EATS-I (the two must become identical when the test photon reaches the observer, which corresponds to $R_t \rightarrow \infty$ for a distant observer, at “infinity”). This immediately implies that for $T \leq T_f$ the observed flux and the opacity along the trajectory of all photons (which reach the observer at time T) are independent of ΔR . Thus, in order to calculate the light curves for a family of model parameters that differ only in their ΔR values, it is sufficient to calculate the observed flux and opacity for $\Delta R \rightarrow \infty$ and use them for $T \leq T_f$, and one needs to do the full calculation for each specific value of ΔR only for $T > T_f$.

The temporal scaling of the unattenuated flux, at sufficiently low photon energies ε , can be understood as follows. For $1 \gg \bar{T} < \bar{T}_f$, $y_{\min} = R_0/R_L(T) = (T/T_0)^{-1/(m+1)} = (1 + \bar{T})^{-1/(m+1)}$ and $y_{\max} = 1$, so that $\Delta y = y_{\max} - y_{\min} \approx \bar{T}/(m+1)$ while $y \approx 1$ and the integrand in equation (13) is also ≈ 1 , implying that $F_\varepsilon \propto \bar{T}$. For $\bar{T}_f < \bar{T} \ll 1$ the emission is from $R \approx R_0$ from angles θ which satisfy $(\Gamma_0\theta)^2 \approx \bar{T}/(m+1) \ll 1$, while the Doppler factor at this stage is almost constant, $\delta \approx 2\Gamma_0/[1 + (\Gamma_0\theta)^2] \approx 2\Gamma_0/[1 + \bar{T}/(m+1)] \approx 2\Gamma_0$, and therefore, the flux is approximately constant in time, $F_\varepsilon \propto \delta^{-1-\alpha} \propto \bar{T}^0$. For $\bar{T}_f \ll 1 \ll T$, $\delta \approx 2\Gamma_0/(\Gamma_0\theta)^2 \propto \bar{T}^{-1}$ and $F_\varepsilon \propto \bar{T}^{-1-\alpha}$. For $1 \ll \bar{T} < \bar{T}_f$, $y_{\min} = R_0/R_L(T) = (1 + \bar{T})^{-1/(m+1)} \approx \bar{T}^{-1/(m+1)} \ll 1$ and $y_{\max} = 1$, so that the integral over y in equation (13) approaches a constant (corresponding to its value for $\int_0^1 dy$) and $F_\varepsilon \propto \bar{T}^{(2b-m\alpha)/[2(m+1)]}$. Finally, for $\bar{T} \gg \bar{T}_f$ the emission is dominated by $R \sim R_0 + \Delta R$ and angles $\theta_{t,0} \gg 1/\Gamma_{t,0}$ (i.e., $x \gg 1$), and we obtain the familiar result for “high-latitude” emission (Kumar & Panaitescu 2000), $F_\varepsilon \propto \bar{T}^{-1-\alpha}$. Altogether,

$$F_{\varepsilon < \varepsilon_1(\bar{T})} \propto \begin{cases} \bar{T}, & 1 \gg \bar{T} < \bar{T}_f, \\ \bar{T}^0, & \bar{T}_f < \bar{T} \ll 1, \\ \bar{T}^{(2b-m\alpha)/[2(m+1)]}, & 1 \ll \bar{T} < \bar{T}_f, \\ \bar{T}^{-1-\alpha}, & \bar{T} \gg \max(1, \bar{T}_f). \end{cases} \quad (112)$$

Now we move on to discuss the opacity effects in some detail. As can be seen in Figure 5, at a given emission radius the optical depth is smallest for small emission angles (i.e., small values of x). There is a local maximum near $x = \gamma_{t,0}\theta_{t,0} \approx 1$, since for such emission angles the photon is emitted almost parallel to the shell in the comoving frame, and a relatively large part of its trajectory (also in the lab frame) is close to the emitting shell, which enhances the optical depth. For a given normalized emission angle, $x^{1/2} = \gamma_{t,0}\theta_{t,0}$, the normalized optical depth increases with emission radius, as can be seen in Figure 6, where the increase is largest for small emission angles. The optical depth generally increases with $\Delta R/R_0$ when all other model parameters are held fixed, due to the larger range of emission radii which enhances the photon field that can potentially interact with test photons. However, as pointed out above, for $T \leq T_f$ the optical depth in this case is independent of $\Delta R/R_0$. This is demonstrated in the right panel of Figure 6, where it can be seen that in practice a noticeable increase in the optical depth due to the increase in $\Delta R/R_0$ does not occur immediately after T_f but takes some time to come into effect. This is because for $0 < T - T_f \ll T_f$ the added contribution to the opacity from $R > R_0 + \Delta R$ for the smaller ΔR is very small, since the additional photons can interact with the test photon only at very large radii [$R_t \gg R_L(T_f) = R_0 + \Delta R$] where the density of the photon field is very small, and at very small angles between the directions of the photons which are very unfavorable for interaction.

One would also like to define ε_1 as the photon energy at which the optical depth becomes unity, $\tau_{\gamma\gamma}(\varepsilon_1) \equiv 1$. However, this definition gives a different value along the trajectories of different (test) photons, making it hard to define a unique value for $\varepsilon_1(\bar{T})$, since its value varies along the EATS-I (see Figs. 7 and 8). For $1 \ll \bar{T} < \bar{T}_f$, $\mathcal{F}(x)$ becomes independent of \bar{T} and depends only on x (see the left panel of Fig. 7 and Fig. 8). Most of the contributions to the observed flux come from $x \lesssim 1$, since for $x \gg 1$ the radiation is strongly beamed away from the observer. The left panel of Figure 7 shows that $\mathcal{F}(x \lesssim 1)$ varies over a factor of ~ 50 for $1 \ll \bar{T} < \bar{T}_f$, and therefore, in this regime it still makes some sense to define a single typical value of $\varepsilon_1(\bar{T})$ and derive its scaling. It is good to keep in mind, however, both the spectral transitions around $\varepsilon_1(\bar{T})$ in the instantaneous spectrum and around $\varepsilon_1(\bar{T}_f)$ in the time-integrated spectrum, as well as the transition in the light curve when $\varepsilon_1(\bar{T})$ sweeps past the observed photon energy ε , are all expected to be somewhat smoothed due to this relatively large range of opacity values across the (unresolved) observed image of the GRB projected in the sky. According to equation (40), $\tau_{\gamma\gamma} \propto \tau_0 \propto \varepsilon_f^{\alpha-1} \hat{R}_0^{1-b-m\alpha/2} \propto \varepsilon_f^{\alpha-1} \bar{T}^{-(1-b-m\alpha/2)/(m+1)}$, and therefore, $\varepsilon_1(1 \ll \bar{T} < \bar{T}_f) \propto \bar{T}^{(1-b-m\alpha/2)/[(m+1)(\alpha-1)]}$.

The right panel of Figure 7 shows $\mathcal{F}(x)$ as a function of $Y \equiv (y - y_{\min})/(y_{\max} - y_{\min}) \approx (x_{\max} - x)/x_{\max}$ for several values of $1 \gg \bar{T} < \bar{T}_f$, along the equal arrival time surface of photons to the observer (EATS-I; see also Fig. 8). In this limit, $R_{t,0} \approx R_0$, $y \approx 1 - x$, and $x_{\max} \approx \bar{T}/(m+1) \approx [\Gamma_0 R_{\perp, \max}(\bar{T})/R_0]^2$, where $R_{\perp, \max}(\bar{T})$ is the radius of the GRB observed image, projected in the sky, at a normalized observed time \bar{T} . As is shown analytically in Appendix D and is apparent in the right panel of Figure 7, in this limit

$$\mathcal{F}(x = 0, 1 \gg \bar{T} < \bar{T}_f) \propto \bar{T}. \quad (113)$$

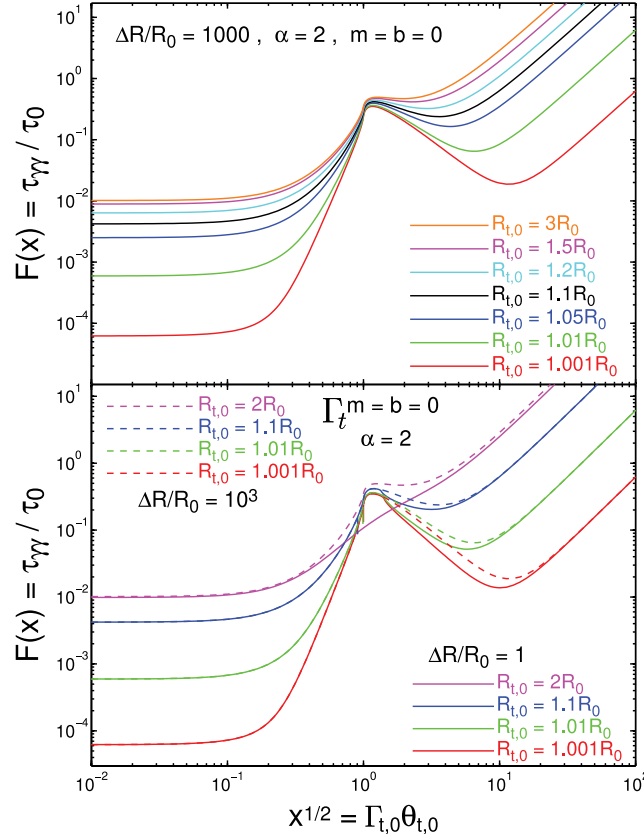


FIG. 5.—Normalized optical depth $\mathcal{F}(x) = \tau_{\gamma}/\tau_0$ as a function of the renormalized emission angle, $x^{1/2} = \Gamma_{t,0}\theta_{t,0}$, for several different emission radii $R_{t,0}$. The top panel is for $\Delta R/R_0 = 1000$, while the bottom panel shows the results for $\Delta R/R_0 = 1$ (solid lines) and for $\Delta R/R_0 = 1000$ (dashed lines) overlaid on each other. The small vertical lines in the bottom panel indicate the angle that corresponds to $\bar{T} = \bar{T}_f$, outside of which the contributions to the opacity from $R > R_0 + \Delta R$ for $\Delta R/R_0 = 1$ start being missed (this effect becomes significant only at somewhat larger angles; see discussion in the text). For $R_{t,0} = 2R_0 = R_0 + \Delta R$, this corresponds to $x^{1/2} = \gamma_{t,0}\theta_{t,0} = 0$, which is outside the range shown in the figure. In both panels the photon index is $\alpha = 2$, while the Lorentz factor and the total luminosity in the comoving frame are independent of radius ($m = b = 0$).

The right panel of Figure 7 also shows that

$$\mathcal{F}(x, 1 \gg \bar{T} < \bar{T}_f) \approx \mathcal{F}(x = 0, 1 \gg \bar{T} < \bar{T}_f) \begin{cases} Y, & Y > Y_*(\bar{T}), \\ Y_*(\bar{T}), & Y < Y_*(\bar{T}), \end{cases} \quad (114)$$

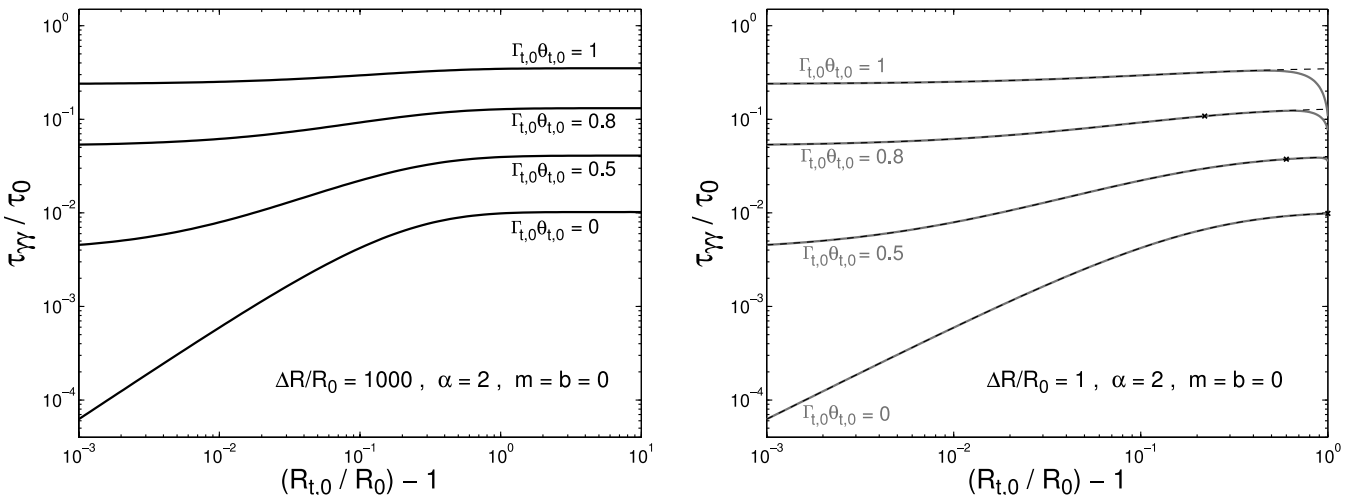


FIG. 6.—Normalized optical depth $\mathcal{F}(x) = \tau_{\gamma}/\tau_0$ as a function of the renormalized emission radius, $(R_{t,0}/R_0) - 1$, for different values of the normalized emission angle $x^{1/2} = \Gamma_{t,0}\theta_{t,0}$. The left panel is for $\Delta R/R_0 = 1000$. The right panel is for $\Delta R/R_0 = 1$, but also shows the corresponding result for $\Delta R/R_0 = 1000$ in dashed lines, where the crosses show the value of the emission radius corresponding to an observed time of $T = T_f$ [for $\Gamma_{t,0}\theta_{t,0} = 1$ this corresponds to $(R_{t,0}/R_0) - 1 = 0$ which is outside the range shown in the figure]. Note the deviation near $(R_{t,0}/R_0) - 1 \sim 1$ and see the text for discussion of its origin. [See the electronic edition of the Journal for a color version of this figure.]

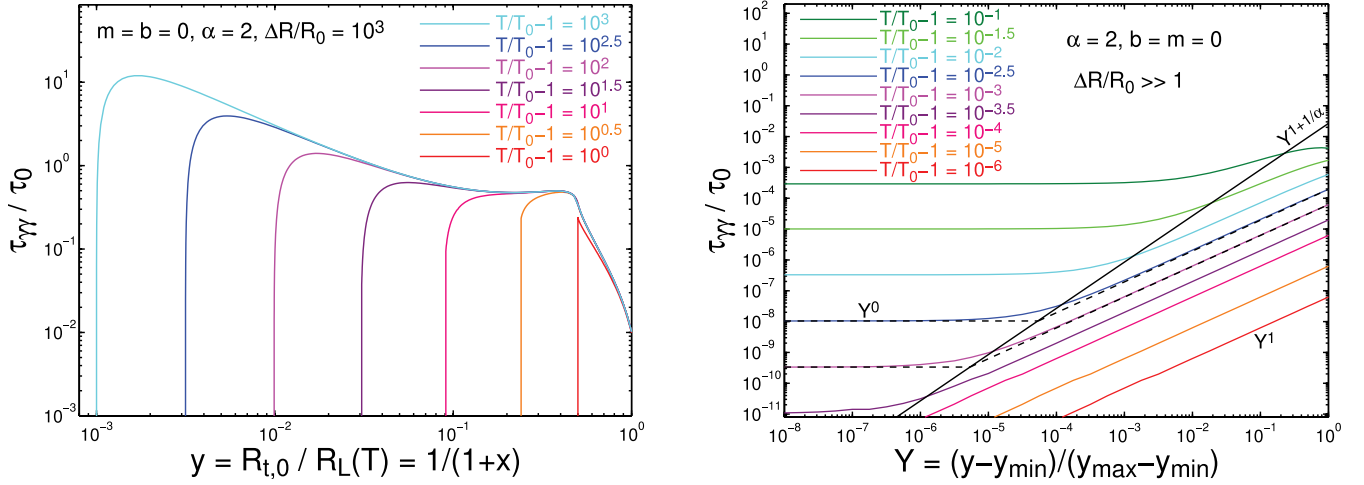


FIG. 7.—Normalized optical depth $\mathcal{F}(x) = \tau_{\gamma}/\tau_0$, along the equal arrival time surface of photons to the observer (EATS-I), for several different values of the normalized time $\bar{T} = (T/T_0) - 1$. The left panel shows $\mathcal{F}(x)$ as a function of the normalized emission radius $y = R_{t,0}/R_L(T)$ for several values of $1 \geq \bar{T} < \bar{T}_f$, while the right panel shows $\mathcal{F}(x)$ as a function of $Y \equiv (y - y_{\min})/(y_{\max} - y_{\min}) \approx (x_{\max} - x)/x_{\max}$ for several values of $1 \gg \bar{T} < \bar{T}_f$.

where $Y_* \approx (x_{\max} - x_*)/x_{\max} \propto \bar{T}^\alpha$ is the value of Y where the scaling of $\mathcal{F}(x)$ changes from $\propto Y^0$ to $\propto Y^1$. The corresponding value of x is x_* , and $\mathcal{F}(x_*) \approx \mathcal{F}(x_{\max}) \propto \bar{T}^{\alpha+1} \propto Y_*^{(\alpha+1)/\alpha}$.

The scaling of $\mathcal{F}(x)$ with Y for $1 \gg \bar{T} < \bar{T}_f$ can be understood as follows. For a given emission radius $R_{t,0}$, the dependence of the optical depth and $\mathcal{F}(x)$ on the emission angle $\theta_{t,0}$ is very weak for $x = (\Gamma_{t,0}\theta_{t,0})^2 \ll 1$ and becomes significant only for $x \gtrsim 1$ (see Fig. 5). Therefore, as x starts increasing from $x = 0$ at the line of sight, along the EATS-I, $\mathcal{F}(x)$ initially varies following its dominant radial dependence. The latter may be derived from that along the line of sight where $\mathcal{F}(x) \propto \bar{T} \propto (R_{t,0}/R_0) - 1$, where for a general value of $x < x_{\max} \ll 1$ we have $(R_{t,0}/R_0) - 1 \approx x_{\max} - x \propto Y$ and therefore $\mathcal{F}(x) \propto Y$. As x approaches x_{\max} , Y approaches zero, until eventually the optical depth becomes dominated by the small angular dependence on $\theta_{t,0}$ at a fixed emission radius $R_{t,0}$, and $\mathcal{F}(x)$ approaches a constant value of $\mathcal{F}(x_{\max})$ which corresponds to $R_{t,0} = R_0$ and $x = (\Gamma_0\theta_{t,0})^2 = x_{\max} = \bar{T}/(m+1)$. We find that $\mathcal{F}(x_{\max}) \propto \bar{T}^{\alpha+1} \propto x_{\max}^{\alpha+1} = (\Gamma_0\theta_{t,0})^{2(\alpha+1)}$. This may be understood as follows, starting from the expression for the optical depth in equation (32). In this regime $\tilde{R}_{e,\max} = f_m^{1/(m+1)}$, and for $R_{t,0} = R_0$ we have

$$\frac{\tilde{R}_{e,\max}}{R_0} - 1 = [1 + x(m+1)(1 - \hat{R}_t^{-1})]^{1/(m-1)} - 1 \approx x(1 - \hat{R}_t^{-1}) \ll 1. \quad (115)$$

This means that the contribution to the local photon field at each point along the trajectory of the test photon is always from a very narrow range of radii near R_0 . This implies that $r^{-2}|d\mu_r/d\mu_r|$, which appears in equation (32), remains approximately constant, since the geometry of the problem implies $R_0\theta_e \approx r\theta_r$, so that $r^{-2}|d\mu_r/d\mu_r| \approx R_0^{-2} = \text{const}$. At any given point along the test photon trajectory $\theta_r \leq \theta_t \leq \theta_{t,0}$, simply because in this regime $\theta_{r,\max}$ is obtained where EATS-II is truncated at R_0 , which must correspond to $\theta_r = \theta_t$ for a test photons that is emitted at $R_{t,0} = R_0$ (the test photon is always on its own EATS-I and EATS-II, by definition). This implies that

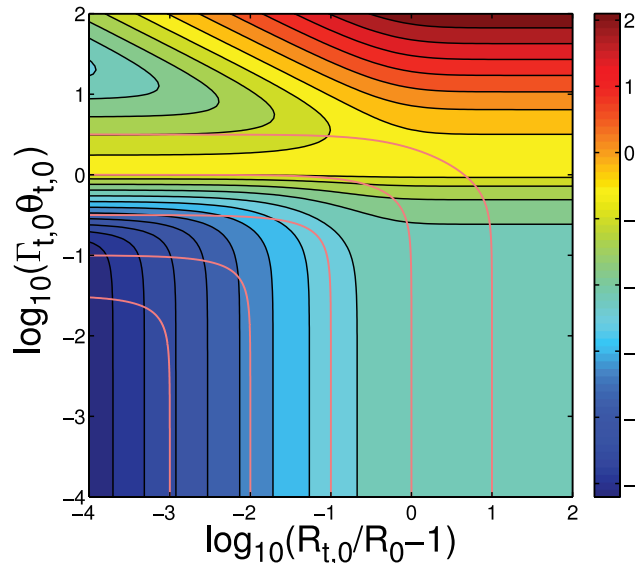


FIG. 8.—Contour plot of $\log_{10}(\tau_{\gamma}/\tau_0)$ as a function of the normalized emission radius, $\log_{10}(R_{t,0}/R_0 - 1)$, and emission angle, $\log_{10}(\Gamma_{t,0}\theta_{t,0})$, for $m = b = 0$, $\alpha = 2$, and a large (effectively infinite) $\Delta R/R_0$. Overlaid are plotted (in thick lines) the equal arrival time surfaces of photons to the distant observer (EATS-I) for $\log_{10}(\bar{T}) = -3, -2, -1, 0, \text{ and } 1$.

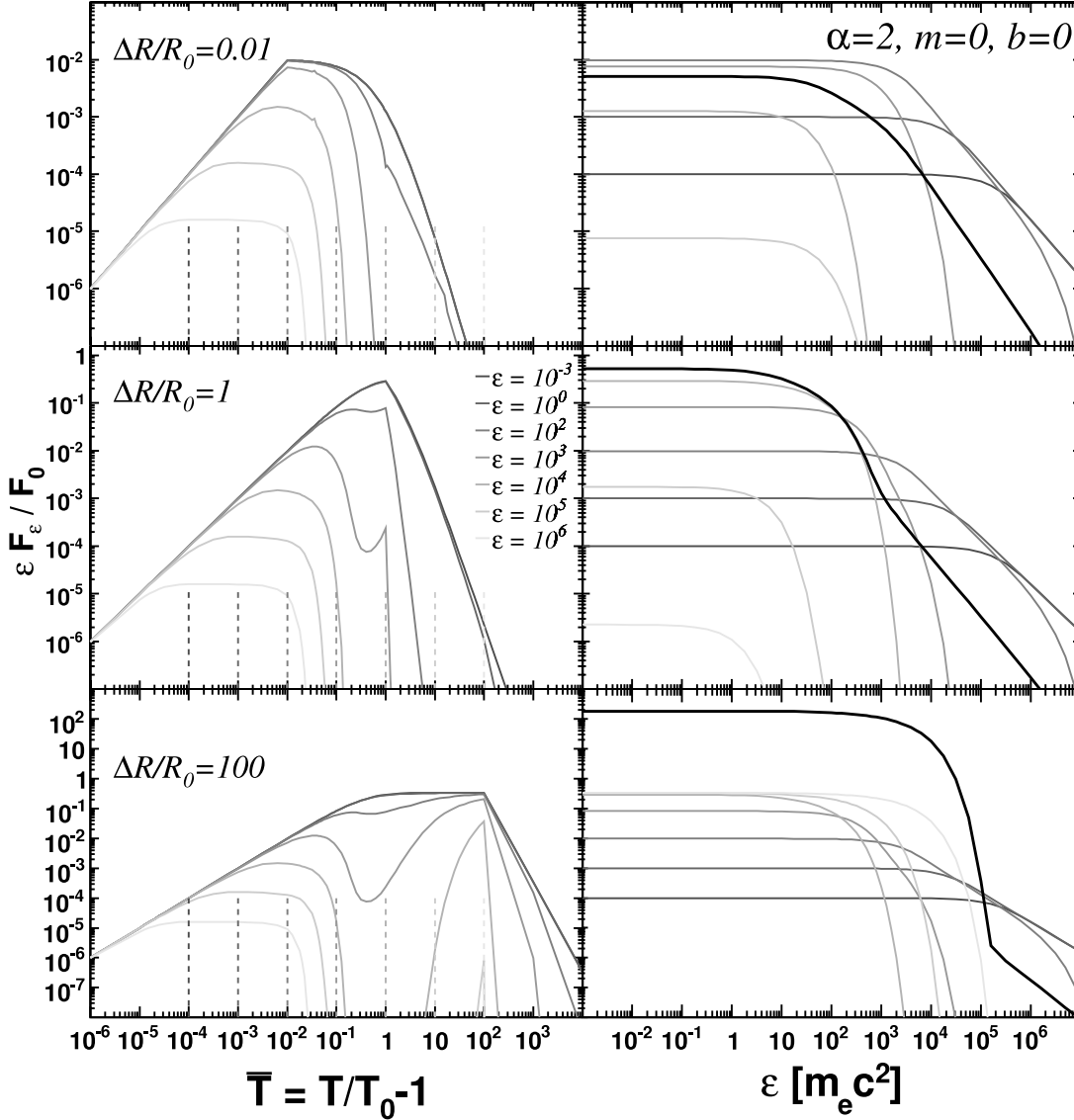


FIG. 9.—Light curves (left) and instantaneous (thin lines) and time-integrated (thick lines) spectra (right), calculated using our semianalytic model, for a constant Lorentz factor ($m = 0$) and a comoving emissivity independent of radius ($b = 0$) with equal energy per decade of photon energy (corresponding to a photon index of $\alpha = 2$). The vertical dashed lines in the left panels indicate the times for which the instantaneous spectra are shown in the corresponding right panel, using matching colors. We show results for three different radial extents of the emission region, $\Delta R/R_0 = 0.01, 1,$ and 100 , from top to bottom. We also use $\tau_* = 1$ (see eq. [37]). [See the electronic edition of the *Journal* for a color version of this figure.]

$\delta \approx 2\Gamma_0 = \text{const}$, since $\Gamma(\theta_e + \theta_r) \leq 2\Gamma_0\theta_t \leq 2\Gamma_0\theta_{t,0} = 2x^{1/2} \ll 1$. Furthermore, $L'_{\varepsilon_i}(\tilde{R}_e)$ is approximately constant, since $\tilde{R}_e \approx R_0 = \text{const}$. Since $\theta_t/\theta_{t,0} \approx R_{t,0}/R_t = \hat{R}_t$, the effective solid angle that contributes to interaction at R_t is $\sim \theta_t^2 \propto R_t^{-2}$, and there is also a factor of $1 - \mu_{ii} \sim \theta_t^2 \propto R_t^{-2}$ in the integrand of equation (32), most of the contribution to the total optical depth is from $R_t \sim R_{t,0}$ (i.e., $\hat{R}_t \lesssim 2$). Therefore, the integration over the solid angle effectively introduces a factor of $\sim \theta_{t,0}^2$, while the factor of $1 - \mu_{ii}$ in the integrand introduces a similar factor, together giving a factor of $\sim \theta_{t,0}^4$. The integration over energy ε_i together with the threshold $\varepsilon_t \varepsilon_i > 2/(1 - \mu_{ii})$ for pair production give $L'_{\varepsilon_i} \propto \varepsilon_i^{1-\alpha} \propto \varepsilon_i^{\alpha-1} (1 - \mu_{ii})^{\alpha-1} \propto \theta_{t,0}^{2(\alpha-1)}$. Altogether, with the previous factor of $\theta_{t,0}^4$, the optical depth in this regime scales as $\theta_{t,0}^{2(\alpha+1)}$.

Thus, for fixed values of τ_* and ε , $\tau_{\gamma\gamma}$ first becomes larger than unity at the center of the image ($x \ll 1$ and $Y \approx 1$) at $\bar{T}_{1i} \sim \alpha 2^{2\alpha-1}/\tau_* \varepsilon^{\alpha-1}$. From this time on, the central part of the image is opaque, at $x < x_1$ which corresponds to $Y_1 \approx \bar{T}_{1i}/\bar{T}$, so that photons of energy ε can escape mainly from a thin ring in the outer part of the image that corresponds to $x_1 < x < x_{\text{max}}$ and occupies a fraction $Y_1 \approx \bar{T}_{1i}/\bar{T} \propto \bar{T}^{-1}$ of the image area (since that area is linear in x). Thus, the observed flux is suppressed by a similar factor and turns from $\propto \bar{T}$ at $\bar{T} < \bar{T}_{1i}$ to $\propto \bar{T}^0$ at $\bar{T} > \bar{T}_{1i}$. Eventually, at a later time $\bar{T}_{1f} \sim \bar{T}_{1i}^{1/(\alpha+1)} \propto \varepsilon^{-(\alpha-1)/(\alpha+1)}$ when $x_1 = x_*$, the whole image becomes opaque, i.e., $\tau_{\gamma\gamma} > 1$ for all $0 \leq x \leq x_{\text{max}}$, and the observed flux starts to drop exponentially with time. This behavior can be seen, e.g., in Figure 9. In summary,

$$F_{\varepsilon \gg \varepsilon_{1*}}(\bar{T} \ll 1) \sim F_{\varepsilon < \varepsilon_{1*}}(\bar{T} = 1) \begin{cases} \bar{T}, & \bar{T} < \bar{T}_{1i}(\varepsilon), \\ \bar{T}_{1i}, & \bar{T}_{1i}(\varepsilon) < \bar{T} < \bar{T}_{1f}(\varepsilon), \\ \bar{T}^{\alpha+1} \exp[-(\bar{T}/\bar{T}_{1f})^{\alpha+1}], & \bar{T} > \bar{T}_{1f}(\varepsilon). \end{cases} \quad (116)$$

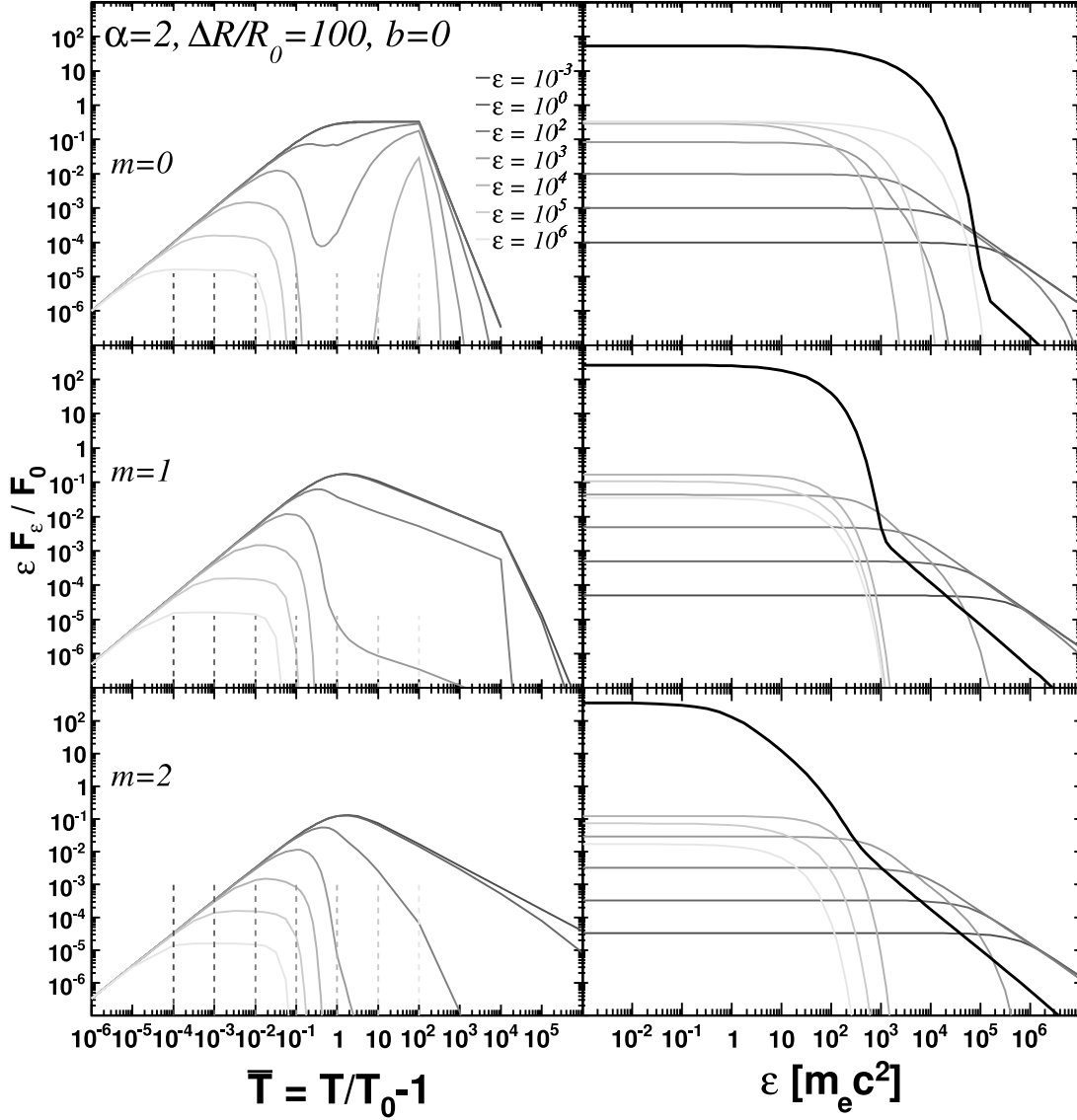


FIG. 10.— Same as Fig. 9, with $b = 0$, $\alpha = 2$, and $\tau_* = 1$, but for a fixed $\Delta R/R_0 = 100$ and varying m where $\Gamma^2 \propto R^{-m}$. [See the electronic edition of the Journal for a color version of this figure.]

Similarly, for $1 \gg \bar{T} < \bar{T}_f$ it is natural to define $\epsilon_{1i}(\bar{T})$ and $\epsilon_{1f}(\bar{T})$ as the two photon energies above which the center and outer edge of the observed image, respectively, become optically thick to pair production; by definition, $\bar{T}_{1i,f}[\epsilon_{1i,f}(\bar{T})] \equiv \bar{T}$. This implies that $\epsilon_{1i} \sim (\alpha 2^{2\alpha-1}/\tau_* \bar{T})^{1/(\alpha-1)} \propto \bar{T}^{-1/(\alpha-1)}$, and since $\bar{T}_{1f} \sim \bar{T}_{1i}^{1/(\alpha+1)}$, we have $\epsilon_{1i}/\epsilon_{1f} \sim \bar{T}^{\alpha/(\alpha-1)}$ and $\epsilon_{1f} \propto \bar{T}^{-(\alpha+1)/(\alpha-1)}$. Equation (116) determines the instantaneous spectrum in this regime,

$$F_\epsilon \gg \epsilon_{1*}(\bar{T} \ll 1) \sim \bar{T} F_{\epsilon=1 < \epsilon_{1*}}(\bar{T} = 1) \begin{cases} \epsilon^{-(\alpha-1)}, & \epsilon < \epsilon_{1i}(\bar{T}), \\ \epsilon_{1i}^{\alpha-1} \epsilon^{-2(\alpha-1)}, & \epsilon_{1i}(\bar{T}) < \epsilon < \epsilon_{1f}(\bar{T}), \\ \epsilon_{1i}^{\alpha-1} \epsilon_{1f}^{-2(\alpha-1)} \exp[-(\epsilon/\epsilon_{1f})^{\alpha-1}], & \epsilon > \epsilon_{1f}(\bar{T}). \end{cases} \quad (117)$$

At $\bar{T} \sim 1$ the opacity becomes more uniform across the image, $\bar{T}_{1i} \sim \bar{T}_{1f} \sim 1$, and $\epsilon_{1i} \sim \epsilon_{1f} \sim \epsilon_1(\bar{T} = 1) \sim \epsilon_{1*}$.

For $\epsilon \gg \epsilon_1(\bar{T} = 1)$, the time-integrated flux $f_\epsilon = \int dT F_\epsilon(T)$ is approximately given by $\sim T_0 F_{\epsilon < \epsilon_1}(\bar{T} = 1) \bar{T}_{1i} \bar{T}_{1f}$, where $\bar{T}_{1i} \bar{T}_{1f} \propto \bar{T}_{1i}^{(\alpha+2)/(\alpha+1)} \propto \epsilon^{-(\alpha-1)(\alpha+2)/(\alpha+1)}$, since $\bar{T}_{1i} \propto \epsilon^{1-\alpha}$. Therefore, the spectral slope of the time-integrated spectrum, f_ϵ , for impulsive sources ($\Delta R \lesssim R_0$ and $\bar{T}_f \lesssim 1$) where the total time-integrated flux is comparable to that from the rising phase, steepens by $\Delta\alpha = (\alpha - 1)(\alpha + 2)/(\alpha + 1)$ above $\epsilon_1(\bar{T}_f)$,

$$f_\epsilon(\Delta R \sim R_0) \propto \begin{cases} \epsilon^{-(\alpha-1)}, & \epsilon \ll \epsilon_1(\bar{T}_f), \\ \epsilon^{-(\alpha-1)(2\alpha+3)/(\alpha+1)}, & \epsilon \gg \epsilon_1(\bar{T}_f). \end{cases} \quad (118)$$

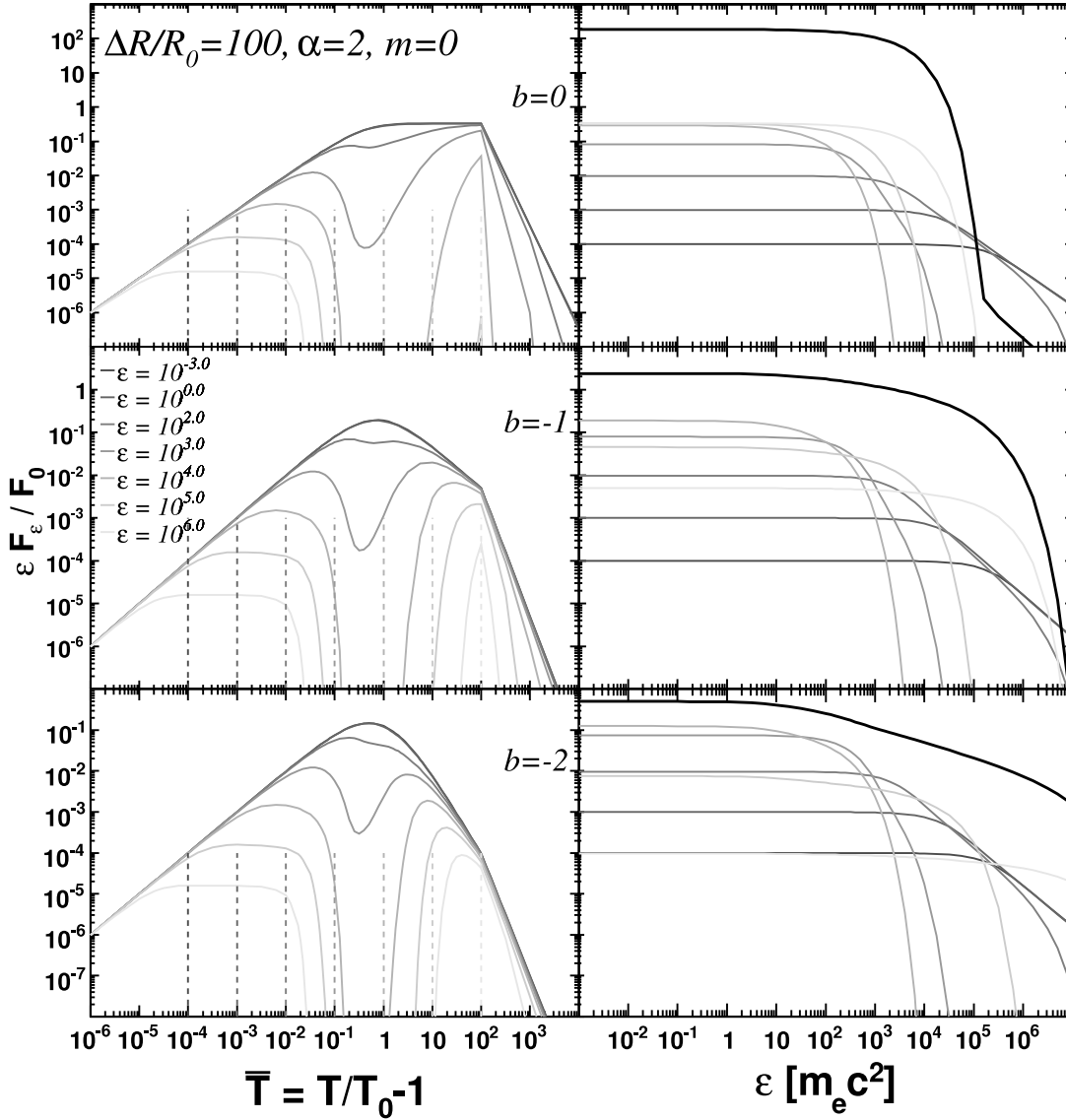


FIG. 11.— Same as Fig. 9, with $m = 0$, $\alpha = 2$, and $\tau_* = 1$, but for a fixed $\Delta R/R_0 = 100$ and varying b where the spectral luminosity in the comoving frame of the shell scales as $L'_\varepsilon \propto R^b (\varepsilon')^{1-\alpha}$. [See the electronic edition of the Journal for a color version of this figure.]

This can be seen in Figure 13. For a quasi-steady source ($\Delta R \gg R_0$ and $\bar{T}_f \gg 1$), a similar time-integrated spectrum is obtained only if the flux at $1 < \bar{T} < \bar{T}_f$ decays faster than \bar{T}^{-1} , i.e., if $m(\alpha - 2) > 2(b + 1)$ (see eq. [112]), so that f_ε is dominated by contributions near $\bar{T} \sim 1$. For a slower decay or a rising flux at $1 < \bar{T} < \bar{T}_f$, f_ε is dominated by contributions from $\bar{T} \sim \bar{T}_f$ and there is an exponential cutoff above $\varepsilon_1(\bar{T}_f)$, while the power-law high-energy tail from the rising phase is encountered only after a significant (exponential in ε) flux drop. For extremely impulsive sources, where $\bar{T}_f \ll 1$ (i.e., $\Delta R \ll R_0$), there is also an intermediate power-law segment in the time-integrated spectrum,

$$f_\varepsilon(\Delta R \ll R_0) \propto \begin{cases} \varepsilon^{-(\alpha-1)}, & \varepsilon < \varepsilon_{1i}(\bar{T}_f), \\ \varepsilon^{-2(\alpha-1)}, & \varepsilon_{1i}(\bar{T}_f) < \varepsilon < \varepsilon_{1f}(\bar{T}_f), \\ \varepsilon^{-(\alpha-1)(2\alpha+3)/(\alpha+1)}, & \varepsilon > \varepsilon_{1f}(\bar{T}_f). \end{cases} \quad (119)$$

6. RESULTS: SEMIANALYTIC LIGHT CURVES AND SPECTRA

Figures 9–12 show light curves and spectra for the semianalytic model developed in the preceding sections. We use fiducial parameter values of $m = b = 0$, $\Delta R/R_0 = \tau_* = 1$, and $\alpha = 2$, which are relevant for the prompt gamma-ray emission in GRBs, and vary one parameter at a time in order to see the effect of each model parameter more clearly. When varying m and b (Figs. 10 and 11, respectively) we use $\Delta R/R_0 = 100$ in order to have a large enough range of emission radii so that the radial dependence of the Lorentz factor and of the comoving spectral emissivity would have a significant effect on the light curves (for $\Delta R/R_0 \ll 1$ the values of m and b hardly affect the light curves). Figure 13 shows the time-integrated spectra for several values of $\Delta R/R_0$, where each panel is for a

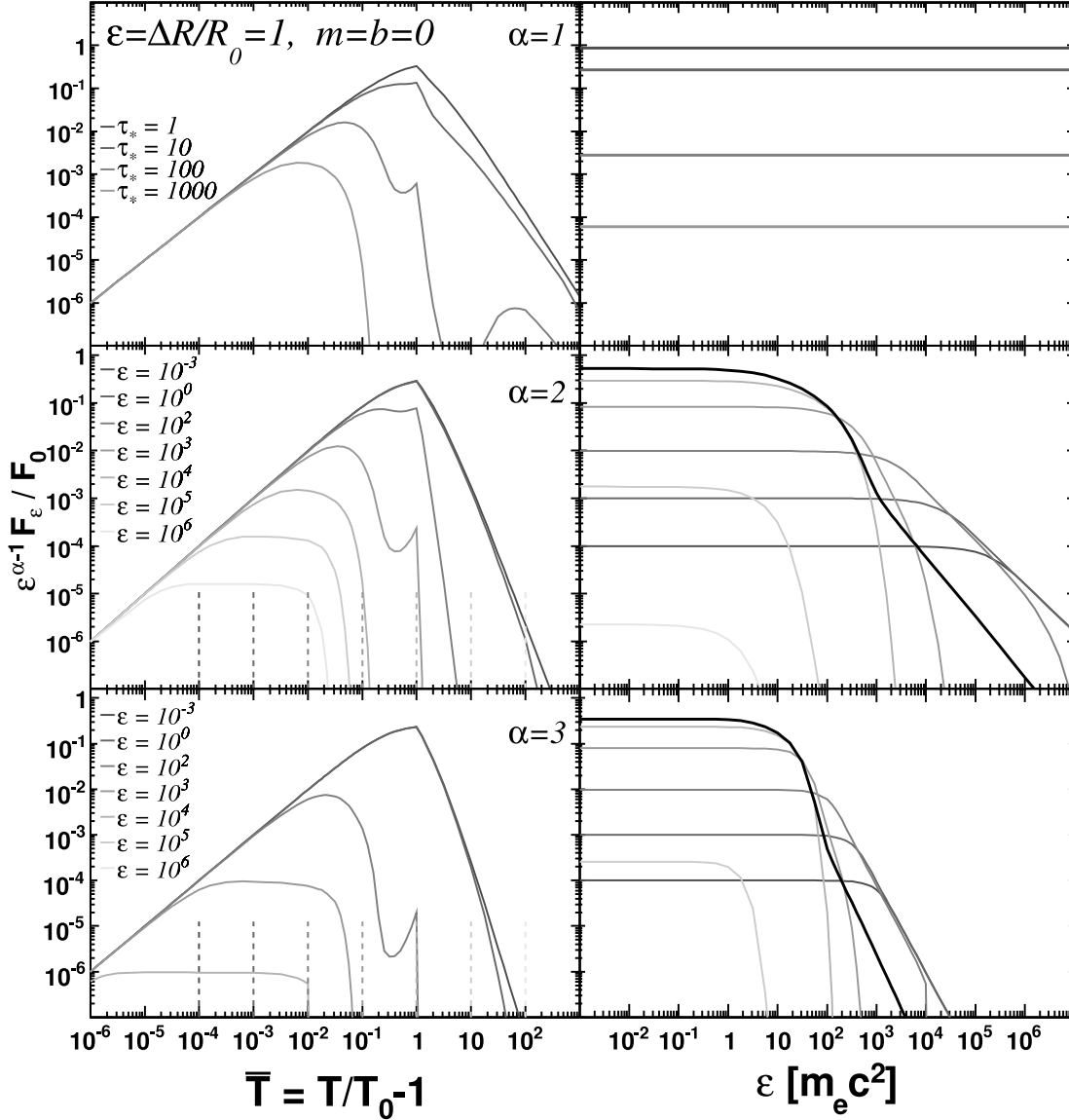


FIG. 12.— Same as Fig. 9, with $b = m = 0$ and $\tau_* = 1$, but for $\Delta R/R_0 = 1$ and varying α , where the spectral luminosity in the comoving frame of the shell scales as $L'_\epsilon \propto R^b (\epsilon')^{1-\alpha}$. The middle and bottom panels are for $\alpha = 2$ and 3 , respectively. The top panel is for $\alpha = 1$, for which $\tau_{\gamma\gamma}$ becomes independent of the photon energy ϵ , and therefore, the spectrum is always a pure power law, $F_\epsilon \propto \epsilon^\beta$, and the flux depends only on time but not on the photon energy. For this reason we show light curve (left) and time-integrated spectra (right panel) for different values of τ_* (see eq. [37]). [See the electronic edition of the Journal for a color version of this figure.]

different set of values for the three parameters (α, m, b) . In order to ease the reading, Table 2 summarizes the various sets of parameters and the corresponding figures.

Figure 9 shows the light curves for fixed values $m = b = 0$, $\tau_* = 1$, and $\alpha = 2$, while the various panels correspond to different values of $\Delta R/R_0$ (of 0.01, 1, and 100, from top to bottom). At the lowest photon energies, well below ϵ_{1*} (which for the parameter values used here is $\sim 10^2$), opacity to pair production never becomes very significant, and the light curves follow the behavior described in equation (112) which is discussed in § 5. In this regime the light curves are self-similar in the sense that $\epsilon^{\alpha-1} F_\epsilon$ is independent of ϵ below $\epsilon_1(T)$. The different behavior for $\bar{T}_f \ll 1$ and $\bar{T}_f \gg 1$ (where $\bar{T}_f = \Delta R/R_0$ for $m = 0$) that appears in equation (112) can clearly be seen by comparing the top and bottom panels of Figure 9. For $\epsilon \gg \epsilon_{1*}$, on the other hand, opacity to pair production has a major effect on the light curves. In this regime, the light curves at $\bar{T} \ll 1$ follow equation (116), showing a pronounced constant-flux plateau between $\bar{T}_{li} \propto \epsilon^{1-\alpha}$, when the center of the image becomes optically thick to pair production, and $\bar{T}_{lf} \sim \bar{T}_{li}^{1/(\alpha+1)}$, when the entire image becomes opaque, followed by an exponential flux decay. At $1 \lesssim \bar{T} < \bar{T}_f$ the opacity does not vary drastically across the image and may be described by a single value of $\epsilon_1(1 \ll \bar{T} < \bar{T}_f) \propto \bar{T}^{(1-b-m\alpha/2)/[(m+1)(\alpha-1)]}$. For the parameter values used in Figure 9, ϵ_1 increases (linearly) with \bar{T} in this range, and therefore, the opacity at a given ϵ decreases with time, causing the observed flux to increase with time until ϵ_1 sweeps across ϵ or until \bar{T}_f is reached (whichever comes first). At $\bar{T} > \bar{T}_f$ the situation is reversed, as the observed emission comes from large angles relative to the line of sight (“high-latitude” emission) and ϵ_1 decreases with time.

We now turn to the photon energy spectrum. The instantaneous spectra at $\bar{T} \ll 1$ follow the behavior described in equation (117). At very early times the exponential part starts only at very high photon energies, making it very hard to detect. When $\bar{T} \sim 1$ the intermediate power-law segment disappears as ϵ_{li} and ϵ_{lf} become nearly equal (note that the low-energy part of the curves appears flat

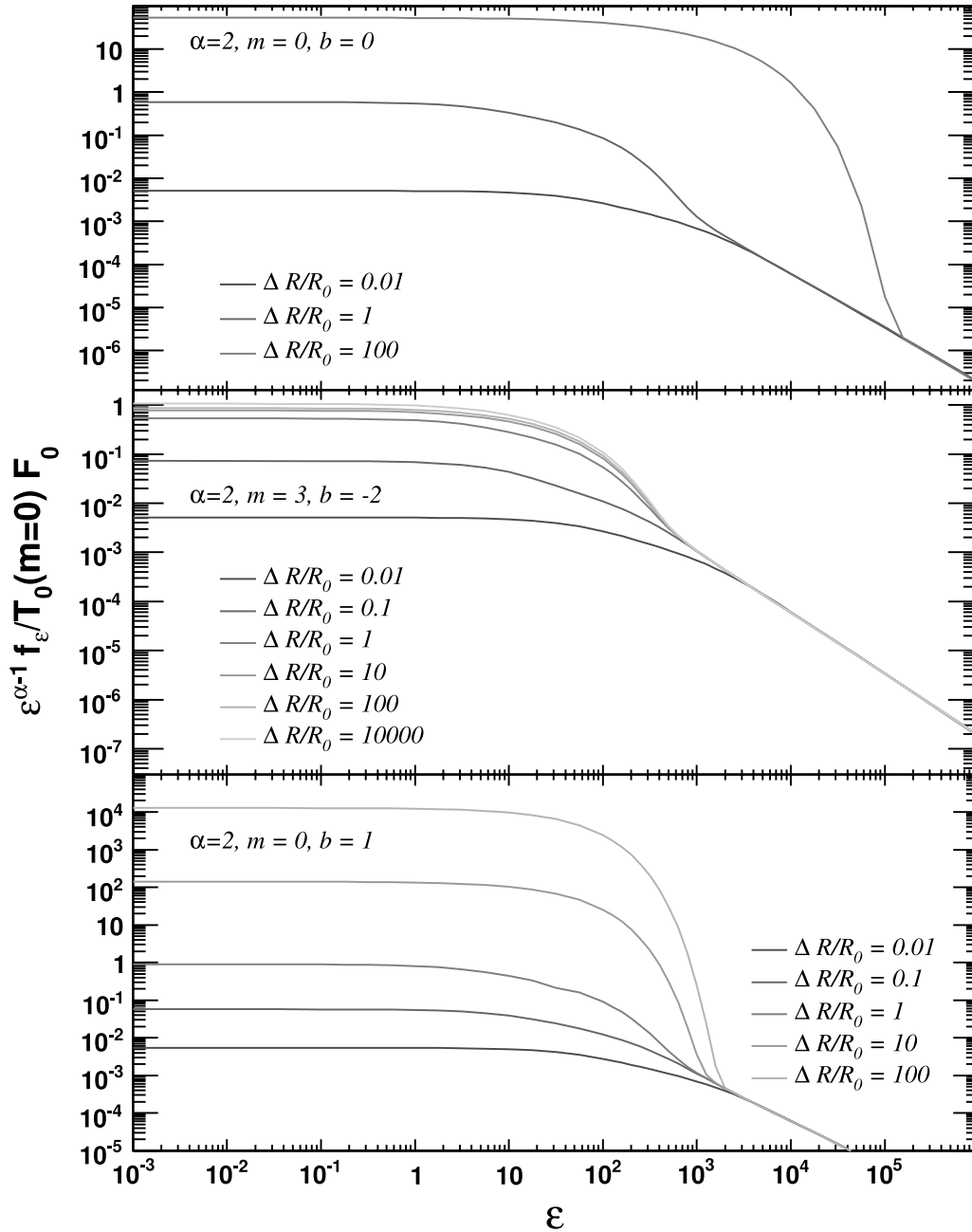


FIG. 13.— Time-integrated spectra for different values of $\Delta R/R_0$, while fixing the values of the other parameters. In the top panel $m = b = 0$, in the middle panel $m = 3$ and $b = -2$, while in the bottom panel $m = 0$ and $b = 1$. The values of the other model parameters in all the panels are $\alpha = 2$ and $\tau_* = 1$. [See the electronic edition of the *Journal* for a color version of this figure.]

TABLE 2
THE DIFFERENT SETS OF PARAMETERS FOR WHICH RESULTS
ARE SHOWN IN THIS WORK

α	m	b	$\log_{10}(\Delta R/R_0)$	Figures
2	0	0	-2, -1, 0, 1, 2	9, 13
2	0	1	-2, -1, 0, 1, 2	13
2	3	-2	-2, -1, 0, 1, 2, 4	13
2	0, 1, 2	0	2	10
2	0	-2, -1, 0	2	11
2, 3, 4	0	0	0	12

in the figures since we show $\varepsilon^{\alpha-1}F_\varepsilon$ which is independent of ε below ε_1). The time-integrated spectrum varies with the value of $\Delta R/R_0$. For $\Delta R/R_0 \ll 1$ it consists of three power-law segments, as described in equation (119). As $\Delta R/R_0$ increases, the central power-law segment, at $\varepsilon_{1i}(\bar{T}_f) < \varepsilon < \varepsilon_{1f}(\bar{T}_f)$, shrinks as $\varepsilon_{1i}(\bar{T}_f)$ and $\varepsilon_{1f}(\bar{T}_f)$ approach each other, until it disappears for $\Delta R/R_0 \sim 1$ where $\bar{T}_f \sim 1$ and $\varepsilon_{1i}(\bar{T}_f) \sim \varepsilon_{1f}(\bar{T}_f) \sim \varepsilon_{1*}$. For $\Delta R/R_0 \sim 1$ the time-integrated spectrum is described by equation (118) and consists of two power-law segments. As $\Delta R/R_0$ increases above unity, the time-integrated spectrum develops an exponential high-energy cutoff, while the power-law tail at high energies becomes increasingly suppressed. This occurs because if the flux at $1 < \bar{T} < \bar{T}_f$ does not drop faster than \bar{T}^{-1} , which corresponds to $m(\alpha - 2) < 2(b + 1)$ (see eq. [112]) as is indeed the case for the parameter values used in Fig. 9, then the time-integrated flux is dominated by contributions from $\bar{T} \sim \bar{T}_f \gg 1$ and reflects the exponential cutoff of the instantaneous spectrum at that time, which dominates over the high-energy power-law component that arises from the superposition of the instantaneous spectra from $\bar{T} \lesssim 1$.

Figures 10 and 11 demonstrate the effects of the two parameters m and b . As discussed above, a large value for $\Delta R/R_0$ (100) was chosen so that the radial dependence of the Lorentz factor ($\Gamma^2 \propto R^{-m}$) and of the comoving spectral luminosity [$L'_\varepsilon \propto R^b(\varepsilon')^{1-\alpha}$] would have a large effect on the light curves. For $\Delta R/R_0 \ll 1$ the values of m and b hardly affect the light curves (since the emission takes place over a very small range of radii in which both Γ and L'_ε hardly vary). Figure 10 also demonstrates the dependence of \bar{T}_f on m , where in the limit of $\Delta R/R_0 \gg 1$, $\bar{T}_f \approx (\Delta R/R_0)^{m+1}$ (see eq. [111]).

As can be seen in Figure 10, the power-law component of the time-integrated spectrum is largely independent of m , since it originates from the superposition of the instantaneous spectra at $\bar{T} \lesssim 1$, which are sampling a small range of emission radii. The lower energy component, however, from the contribution of the emission at times $1 < \bar{T} \lesssim \bar{T}_f$, is sensitive to the value of m , since it samples a large range of emission radii. For $m = 0$, $F_\varepsilon(1 < \bar{T} < \bar{T}_f)$ is constant in time (for the values of the other parameters that are used in Fig. 10), while $\varepsilon_1(1 < \bar{T} < \bar{T}_f) \propto \bar{T}$, and both effects combine to produce a very pronounced high-energy exponential cutoff. For $m = 1$, $F_\varepsilon(1 < \bar{T} < \bar{T}_f) \propto \bar{T}^{-1/2}$ while $\varepsilon_1(1 < \bar{T} < \bar{T}_f)$ is constant in time, which results in a somewhat less pronounced, although still fairly large high-energy exponential cutoff in the time-integrated spectrum. For $m = 2$, $F_\varepsilon(1 < \bar{T} < \bar{T}_f) \propto \bar{T}^{-2/3}$ while $\varepsilon_1(1 < \bar{T} < \bar{T}_f) \propto \bar{T}^{-1/3}$, so that the time-integrated spectrum in the range $\varepsilon_1(\bar{T}_f) < \varepsilon < \varepsilon_1(\bar{T} = 1) \sim \varepsilon_{1*}$ is dominated by the contributions near the time $T_1(\varepsilon)$ when $\varepsilon_1(\bar{T}_1) = \varepsilon$. This results in a spectral slope of $\varepsilon f_\varepsilon \propto \varepsilon^{-1}$ in the bottom panel of Figure 10.

More generally, $F_{\varepsilon < \varepsilon_1(\bar{T})}(1 < \bar{T} < \bar{T}_f) \sim \varepsilon^{1-\alpha} \bar{T}^{(2b-m\alpha)/(2(m+1))}$ while $\varepsilon_1(1 < \bar{T} < \bar{T}_f) \sim \varepsilon_{1*} \bar{T}^{(1-b-m\alpha/2)/[(m+1)(\alpha-1)]}$, so that when the flux is dominated by the contribution from $\bar{T} \sim \bar{T}_1(\varepsilon)$, then the spectral slope of the time-integrated spectrum is given by

$$\frac{d \log \varepsilon^{\alpha-1} f_\varepsilon}{d \log \varepsilon} = \frac{(\alpha - 1)[m(2 - \alpha) + 2(b + 1)]}{2(1 - b) - m\alpha}. \quad (120)$$

This may be relevant if $\varepsilon_1(1 < \bar{T} < \bar{T}_f)$ decreases with \bar{T} , in which case this spectral slope is valid in the range $\varepsilon_1(\bar{T}_f) < \varepsilon < \varepsilon_{1*}$. It may also be relevant if $\varepsilon_1(1 < \bar{T} < \bar{T}_f)$ increases with \bar{T} , as discussed below.

In Figure 11, the top panel is identical to the top panel of Figure 10 and the bottom panel of Figure 9. In the middle panel of Figure 11, $F_\varepsilon(1 < \bar{T} < \bar{T}_f) \propto \bar{T}^{-1}$ and $\varepsilon_1(1 < \bar{T} < \bar{T}_f) \propto \bar{T}^2$, while in the bottom panel $F_\varepsilon(1 < \bar{T} < \bar{T}_f) \propto \bar{T}^{-2}$ and $\varepsilon_1(1 < \bar{T} < \bar{T}_f) \propto \bar{T}^3$. Both cases result in a very pronounced exponential cutoff at very high photon energies (which may be hard to detect), but show a shallow spectral slope up to this exponential cutoff (which may be easier to detect). This again results in the spectral slope given by equation (120). However, in this case $\varepsilon_1(1 < \bar{T} < \bar{T}_f)$ increases with \bar{T} , and therefore, this spectral slope occurs in the range $\varepsilon_{1*} < \varepsilon < \varepsilon_1(\bar{T}_f)$. This is valid, however, only if indeed the time-integrated flux in this spectral range is dominated by the contribution from near $T_1(\varepsilon)$. This is not valid in the top panel of Figure 11 (where it is dominated by the contribution from $\bar{T} \sim \bar{T}_f$) and is only marginally valid in the middle panel (where the contributions from all the times in the range $T_1(\varepsilon) \lesssim \bar{T} \lesssim \bar{T}_f$ are comparable). In the bottom panel of Figure 11 the flux in this spectral range is indeed dominated by the contribution from $\bar{T} \sim \bar{T}_1(\varepsilon)$, which results in a spectral slope of $\varepsilon f_\varepsilon \propto \varepsilon^{-1/3}$ in this range.

In Figure 12, which shows the effect of varying α , the top panel corresponds to $\alpha = 1$, for which both the flux and the optical depth become independent of ε . As a result, we present for this case light curves for different values of τ_* and the corresponding integrated spectra (which all have a flat f_ε and vary only in their normalization). For $\alpha = 2$ (Fig. 12, *middle*) and $\alpha = 3$ (Fig. 12, *bottom*), one can verify that the power laws on the middle and bottom right panels have an index of approximately 4/3 and 5/2, respectively, as expected from equation (118) after rescaling by $\varepsilon^{\alpha-1}$.

Finally, Figure 13 illustrates the behavior of the time-integrated spectra, as discussed at the end of § 5. All the curves show a high-energy power-law tail with an index of about 4/3, as expected from equation (118). Moreover, given the rescaling by $T_0(m = 0)$ (which is independent of m) in Figure 13, it is easier to see that the time-integrated spectra become independent of b and m for $\Delta R/R_0 \ll 1$ (since in that limit, the same holds for the light curves and instantaneous spectra). As discussed in the paragraph following equation (118), the exponential cutoff is suppressed when $m(\alpha - 2) > 2(b + 1)$, as is the case on Figure 13's middle panel only. In such a case, the time-integrated spectra are dominated by contributions near $\bar{T} \sim 1$, and the effect of $\Delta R/R_0$ becomes negligible for $\Delta R/R_0 \gg 1$, which explains the asymptotic behavior of the spectra with increasing $\Delta R/R_0$. Finally, for very impulsive sources, the intermediate power-law segment in equation (119) can be discerned, albeit with difficulty.

7. DISCUSSION

We have explored in great detail a model for the temporal and spatial dependence of the opacity to pair production ($\gamma\gamma \rightarrow e^+e^-$) in impulsive relativistic sources. Our simple, yet rich, model features a thin spherical shell expanding ultrarelativistically and emitting isotropically in its own rest frame within a finite range of radii. Our two main results are the following. First, while the instantaneous spectrum (which is typically very hard to measure due to poor photon statistics) has an exponential cutoff at high photon energies, the time-integrated spectrum over the duration of a flare or spike in the light curve (which is easier to measure) has a power-law high-energy tail. Second, photons above this spectral break in the time-integrated spectrum arrive mainly near the onset of the flare or spike in the light curve.

These two features provide a unique detectable signature of opacity to pair production, making it easier to identify observationally. Furthermore, these features are expected to be fairly robust, even if the exact details (such as the exact change in the spectral slope across the break, $\Delta\alpha$ or the exact shape of the light curve at high photon energies above the spectral break) may depend on the details of the model (such as the exact geometry, which is assumed to be spherical in our model⁸). The reason behind these features is that in impulsive sources the photon field starts from zero (or more realistically a nonzero value, which is still much lower than that near the peak of the flare or spike in the light curve) and builds up with time, so that the optical depth to pair production, $\tau_{\gamma\gamma}$, increases with time, and high-energy photons can escape mainly at early times while $\tau_{\gamma\gamma}$ is still below unity.

A source is considered impulsive for our purposes if the photon field in the source and its vicinity changes considerably within the source light crossing time. In this limit the time dependence of the photon field and the resulting opacity to pair production is important. This can naturally occur in relativistic sources, but is hard to produce in nonrelativistic sources (since it requires a relativistic signal in order to turn the emission on or off on a timescale of the order of the light crossing time of the source). In the opposite limit, where the photon field hardly varies within the source light crossing time, the photon field may be approximated as constant in time along the trajectory of the photons, and can be evaluated at the time of emission (this is considered a “quasi-steady state”). In our model, in order for the source to be impulsive, the duration of the emission should be at most comparable to the light crossing time of the source ($\bar{T}_f \lesssim 1 \Leftrightarrow \Delta R/R_0 \lesssim 1$). If the source is active for much longer times ($\bar{T}_f \gg 1 \Leftrightarrow \Delta R/R_0 \gg 1$), then the photon field approaches a quasi-steady state⁹ within a few light crossing times of the emitting region ($\bar{T}_f > \bar{T} \gtrsim \text{a few}$), and the time-integrated spectrum will usually be dominated by this late-time quasi-steady emission. This can result in an exponential high-energy cutoff in the time-integrated spectrum, which dominates over the high-energy power-law tail from the emission at early times ($\bar{T} \lesssim 1$), and may also introduce an intermediate power-law segment (described by eq. [120]).

When the source is inhomogeneous, in the sense that the optical depth to pair production out to infinity (i.e., to the distant observer), $\tau_{\gamma\gamma}$, varies considerably between different parts of the emitting region, an intermediate power law can develop in the instantaneous spectrum, due to the summation over the contributions from the different parts of the source, each of which has a different value for the photon energy ε_1 at which $\tau_{\gamma\gamma} = 1$ and above which the local emitted spectrum cuts off exponentially. In our model this occurs at $\bar{T}_f > \bar{T} \ll 1$, where $\tau_{\gamma\gamma}$ varies considerably along the equal arrival time surface to the observer (EAST-I; see right panel of Fig. 7), and as a result, an intermediate power law develops in the instantaneous spectrum (see eq. [117]). For highly impulsive sources ($\Delta R \ll R_0$) it is also reflected in the time-integrated spectrum (eq. [119]). Such an intermediate power-law spectrum is obtained in quasi-steady inhomogeneous AGN jets in which the emission takes place over a wide range of radii, where ε_1 increases with radius and the emission at each photon energy is dominated by the contribution from near the radius R where $\varepsilon_1(R) = \varepsilon$ (Blandford & Levinson 1995). In our model, at later times ($1 \lesssim \bar{T} < \bar{T}_f$) the opacity becomes roughly uniform along the EASTS-I (see left panel of Fig. 7), resulting in the disappearance of the intermediate power-law segment in the instantaneous spectrum, and the exponential cutoff starts directly from the unattenuated part of the spectrum.

Another analogy to a known result from inhomogeneous AGN jets (Blandford & Levinson 1995) is a soft to hard spectral evolution at high energies as the emission moves from smaller to larger radii, again since ε_1 increases with radius. We obtain a similar behavior if the emission occurs over a wide range of radii, $\Delta R \gg R_0$, in the quasi-steady regime ($1 \ll \bar{T} < \bar{T}_f$), as can be seen in the bottom panel of Figure 9. In the impulsive regime ($\bar{T} \ll 1$) ε_1 decreases with time as the opacity builds up (hard to soft evolution), while during the quasi-steady regime ($1 \ll \bar{T} < \bar{T}_f$) ε_1 can either increase with time (soft to hard evolution; e.g., middle and bottom panels of Fig. 11), remain constant (e.g., middle panel of Fig. 10), or decrease with time (hard to soft evolution; e.g., bottom panel of Fig. 10), depending on the values of the model parameters. This can result in an intermediate power-law segment in the time-integrated spectrum (which is described by eq. [120]; see also the bottom panel of Fig. 11).

We have considered a single, isolated emission episode which corresponds to a single flare or spike in the observed light curve. Furthermore, we have assumed no background photon field at the time when the emission turns on. These are obviously idealized assumptions and it is worth considering, at least qualitatively at this stage, the modifications that may occur when these ideal conditions are not satisfied. For the prompt emission or X-ray flares in GRBs, the background quasi-steady photon field is usually expected to be very low and not contribute significantly to $\tau_{\gamma\gamma}$. In some nonstandard scenarios (e.g., Königl & Granot 2002; Guetta & Granot 2003) the external radiation field may dominate $\tau_{\gamma\gamma}$. In such cases our model would not be applicable, since the external radiation field would prevent the escape of high-energy photons near the onset of the spike, resulting in $\tau_{\gamma\gamma}$ that is largely independent of time. This different expected observational signature can be used in order to test such models. For blazars it is not always clear whether the internal or external radiation fields dominate $\tau_{\gamma\gamma}$ (and this is also somewhat model dependent), and a more careful examination of the relative strengths of the external and internal radiation field as a function of time, Doppler factor, and radial distance would be in order (e.g., Sikora et al. 1994; Dermer & Schlickeiser 1994; Begelman et al. 2007). This interesting question deserves a more thorough treatment, which is beyond the scope of this paper.

Regarding the assumption that the flare/spike is isolated, in many cases there are series of flares, so that except for the first flare in the series for which our assumption should hold very well, for consecutive flares the high-energy photons could in principle pair produce with photons emitted in previous flares. This will be highly suppressed if the time from the end of the previous flare is much larger than its duration. Even if these two times are comparable, pair production is still significantly suppressed.¹⁰ Such a proximity in time to a previous flare/spike will still increase $\tau_{\gamma\gamma}$ to some degree, but this will affect mainly the highest energy photons, with energies well above the spectral break in the time-integrated spectrum over the duration of the flare/spike, which are relatively hard to detect due to the

⁸ In AGNs, for example, a cylindrical geometry may be more appropriate. We intend to study such a cylindrical geometry in a future work.

⁹ Here, by quasi-steady state, we mean that neglecting the time dependence of the photon field would at most change the results by a factor of order unity, but not qualitatively.

¹⁰ This occurs since if photons from an earlier flare are emitted at close to the radial direction, they can meet (and potentially pair produce with) photons from the later flare only at large radii, where the photon density is smaller and the angle between the directions of the photons (in the lab frame) is small, while in order to meet the photons from the later flare at close to their emission radius, they must be emitted at large angles relative to the radial direction, into which few photons are emitted due to the aberration of light (i.e., relativistic beaming).

smaller number of photons at such high energies. Therefore, in practical terms, the differences from our idealized model are not expected to be very large. This may even make it meaningful to integrate the spectrum over many spikes/flares in order to increase the photon statistics, in cases where the number of photons detected in individual spikes is not large enough to enable a good spectral analysis.

Other sources of opacity, such as scattering of photons on the pairs that are produced, are also possible. The latter, however, is expected to build up in time on a comparable timescale to that of the opacity to pair production that we study here. Therefore, it is not expected to have a significant impact on our main conclusions. Opacity for scattering on the electrons associated with the baryons or with preexisting pairs within the outflow is also possible. However, it will not vary greatly within a single dynamical time and should also affect lower energy photons (where the larger number of photons enables a better spectral analysis). Furthermore, it is suppressed at high photon energies due to the reduction in the cross section in the Klein-Nishina regime. Moreover, we find a rather unique combined spectral and temporal signature for the opacity to pair production, which could help distinguish between it and other sources of opacity.

Sufficiently high energy photons, of energy $\varepsilon \gg \varepsilon_1$, have $\tau_{\gamma\gamma}(\varepsilon) \gg 1$ and therefore pair produce with lower energy photons. The pairs that are produced can in turn upscatter lower energy photons to high energies and produce second-generation photons, some of which carry a fair fraction of the initial photon energy. This produces a pair cascade, which continues until eventually (and typically after several such cycles) the photons cascade down in energy to $\lesssim \varepsilon_1$ and can escape. This can in principle enhance the observed spectrum near ε_1 (e.g., Blandford & Levinson 1995), especially if there was originally more energy in higher energy photons ($\alpha < 2$). In GRBs, however, the Compton y -parameter is expected to be $Y \lesssim 1$, so that the pairs that are produced would radiate a good part of their energy into the synchrotron channel, rather than inverse Compton scattering of soft photons into high-energy photons that would continue the pair cascade. Therefore, by the time several generations of pairs are produced (in order to cascade down in energy to $\lesssim \varepsilon_1$ and escape), most of the original energy is lost through the synchrotron channel, and only a small fraction of that energy remains in the high-energy photons that escape. The synchrotron emission from the pairs peaks at much lower photon energies and can therefore escape. Furthermore, it does not directly contribute to the spectrum at the high photon energies which are the topic of this work. In AGN jets it may have a larger effect on the high-energy part of the spectrum.

The photons from the pair cascade reach the observer at a time delay compared to the arrival time of the original photon that initiated it if it had not pair produced. This arises since the e^\pm pairs gyrate in the magnetic field inside the source before upscattering a soft photon, so that the upscattered photon moves in a direction different than the original high-energy photon that pair produced. Thus, the photons of successive generations in the cascade perform a random walk (of increasing step size, since their mean free path increases as they cascade down in energy), until they can escape, resulting in $\Delta T \sim \bar{T}$. When the source turns on, both the opacity and the unattenuated flux initially increase with time. The increase in the opacity with time increases the time delay described above, and during this time, the unattenuated flux rises by a larger factor. This causes the relative contribution to the instantaneous spectrum at early times to be even smaller. This effect is more important in impulsive sources. Since the main results of our work rely on the early spectra during the rising stage, the effects of pair cascades should not qualitatively change our conclusions. Some quantitative differences are possible, depending on the parameter regime (e.g., a larger effect is expected for a harder initial spectrum, with $\alpha < 2$).

In GRB afterglows the opacity to pair production is typically very low and therefore not expected to be detectable in the *GLAST* energy range. During the afterglow, after about one day, $L_{0.52} \sim 10^{-8}$ to 10^{-7} , $R \sim 10^{17}$ cm corresponding to $R_{0.13} \sim 10^4$, and $\Gamma \sim 10$ corresponding to $\Gamma_{0.2} \sim 0.1$. According to equation (124), this implies a huge value of ε_{1*} ($\varepsilon_{1*} m_e c^2 \sim 10^{15} - 10^{16}$ eV for $\alpha \approx 2$). In practice, the opacity would be even lower than this, since the typical energy of the photons that would pair produce with such high-energy photons would be $\sim \Gamma^2 / \varepsilon_{1*}$ corresponding to $\nu \sim 10^{12}$ Hz, which is well below the assumed power-law segment of the spectrum (so that the number density of these low-energy photons would in practice be much lower than the default value according to our assumption of a simple single power-law spectrum). A possible exception to the very low $\tau_{\gamma\gamma}$ during the afterglow may be the very early afterglow in a stellar wind environment, near T_{dec} which is of the order of seconds in this case. Typical parameters values there are $R_{0.13} \sim 100$, $\Gamma_{0.2} \sim 1$, and $L_{0.52} \sim 0.1$, which might give $\varepsilon_{1*} m_e c^2$ as low as ~ 100 GeV. Such values could be detected by *GLAST*, albeit with difficulty.

For the internal shocks model, the GRB prompt emission occurs at a much smaller radius compared to the afterglow, $R_{\text{GRB}} \ll R_{\text{dec}}$. Furthermore, the luminosity of the prompt GRB emission is much larger than that of the afterglow, and the Lorentz factor is higher. Therefore, despite the higher Lorentz factor during the prompt GRB, $\tau_{\gamma\gamma}$ is still much larger than during the afterglow. In models where the prompt emission occurs near the deceleration radius, $R_{\text{GRB}} \sim R_{\text{dec}}$, the values of $\tau_{\gamma\gamma}$ in the very early afterglow and in the prompt emission are comparable (perhaps somewhat smaller in the early afterglow due to a smaller radiative efficiency), but $\tau_{\gamma\gamma}$ is typically very low for both emission components (i.e., the effects of opacity to pair production are not expected in the *GLAST* energy range).

Once the spectral break in the time-integrated spectrum over the duration of a flare or spike in the light curve is observed in the data, it can be used to constrain the values of the physical parameters of the source, namely, $\Gamma_0^{2\alpha} R_0$. A fit of our model predictions to the data can in principle determine the values of all the model parameters: α , m , b , $\Delta R/R_0$, τ_* , and F_0 , which in turn determine L_0 (from F_0 , eq. [96]) and $\Gamma_0^{2\alpha} R_0$ (from τ_* , eq. [37]). In practice, however, the limited photon statistics may render such a direct fit with such a large number of free parameters impractical. One way to overcome this problem is to fix the values of some of the model parameters, e.g., $m = b = 0$ and even $\Delta R/R_0 = 1$, if necessary.

A less accurate but less computationally demanding alternative is to fit the time-integrated spectrum (over a flare or spike in the light curve) to a parameterized function featuring a smooth transition between two power laws,

$$f_\varepsilon = f_0 \left[\left(\frac{\varepsilon}{\varepsilon_{1*}} \right)^{-n(1-\alpha)} + \left(\frac{\varepsilon}{\varepsilon_{1*}} \right)^{-n(1-\alpha-\Delta\alpha)} \right]^{-1/n}, \quad (121)$$

where n and f_0 determine the sharpness of the spectral break at ε_{1*} and its flux normalization, respectively, while $f_\varepsilon \ll \varepsilon_{1*} \propto \varepsilon^{1-\alpha}$ and $f_\varepsilon \gg \varepsilon_{1*} \propto \varepsilon^{1-\alpha-\Delta\alpha}$. Such a fit can determine both the photon index, α , and the photon energy $\varepsilon_{1*} \approx \varepsilon_1(\bar{T} = 1)$ of the spectral break in

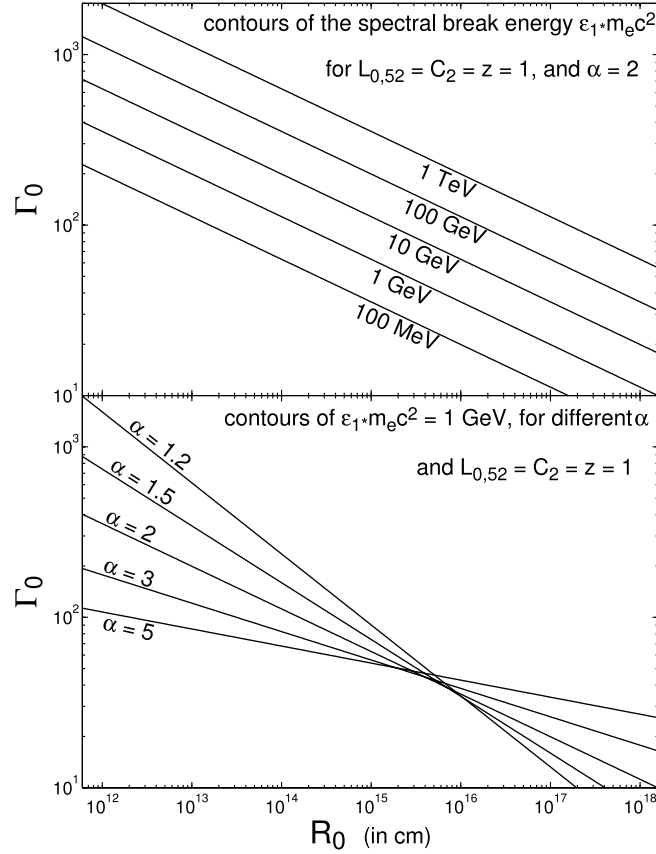


FIG. 14.—Contour lines for the photon energy $\varepsilon_{1*} m_e c^2$ where the time-integrated spectrum over a flare or spike in the light curve steepens due to opacity to pair production, shown in the Γ_0 - R_0 plane, according to eq. (124). In the top panel $\varepsilon_{1*} m_e c^2$ is varied and $\alpha = 2$ is fixed, while in the bottom panel α is varied and $\varepsilon_{1*} m_e c^2 = 1$ GeV is fixed. In both panels $L_{0,51} = C_2 = z = 1$. [See the electronic edition of the Journal for a color version of this figure.]

the time-integrated spectrum, as well as F_0 . For $\Delta R/R_0 \lesssim 1$ and defining ΔT as the observed variability time (in seconds), e.g., the observed FWHM of the flare or spike in the light curve, we have $f_0/\Delta T \approx \bar{T}_f F_0 \varepsilon_{1*}^{1-\alpha} \sim F_0 \varepsilon_{1*}^{1-\alpha} \Delta R/R_0$, which can be used in equation (96) to determine L_0 ,

$$L_0 \approx \pi d_L^2 \frac{f_0}{\Delta T} \frac{R_0}{\Delta R} \left(\frac{1+z}{2}\right)^{\alpha-2} \varepsilon_{1*}^{\alpha-1} = 1.3 \times 10^{51} \frac{R_0}{\Delta R} \left(\frac{1+z}{2}\right)^{\alpha-2} d_{L,z1}^2 \frac{f_{0,-6}}{\Delta T} \varepsilon_{1*}^{\alpha-1} \text{ erg s}^{-1}, \quad (122)$$

where $f_0 = 10^{-6} f_{0,-6}$ erg cm $^{-2}$ and $d_{L,z1}$ is d_L in units of $d_L(z=1) \approx 2.05 \times 10^{28}$ cm (for standard cosmological parameters). It is hard to determine $\Delta R/R_0$ without a detailed fit to the model spectra (see Fig. 13 for the dependence of the time-integrated spectrum on $\Delta R/R_0$), and this is a price for the simplicity of this method and the use of simple analytic formulae rather than numerically evaluating the set of nested integrals in order to calculate our model predictions. One can either assume $\Delta R/R_0 \approx 1$ or try to estimate its values by eye, guided by Figure 13, if one wishes to avoid a direct fit to the model predictions.

The quantities α , L_0 , and ε_{1*} may in turn be used to determine $\Gamma_0^2 R_0$. In order to do this in practice, we need to use equation (37) and the relation

$$(1+z)\varepsilon_{1*} \equiv (\tau_*/C_\alpha)^{-1/(\alpha-1)} = \left[249C_2(\alpha/2)^{5/3} 10^{4(\alpha-2)} L_{0,52}^{-1} (\Gamma_{0,2})^{2\alpha} R_{0,13}\right]^{1/(\alpha-1)}, \quad (123)$$

$$\varepsilon_{1*} m_e c^2 = \frac{127 \text{ MeV}}{(1+z)} \left[C_2 (40.2)^{\alpha-2} \left(\frac{\alpha}{2}\right)^{5/3} \frac{(\Gamma_{0,2})^{2\alpha} R_{0,13}}{L_{0,52}} \right]^{1/(\alpha-1)}, \quad (124)$$

where $C_\alpha = 100C_2$ is a coefficient whose value is determined numerically. The dependence of ε_{1*} on Γ_0 , R_0 , and α is demonstrated in Figure 14. Since a test photon of dimensionless energy ε_{1*} pair produces primarily with photons of energy $\sim \Gamma^2/(1+z)^2 \varepsilon_{1*}$, and we fix the value of L_0 [i.e., the photon number density near $(1+z)\varepsilon = 1$], the values of ε_{1*} becomes almost independent of α near $\Gamma_0 \sim [(1+z)\varepsilon_{1*}]^{1/2}$ (which is roughly where the lines for the three values of α for the same value of ε_{1*} almost meet).

Equation (124) can be inverted in order to obtain

$$(\Gamma_{0,2})^{2\alpha} R_{0,13} = C_2^{-1} 40.2^{2-\alpha} \left(\frac{\alpha}{2}\right)^{-5/3} L_{0,52} \left[\frac{(1+z)\varepsilon_{1*} m_e c^2}{127 \text{ MeV}} \right]^{\alpha-1}. \quad (125)$$

If one makes the additional assumption that $R_0 \sim \Gamma_0^2 c \Delta T / (1+z)$, which is valid for a large class of models, then equation (125) provides the following estimate for Γ_0 ,

$$\Gamma_0 \approx 100(1+z)^{\alpha/(2\alpha+2)} \left[\frac{1.34}{C_2} \left(\frac{\alpha}{2} \right)^{-5/3} \frac{L_{0.52}}{(\Delta T/1 \text{ s})} \right]^{1/(2\alpha+2)} \left(\frac{\varepsilon_{1*} m_e c^2}{5.1 \text{ GeV}} \right)^{(\alpha-1)/(2\alpha+2)}. \quad (126)$$

For GRBs, one may perform a consistency check for the assumption that $R_0 \sim \Gamma_0^2 c \Delta T / (1+z)$ by comparing the value of Γ_0 under this assumption from opacity to pair production (eq. [126]) to the estimate for Γ_0 from the time, T_{dec} , of the onset of the afterglow emission,¹¹

$$\Gamma_0(T_{\text{dec}}) \approx \left[\frac{(3-k)E_{\text{iso}}}{\pi A (2c)^{5-k} T_{\text{dec}}^{3-k}} \right]^{1/2(4-k)} = \begin{cases} 128 E_{\text{iso},53}^{1/8} n_0^{-1/8} T_{\text{dec},2}^{-3/8}, & k=0, \\ 131 E_{\text{iso},53}^{1/4} A_*^{-1/4} T_{\text{dec},0}^{-1/4}, & k=2, \end{cases} \quad (127)$$

where $T_{\text{dec}} = T_{\text{dec},0} \text{ s} = 100 T_{\text{dec},2} \text{ s}$, $E_{\text{iso}} = 10^{53} E_{\text{iso},53} \text{ erg}$ is the isotropic equivalent kinetic energy in the outflow, $\rho_{\text{ext}} = AR^{-k}$ is the external density and is assumed to be a power law with radius, which is $\rho_{\text{ext}} = nm_p$ for a uniform external medium ($k=0$) of number density $n = n_0 \text{ cm}^{-3}$, while $A = 5 \times 10^{11} A_* \text{ g cm}^{-1}$ for a stellar wind environment ($k=2$).

We thank M. Peskin, M. G. Baring, P. Coppi, L. Stawarz, and G. Madejski for useful discussions. This work is supported by the US Department of Energy under contract DE-AC02-76SF00515. J. G. gratefully acknowledges a Royal Society Wolfson Research Merit Award.

APPENDIX A

CHANGES OF VARIABLES IN § 3.2

A1. CHANGE OF VARIABLE FROM (s, μ_r) TO (R_e, R_t)

Since we integrate over $d\Omega_r = d\phi_r d\mu_r$ and the integrand contains $|d\mu_e/d\mu_r|$, we can conveniently change variables from μ_r to \tilde{R}_e . It is straightforward to verify that, irrespective of the position of R_t with respect to the upper bound of R_e , $|d\mu_e/d\mu_r| d\mu_r = (d\mu_e/d\tilde{R}_e) d\tilde{R}_e$, with the integration over \tilde{R}_e being performed from the smaller to the larger bound, and $d\mu_e/d\tilde{R}_e > 0$ always. Furthermore, the perpendicular distance from the line of sight from the center of the emitting sphere to the observer at infinity,

$$R_{\perp} \equiv R_{t,0} \sin \theta_{t,0} = R_t \sin \theta_t, \quad (A1)$$

is constant along the trajectory of the test photon (see Fig. 2). Thus,

$$s = R_t \cos \theta_t - R_{t,0} \cos \theta_{t,0}, \quad ds = -\frac{R_{\perp} d\theta_t}{\sin^2 \theta_t} = \frac{R_{\perp} d\mu_t}{(1-\mu_t^2)^{3/2}} = \frac{R_t dR_t}{\sqrt{R_t^2 - R_{\perp}^2}} \approx R_{t,0} d\tilde{R}_t, \quad (A2)$$

where the last approximation holds since $R_{\perp} \leq R_{\perp,\text{max}} \approx R(R_{\perp,\text{max}})/\Gamma(R_{\perp,\text{max}}) = O(R_t/\Gamma) \ll R_t$ and the contribution from $R_t \ll R(R_{\perp,\text{max}})$ is negligible for $\Gamma \gg 1$.

A2. INTEGRATION OVER $d\phi_r$ AND $d\varepsilon_i$

The local photon field derived above is symmetric around the radial direction (i.e., does not depend on ϕ_r). As a consequence, ϕ_r appears only in the function $\sigma^*(\chi(\varepsilon_t, \varepsilon_i, \mu_{ti}))(1-\mu_{ti})$, where μ_{ti} is a function of $\cos \phi_r$ (see eq. [22]). Thus, we can write $\int_0^{2\pi} d\phi_r = 2 \int_0^{\pi} d\phi_r$. Next, we follow the insights of Stepney & Guilbert (1983) and Baring (1994) by performing the change of variables $(\varepsilon_i, \phi_r) \rightarrow (\chi, u)$, with $\chi^2 = \varepsilon_t \varepsilon_i u$ defined in equation (19). Defining $\zeta_+ = [1 - \cos(\theta_r + \theta_t)]/2$ and $\zeta_- = [1 - \cos(\theta_r - \theta_t)]/2$, where $\zeta_+ > \zeta_-$ for $(\theta_r, \theta_t) \in [0, \pi]$, equation (22) yields $\int_0^{\pi} d\phi_r = 2 \int_{\zeta_-}^{\zeta_+} du [(\zeta_+ - \zeta_-) \sin \phi_r]^{-1} = \int_{\zeta_-}^{\zeta_+} du [(\zeta_+ - u)(u - \zeta_-)]^{-1/2}$. Likewise $\int_{2/\varepsilon_t}^{\infty} d\varepsilon_i = 2 \int_1^{\infty} \chi d\chi (\varepsilon_t u)^{-1}$. Equation (34) now reads

$$\tau_{\gamma\gamma}(\varepsilon_t, \theta_{t,0}, R_{t,0}) = \frac{8\sigma_{\text{T}}}{(4\pi)^2 m_e c^3 R_{t,0}} \int_1^{\infty} \frac{d\tilde{R}_t}{\tilde{R}_t^2} \int d\tilde{R}_e \frac{\delta^3 d\mu_e}{\tilde{r}^2 d\tilde{R}_e} \int_{\zeta_-}^{\zeta_+} \frac{u du}{\sqrt{(\zeta_+ - u)(u - \zeta_-)}} \int_1^{\infty} \frac{d\chi}{\chi} \frac{\sigma^*(\chi)}{\sigma_{\text{T}}} L'_{\chi^2/\varepsilon_t u \delta}(\tilde{R}_e). \quad (A3)$$

$$A3. L'_{\varepsilon'_t}(R_e) = L'_0(\varepsilon'_t)^{1-\alpha} h(R_e/R_0).$$

The specific luminosity in the comoving frame is conveniently parameterized as $L'_{\varepsilon'} = L'_0(\varepsilon')^{1-\alpha} h(R_e/R_0)$, where $h(1) = 1$ is normalized at $R_e/R_0 = \tilde{R}_e \tilde{R}_t / \tilde{R}_0 = 1$. Similarly, we want to parameterize the specific luminosity in the lab frame at R_0 as $L_{\varepsilon}(R_0) \approx L_0 \varepsilon^{1-\alpha}$,

¹¹ This estimate is for the Lorentz factor of the outflow after the passage of the reverse shock, so it is close to that of the original outflow before it was decelerated by the reverse shock only as long as the reverse shock is at most mildly relativistic. For a highly relativistic reverse shock, the original Lorentz factor of the outflow can be much larger than this value.

even though the luminosity at a given radius is not really well defined, since the Doppler factor also depends on the angle $\theta_{t,0}$ from the line of sight. The normalization coefficients in the lab frame (L_0) and in the comoving frame (L'_0) are the specific luminosity at R_0 corresponding to a photon energy of $m_e c^2 \approx 511$ keV in the respective frames. Since the typical value of the Doppler factor is $\delta = \varepsilon/\varepsilon' \sim \Gamma$, and specifically $\delta(R_0) \sim \Gamma(R_0) \equiv \Gamma_0$, these coefficients are related by $L_0 \varepsilon^{1-\alpha} \sim \Gamma_0 L'_0 (\varepsilon')^{1-\alpha}$ and $L_0 \sim \Gamma_0^\alpha L'_0$. Thus motivated, we use this relation as the definition of L_0 , $L_0 \equiv \Gamma_0^\alpha L'_0$. Therefore, $L'_{\varepsilon'_i}(R_e) = \Gamma_0^{-\alpha} L_0 (\varepsilon'_i)^{1-\alpha} h(\tilde{R}_e \tilde{R}_t / \tilde{R}_0)$. It is convenient to express the optical depth $\tau_{\gamma\gamma}$ in terms of L_0 , which is approximately the observed isotropic equivalent luminosity at an observed photon energy of $511(1+z)^{-1}$ keV near $\bar{T} \sim 1$ for $\Delta R \gtrsim R_0$. For $\Delta R/R_0 \approx \bar{T}_f/(1+m) \ll 1$ (see eq. [111]), the peak isotropic equivalent luminosity at $511(1+z)^{-1}$ keV is $\sim \bar{T}_f L_0$ and the corresponding optical depth near the peak of the spike in the light curve at the same photon energy is $\sim \bar{T}_f \tau_0$. Therefore, L_0 is practically an observable quantity, making it convenient to work with.

Equation (A3) now becomes

$$\tau_{\gamma\gamma}(\varepsilon_t, \theta_{t,0}, R_{t,0}) = \frac{2\Gamma_0^{-\alpha} L_0 \varepsilon_t^{\alpha-1} \sigma_T}{(4\pi)^2 m_e c^3 R_{t,0}} \int_1^\infty \frac{d\tilde{R}_t}{\tilde{R}_t^2} \int d\tilde{R}_e \left(\frac{\delta^{2+\alpha}}{\tilde{r}^2} \frac{d\mu_e}{d\tilde{R}_e} \right) h\left(\frac{\tilde{R}_e \tilde{R}_t}{\tilde{R}_0}\right) \int_{\zeta_-}^{\zeta_+} \frac{u^\alpha du}{\sqrt{(\zeta_+ - u)(u - \zeta_-)}} \frac{4}{\sigma_T} \int_1^{+\infty} d\chi \chi^{-(2\alpha-1)} \sigma^*(\chi). \quad (\text{A4})$$

From equation (8) of Baring (1994) we can write, to a very good approximation,

$$\frac{4}{\sigma_T} \int_1^{+\infty} d\chi \chi^{-(2\alpha-1)} \sigma^*(\chi) \sim \frac{7}{6\alpha^{5/3}}. \quad (\text{A5})$$

Making the change of variable $u \rightarrow t = (u - \zeta_-)/(\zeta_+ - \zeta_-)$, we also have (see eq. 15.3.1 in Abramowitz & Stegun 1964)

$$\int_{\zeta_-}^{\zeta_+} \frac{u^\alpha du}{\sqrt{(\zeta_+ - u)(u - \zeta_-)}} = \zeta_-^\alpha \int_0^1 \frac{(1 + \zeta t)^\alpha}{\sqrt{t(1-t)}} dt \equiv \frac{\zeta_-^\alpha}{\pi} {}_2F_1(-\alpha, 0.5; 1; -\zeta), \quad (\text{A6})$$

where ${}_2F_1$ is a hypergeometric function and $\zeta = (\zeta_+ - \zeta_-)/\zeta_- > 0$. We define $H_\alpha(\zeta) \equiv {}_2F_1(-\alpha, 0.5; 1; -\zeta)$ and notice that it is regularized by the factor ζ_-^α when $\zeta_- \rightarrow 0$. Note that ζ is of order unity and $H_\alpha(\zeta)$ is a simple polynomial when α is an integer (see eq. 15.4.1 in Abramowitz & Stegun 1964 and our eqs. [104]–[106] for $\alpha = 1, 2$, and 3.).

APPENDIX B

JUSTIFICATION FOR THE APPROXIMATIONS IN CASE 1

When calculating the photon field at the instantaneous location of the test photon in case 1, where the test photons lags behind the shell, $R_t < R_{\text{sh}}(t)$, we have used an approximation for the value of θ_r , namely, equation (71), which is valid for $\theta_r \ll 1$ and breaks down for $\theta_r \sim 1$ which corresponds to $1 - \tilde{R}_e = O(\Gamma_t^{-2})$. This is despite the fact that in this case θ_r can assume any value between zero and π . The justification for this convenient approximation is that the contribution to the optical depth $\tau_{\gamma\gamma}$ from $\theta_r \sim 1$, where our approximation breaks, is negligible compared to the contribution from $\theta_r \ll 1$, where our approximation is valid. In order to show this more explicitly, we examine the dependence of the integrand in the integration over $d\tilde{R}_e$ on the value of θ_r in the range

$$\frac{1}{\Gamma_t} \ll \theta_r \ll 1 \iff \frac{1}{\Gamma_t^2} \ll \tilde{R}_{\text{sh}} - \tilde{R}_e \approx 1 - \tilde{R}_e \ll 1, \quad (\text{B1})$$

which gives us a handle (up to factors of order unity) on its dependence throughout the entire range of possible θ_r values. In this intermediate range of θ_r values, $\tilde{R}_{\text{sh}} - \tilde{R}_e \approx 1 - \tilde{R}_e$ since for case 1 $\Gamma_t^2(\tilde{R}_{\text{sh}} - 1) \lesssim$ a few, and thus,

$$\tilde{r}^2 = (\tilde{R}_{\text{sh}} - \tilde{R}_e)^2 + \frac{(\tilde{R}_{\text{sh}} - \tilde{R}_e)(\tilde{R}_{\text{sh}}^{m+1} - \tilde{R}_e^{m+1})}{(m+1)\Gamma_t^2} + O(\Gamma_t^{-4}) \approx (\tilde{R}_{\text{sh}} - \tilde{R}_e)^2 \approx (1 - \tilde{R}_e)^2. \quad (\text{B2})$$

Likewise, equation (52) yields

$$\frac{d\mu_e}{d\tilde{R}_e} \approx \frac{1}{2\Gamma_t^2 \tilde{R}_e^2} \left[\Gamma_t^2 (\tilde{R}_{\text{sh}}^2 - 1) + \frac{1}{m+1} (1 + m\tilde{R}_e^{m+1}) - \tilde{R}_e^{m+2} \right] \quad (\text{B3})$$

$$\approx \frac{f_m - \tilde{R}_e^{m+1}}{2(m+1)\Gamma_t^2 \tilde{R}_e^2} \approx \frac{f_m - 1}{2(m+1)\Gamma_t^2}. \quad (\text{B4})$$

Thus, we see that in this intermediate range of θ_r values $d\mu_e/d\tilde{R}_e$ is approximately constant and is of order Γ_t^{-2} . Besides, H_α is of order unity, $\zeta_- \sim \theta_r^2$, and $\delta \sim \Gamma^{-1}\theta_r^{-2}$, so that

$$\frac{\delta^{\alpha+2}}{\tilde{r}^2} \frac{d\mu_e}{d\tilde{R}_e} \zeta_-^\alpha H_\alpha(\zeta) \sim \frac{1}{\Gamma_t^{4+\alpha} (1 - \tilde{R}_e)^2 \theta_r^4} \propto \frac{1}{(1 - \tilde{R}_e)^2 \theta_r^4}. \quad (\text{B5})$$

Moreover, equation (71), which is valid for case 1 in the limit $\theta_r \ll 1$ that applies in our intermediate regime, implies that $(1 - \tilde{R}_e)\theta_r^2$ is approximately constant in this range of θ_r values given by equation (B1). Therefore, from equation (B5) we conclude that the integrand in the integration over $d\tilde{R}_e$ is approximately constant over this range in \tilde{R}_e , which is of interest here. Furthermore, the integrand must still have a similar value, up to a factor of order unity, even for $\theta_r \sim 1$, since the approximation of $\theta_r \ll 1$ breaks only marginally, rather than very severely (since θ_r cannot have values $\gg 1$). As the region where our approximation breaks, $\theta_r \sim 1$, corresponds to $1 - \tilde{R}_e = O(\Gamma_t^{-2})$, i.e., a range of the order of Γ_t^{-2} in \tilde{R}_e , which is much smaller than the range over which our approximation is valid, and is also much smaller than the range in equation (B1), we conclude that the contribution to the integral from $\theta_r \sim 1$ can safely be neglected.

APPENDIX C

PROPERTIES OF THE PHOTON FIELD IN CASE 3

By changing the integration variable from μ_r to \tilde{R}_e we eliminated the need to express \tilde{R}_e as a function of μ_r and to calculate the minimal value μ_r , which corresponds to $\theta_{r,\max}$. Nevertheless, this is still interesting in terms of the properties of the local photon field, so it is given in this appendix. Each value of μ_r may correspond to two different values of \tilde{R}_e , one at the front and one at the back of the equal arrival time surface of photons to the point (R_t, t_t) . Equation (89) can be rewritten as

$$\tilde{R}_e^{m+2} - \left[\tilde{R}_{e,\max}^{m+1} + 2(m+1)\Gamma_t^2(1 - \mu_r) \right] \tilde{R}_e + 2(m+1)\Gamma_t^2(1 - \mu_r) = \tilde{R}_e^{m+2} - 2(m+1)\Gamma_t^2 \left(\frac{ct_t}{R_t} - \mu_r \right) \tilde{R}_e + 2(m+1)\Gamma_t^2(1 - \mu_r) = 0. \quad (C1)$$

For $m = 0$ this becomes a second-order equation with the solutions

$$\tilde{R}_e = \Gamma_t^2 \left(\frac{ct_t}{R_t} - \mu_r \right) \left[1 \pm \sqrt{1 - \frac{2\Gamma_t^2(1 - \mu_r)}{\Gamma_t^4(ct_t/R_t - \mu_r)^2}} \right] = \frac{\tilde{R}_{e,\max} + (\Gamma_t\theta_r)^2}{2} \left\{ 1 \pm \sqrt{1 - \frac{4(\Gamma_t\theta_r)^2}{[\tilde{R}_{e,\max} + (\Gamma_t\theta_r)^2]^2}} \right\}, \quad (C2)$$

where $\theta_{r,\max}$ may be obtained by the condition of a single solution, i.e., that the expression in the square root vanishes. This implies

$$(\Gamma_t\theta_{r,\max})^2 = (2 - \tilde{R}_{e,\max}) \left[1 - \sqrt{1 - \left(\frac{\tilde{R}_{e,\max}}{2 - \tilde{R}_{e,\max}} \right)^2} \right], \quad (C3)$$

where we chose the root of the equation which corresponds to the familiar result of $\Gamma_t\theta_{r,\max} \approx \tilde{R}_{e,\max}/2$ for $\tilde{R}_{e,\max} \ll 1$.

More generally, $\mu_{r,\min} = \cos\theta_{r,\max}$ may be found by the condition that $d\mu_r/d\tilde{R}_e = 0$. Using equation (91), this results in

$$(m+1)\tilde{R}_e^{m+2} - (m+2)\tilde{R}_e^{m+1} + \tilde{R}_{e,\max}^{m+1} = 0, \quad (\Gamma_t\theta_{r,\max})^2 = [\tilde{R}_e(\theta_{r,\max})]^{m+2}. \quad (C4)$$

Alternatively, one can use the latter relation, which is obtained by substituting $d\mu_r/d\tilde{R}_e = 0$ from equation (91) into equation (89), to obtain an explicit equation for $\theta_{r,\max}$,

$$(m+1)(\Gamma_t\theta_{r,\max})^2 - (m+2)(\Gamma_t\theta_{r,\max})^{2(m+1)/(m+2)} + \tilde{R}_{e,\max}^{m+1} = 0. \quad (C5)$$

APPENDIX D

THE SCALING OF $\tau_{\gamma\gamma}$ WITH \bar{T}

It is instructive to explicitly derive the scaling of $\tau_{\gamma\gamma} = \tau_0(\varepsilon_t, \hat{R}_t)\mathcal{F}(x)$ with \bar{T} , in the two regimes $1 \gg \bar{T} < \bar{T}_f$ and $1 \ll \bar{T} < \bar{T}_f$. The only time dependence of τ_0 on \bar{T} is through $\hat{R}_0 = y^{-1}(T/T_0)^{-1/(m+1)}$ (see eq. [40]), so that $\tau_0 \propto (1 + \bar{T})^{(b-1+\alpha m/2)/(m+1)}$.

$$D1. 1 \gg \bar{T} < \bar{T}_f$$

For $1 \gg \bar{T} < \bar{T}_f$, τ_0 is thus approximately constant and the time dependence of $\tau_{\gamma\gamma}$ is dominated by the time dependence of $\mathcal{F}(x)$, which we now consider in more detail. First, the maximal value of the emission angle $\theta_{t,0}$ and correspondingly of $x = (\gamma_{t,0}\theta_{t,0})^2$ along the EATS-I is given by

$$T - T_0 = \frac{R_0\theta_{t,0}^2}{2c} = T_0(m+1)x_{\max} \iff x_{\max}(\bar{T}) = \frac{\bar{T}}{(m+1)}. \quad (D1)$$

This result holds in general and can be readily obtained by noticing that x_{\max} always corresponds to $y_{\min} = (T/T_0)^{-1/(m+1)}$ and substituting the latter in equation (16). Therefore, $x \leq x_{\max} \ll 1$ for $\bar{T} \ll 1$ and we are always in case 3. Second, it is straightforward to show that

$$f_m(\hat{R}_t) \left(\frac{\hat{R}_0 + \Delta \hat{R}}{\hat{R}_t} \right)^{-(m+1)} = \left(\frac{1 + \bar{T}}{1 + \bar{T}_f} \right) \frac{1 + x(m+1)(1 - \hat{R}_t^{-1})}{1 + x(m+1)} < \frac{1 + \bar{T}}{1 + \bar{T}_f}, \tag{D2}$$

so that for $\bar{T} \leq \bar{T}_f$ we always have

$$\tilde{R}_{e,\max} = \tilde{R}_{e,3} = f_m(\hat{R}_t)^{1/(m+1)} = \hat{R}_t^{-1} [1 + x(m+1)(1 - \hat{R}_t^{-1})]^{1/(m+1)}, \tag{D3}$$

$$\mathcal{F}(x) = \int_1^\infty d\hat{R}_t \int_{\hat{R}_0/\hat{R}_t}^{\tilde{R}_{e,3}} d\tilde{R}_e \mathcal{I}(\hat{R}_t, \tilde{R}_e, x), \tag{D4}$$

where $\mathcal{I}(\hat{R}_t, \tilde{R}_e, x)$ is given in equation (100), and

$$\tilde{R}_{e,\min} = \frac{\hat{R}_0}{\hat{R}_t} = \hat{R}_t^{-1} \left[\frac{1 + (m+1)x}{1 + \bar{T}} \right]^{1/(m+1)}. \tag{D5}$$

Keeping terms to first order in \bar{T} (and x), the range of \tilde{R}_e value that is being integrated over in equation (D4) is

$$\Delta \tilde{R}_e = \tilde{R}_{e,\max} - \tilde{R}_{e,\min} \approx \frac{\bar{T}}{(m+1)\hat{R}_t} - \frac{x}{\hat{R}_t^2} = O(\bar{T}) \ll 1. \tag{D6}$$

The integrand includes in several places the expression

$$f_m(\hat{R}_t) - \tilde{R}_e^{m+1} = \tilde{R}_{e,\max}^{m+1} - \tilde{R}_e^{m+1} \approx (m+1)\tilde{R}_{e,\max}^m (\tilde{R}_{e,\max} - \tilde{R}_e) \ll 1, \tag{D7}$$

which is either comparable to or much smaller than $1 - \tilde{R}_e$, which also appears in the integrand, thus defining different regimes. The relevant ratio to compare to unity is

$$\max \left(\frac{\tilde{R}_{e,\max} - \tilde{R}_e}{1 - \tilde{R}_e} \right) = \frac{\Delta \tilde{R}_e}{1 - \tilde{R}_{e,\min}} = \frac{1 - \tilde{R}_{e,\min}}{1 - \tilde{R}_{e,\max}} - 1 \approx (\hat{R}_t - 1)^{-1} \left(\frac{\bar{T}}{m+1} - \frac{x}{\hat{R}_t} \right), \tag{D8}$$

which measures both the fractional change in $1 - \tilde{R}_e$ and the minimal value of its ratio to $\tilde{R}_{e,\max} - \tilde{R}_e$.

For $x = x_{\max} = \bar{T}/(m+1)$, this ratio is $x_{\max}/\hat{R}_t \leq \bar{T}/(m+1) \ll 1$ so that $1 - \tilde{R}_e$ is both approximately constant and much larger than $\tilde{R}_{e,\max} - \tilde{R}_e \sim f_m(\hat{R}_t) - \tilde{R}_e^{m+1}$. Therefore, the only term that varies significantly with \tilde{R}_e in the inner integrand is $\bar{\zeta}^\alpha H_\alpha(\bar{\zeta})$. For $\zeta \gg 1$, $H_\alpha(\zeta) \sim \zeta^\alpha$ so that $\bar{\zeta}^\alpha H_\alpha(\bar{\zeta}) \sim (\bar{\zeta} - \zeta)^\alpha \propto \bar{T}^{\alpha/2} (\tilde{R}_{e,\max} - \tilde{R}_e)^{\alpha/2}$ where the integration over $(\tilde{R}_{e,\max} - \tilde{R}_e)^{\alpha/2}$ results in a factor of $\bar{T}^{1+\alpha/2}$ so that altogether the inner integral is $\propto \bar{T}^{\alpha+1}$. The outer integral is of the form $\int_1^\infty d\hat{R}_t g(\hat{R}_t) = \text{const}$. For $\zeta \lesssim 1$, $H_\alpha(\zeta) \sim \frac{1}{\zeta}$ and $\bar{\zeta}^\alpha H_\alpha(\bar{\zeta}) \sim \bar{\zeta}^{\alpha-1} \sim (\Gamma_t \theta_r - \Gamma_t \theta_t)^{2\alpha}$ which consists of a sum of terms of the form $\bar{T}^a (\tilde{R}_{e,\max} - \tilde{R}_e)^{\alpha-a}$ that on integration are $\propto \bar{T}^{\alpha+1}$. Thus,

$$\mathcal{F}(x_{\max}) \propto \bar{T}^{\alpha+1}. \tag{D9}$$

Note that in this case most of the contribution to the optical depth comes from $\hat{R}_t \lesssim 2$ or $\Delta \hat{R}_t \sim 1$.

For $x = 0$, $\theta_t = \zeta = 0$ so that $H_\alpha(\zeta) = 1$. Furthermore, the ratio in equation (D8) becomes larger than unity for $\hat{R}_t - 1 < \bar{T}/(m+1)$, and in this regime, $f_m(\hat{R}_t) - \tilde{R}_e^{m+1} \sim \tilde{R}_{e,\max} - \tilde{R}_e \sim 1 - \tilde{R}_e$ so that $\bar{\zeta}$ is roughly constant and the inner integrand scales as $(1 - \tilde{R}_e)^{-1}$, which on integration scales linearly with \bar{T} ,

$$\begin{aligned} \int_1^{1+x_{\max}} d\hat{R}_t g(\hat{R}_t) \int_{(1-x_{\max})/\hat{R}_t}^{1/\hat{R}_t} \frac{d\tilde{R}_e}{(1-\tilde{R}_e)} &\approx g(1) \int_0^{x_{\max}} d(\hat{R}_t - 1) \ln \left[\frac{(\hat{R}_t - 1) + x_{\max}}{(\hat{R}_t - 1)} \right] \\ &= g(1)(2 \ln 2)x_{\max} \propto \bar{T}. \end{aligned} \tag{D10}$$

For $\hat{R}_t - 1 \gg x_{\max} = \bar{T}/(m+1)$, the approximation discussed in the previous paragraph applies, and this part of the integration over \hat{R}_t does not contribute significantly to the total optical depth, so that

$$\mathcal{F}(x=0) \propto \bar{T}. \tag{D11}$$

Physically, the lack of significant contribution to the optical depth from $\hat{R}_t - 1 \gg x_{\max} = \bar{T}/(m+1)$ may be understood, since the maximal value of θ_r (which corresponds to $R_e = R_0$) starts to decrease significantly,

$$\begin{aligned} \max[(\Gamma_0 \theta_r)^2] &\approx \frac{\bar{T}}{(m+1)} \hat{R}_t^{-2} \left[\hat{R}_t - 1 + \frac{\bar{T}}{(m+1)} \right]^{-1} \\ &\approx \begin{cases} 1, & \hat{R}_t - 1 \ll \frac{\bar{T}}{(m+1)}, \\ \frac{\bar{T}}{(m+1)(\hat{R}_t - 1)\hat{R}_t^2} \ll 1, & \hat{R}_t - 1 \gg \frac{\bar{T}}{(m+1)}, \end{cases} \end{aligned} \quad (\text{D12})$$

which suppresses the opacity to pair production.

$$\text{D2. } 1 \ll \bar{T} < \bar{T}_f$$

For $1 \ll \bar{T} < \bar{T}_f$, we have $R_{t,0} \gg R_0$, so that $\hat{R}_0/\hat{R}_t \ll 1$ and may effectively be taken as zero. Furthermore, $R_{e,\max} < R_L(\bar{T}) < R_L(\bar{T}_f) = R_0 + \Delta R$ (since $\bar{T} < \bar{T}_f$) so that $\hat{R}_{e,2} = 1$ and $\hat{R}_{e,3} = f_m(x, \hat{R}_t)^{1/(m+1)}$ is given by equation (D3), and equation (98) now reads

$$\mathcal{F}(x) = \int_1^{\hat{R}_2(x)} d\hat{R}_t \int_0^1 d\hat{R}_e \mathcal{I}(\hat{R}_t, \hat{R}_e) + \int_{\hat{R}_2(x)}^\infty d\hat{R}_t \int_0^{f_m(x, \hat{R}_t)^{1/(m+1)}} d\hat{R}_e \mathcal{I}(\hat{R}_t, \hat{R}_e). \quad (\text{D13})$$

In this regime neither the boundaries of integration nor the integrand, \mathcal{I} , depend on \bar{T} . As a consequence, the dependence of $\tau_{\gamma\gamma}$ in this regime is only through τ_0 , and we have

$$\tau_{\gamma\gamma}(1 \ll \bar{T} < \bar{T}_f) \approx \tau_0(\bar{T}) \mathcal{F}(x) \propto \bar{T}^{(b-1+\alpha m/2)/(m+1)}. \quad (\text{D14})$$

APPENDIX E

ON THE DEFINITION OF THE OPTICAL DEPTH

We start with the explicitly Lorentz-invariant expression for the differential interaction rate of two particles, denoted 1 and 2, colliding with respective momenta \mathbf{p}_1 and \mathbf{p}_2 , as given in equation (24a) of Weaver (1976),

$$R_{12}(\mathbf{p}_1, \mathbf{p}_2) \equiv \frac{n_1(\mathbf{p}_1)n_2(\mathbf{p}_2)(1 - \beta_1 \cdot \beta_2)[(p_1 \cdot p_2)^2 - m_1^2 m_2^2 c^4]^{1/2}}{p_1 \cdot p_2} c\sigma, \quad (\text{E1})$$

where p_1 and p_2 are the four-momenta of particles 1 and 2, respectively, m_1 and m_2 are their masses, $n_1(\mathbf{p}_1)$ and $n_2(\mathbf{p}_2)$ their phase-space density, and σ is the generalized Lorentz-invariant cross section, usually computed in the center of momentum frame. In equation (E1), we have explicitly written the dependence of R_{12} on the momenta, which is missing in Weaver (1976) in order to distinguish it from the total interaction rate $\langle R_{12} \rangle$. The latter results from an integration over the phase spaces of both particles (see eqs. [2] and [27] in Weaver 1976),

$$\langle R_{12} \rangle = \frac{1}{1 + \delta_{12}} \int \int R_{12}(\mathbf{p}_1, \mathbf{p}_2) d^3\mathbf{p}_1 d^3\mathbf{p}_2. \quad (\text{E2})$$

In equation (E2), the Kronecker symbol δ_{12} is 1 if the two particles are identical and 0 otherwise. It accounts for the fact that, for identical particles, the double integration counts twice each pair of interacting particles.

Now, we define $R_{12}(\mathbf{p}_1)$ as the interaction rate of a *given* particle 1 of momentum p_1 . It writes $R_{12}(\mathbf{p}_1) = \int R_{12}(\mathbf{p}_1, \mathbf{p}_2) d^3\mathbf{p}_2$, without a Kronecker symbol because there cannot be any double counting when there is no double integration. Specializing now to $\gamma\gamma$ -interactions, the interaction rate $R_{\gamma\gamma}(\mathbf{p}_1)$ is equal to the decrease in n_1 per unit time, $dn_1(\mathbf{p}_1)/dt = -R_{\gamma\gamma}(\mathbf{p}_1)$. Defining the differential optical depth of a particle of type 1 and momentum \mathbf{p}_1 as the corresponding attenuation per unit length, $d\tau_{\gamma\gamma}(\mathbf{p}_1) \equiv -dn_1/n_1 = R_{\gamma\gamma}(\mathbf{p}_1) ds/cn_1$, where ds is an element of the trajectory of particle 1, we obtain

$$\tau_{\gamma\gamma}(\mathbf{p}_1) \equiv \int ds R_{\gamma\gamma}(\mathbf{p}_1)/(cn_1) = \int ds \int n_2(\mathbf{p}_2)(1 - \beta_1 \cdot \beta_2)\sigma d^3\mathbf{p}_2, \quad (\text{E3})$$

where in the last equality we made use of $m_1 = m_2 = 0$ in equation (E1). We thus rederived equation (17) (in integral form) and showed that there is no factor 1/2 involved because the computation of the optical depth does not warrant a double integration over the phase space of both particles. Because they compute the total reaction rates and not the optical depth, Weaver (1976) and Stepney & Guilbert (1983) do have this factor.

Another source of confusion arises from the fact that in their seminal paper, Gould & Schreder (1967) specialized to an isotropic distribution for particles 2, which brings up a factor 1/2 due only to the normalization of the integration over $\cos \theta$. In other words, introducing $dn \equiv n_2(\mathbf{p}_2) d^3\mathbf{p}_2 = (1/2)n(\varepsilon)d\varepsilon \sin \theta d\theta$ in equation (E3) immediately yields their equation (7).

REFERENCES

- Abramowitz, M., & Stegun, I. A. 1964, *Handbook of Mathematical Functions with Formulas, Graphs, and Mathematical Tables* (New York: Dover)
- Baring, M. G. 1994, *ApJS*, 90, 899
- . 2006, *ApJ*, 650, 1004
- Baring, M. G., & Harding, A. K. 1997, *ApJ*, 491, 663
- Begelman, M. C., Fabian, A. C., & Rees, M. J. 2007, *MNRAS*, in press (arXiv: 0709.0540)
- Blandford, R. D., & Levinson, A. 1995, *ApJ*, 441, 79
- Blandford, R. D., & McKee, C. F. 1976, *Phys. Fluids*, 19, 1130
- Dermer, C. D., & Schlickeiser, R. 1994, *ApJS*, 90, 945
- Fenimore, E. E., Epstein, R. I., & Ho, C. 1993, *A&AS*, 97, 59
- Gould, R. J., & Schreder, G. 1967, *Phys. Rev.*, 155, 1404
- Granot, J. 2005, *ApJ*, 631, 1022
- Granot, J., & Loeb, A. 2001, *ApJ*, 551, L63
- Granot, J., Piran, T., & Sari, R. 1999a, *ApJ*, 513, 679
- . 1999b, *ApJ*, 527, 236
- Guetta, D., & Granot, J. 2003, *MNRAS*, 340, 115
- Kneiske, T. M., Bretz, T., Mannheim, K., & Hartmann, D. H. 2004, *A&A*, 413, 807
- Königl, A., & Granot, J. 2002, *ApJ*, 574, 134
- Krolik, J. H., & Pier, E. A. 1991, *ApJ*, 373, 277
- Kumar, P., & Panaitescu, A. 2000, *ApJ*, 541, L51
- Lee, W. H., Ramirez-Ruiz, E., & Granot, J. 2005, *ApJ*, 630, L165
- Lithwick, Y., & Sari, R. 2001, *ApJ*, 555, 540
- Lyutikov, M., & Blandford, R. D. 2002, in *Beaming and Jets in Gamma Ray Bursts*, ed. R. Ouyed (Stanford: SLAC), 146
- . 2003, preprint (astro-ph/0312347)
- Mészáros, P. 2006, *Rep. Prog. Phys.*, 69, 2259
- Molinari, E., et. al. 2007, *A&A*, 469, L13
- Panaitescu, A., & Kumar, P. 2002, *ApJ*, 571, 779
- Piran, T. 2005, *Rev. Mod. Phys.*, 76, 1143
- Rees, M. 1966, *Nature*, 211, 468
- Rees, M. J., & Mészáros, P. 1994, *ApJ*, 430, L93
- Reimer, O. 2007, in *Exploring the Cosmic Frontier*, ed. A. P. Lobanov et al. (Berlin: Springer), 77
- Ritz, S. 2007, in *AIP Conf. Proc. 921, First Int. GLAST Symp.*, ed. S. Ritz et al. (Melville: AIP), 3
- Ruderman, M. 1975, *Ann. NY Acad. Sci.*, 262, 164
- Sari, R. 1998, *ApJ*, 494, L49
- Sikora, M., Begelman, M. C., & Rees, M. J. 1994, *ApJ*, 421, 153
- Stepney, S., & Guilbert, P. W. 1983, *MNRAS*, 204, 1269
- Waxman, E. 1997, *ApJ*, 491, L19
- Weaver, T. A. 1976, *Phys. Rev. A*, 13, 1563
- Woods, E., & Loeb, A. 1995, *ApJ*, 453, 583